ALL-OPTICAL MODULATION OF LINEAR AND NONLINEAR EMISSIONS IN PLASMONIC NANOGAP SYSTEMS

LIU DANJUN

PhD

The Hong Kong Polytechnic University

2021

The Hong Kong Polytechnic University

Department of Applied Physics

All-Optical Modulation of Linear and Nonlinear Emissions in Plasmonic Nanogap Systems

Liu Danjun

A Thesis Submitted in Partial Fulfilment
of the Requirements for the Degree of
Doctor of Philosophy

January 2021

CERTIFICATE OF ORIGINALITY

I hereby declare that this thesis is my own work and that, to the best of my knowledge and belief, it reproduces no material previously published or written, nor material that has been accepted for the award of any other degree or diploma, except where due acknowledgement has been made in the text.

_____ (Signed)

Liu Danjun (Name of student)

Abstract

The past decades have witnessed the rapid growth of studies regarding light-matter interactions in plasmonic systems. It is well-known that light can be confined at subwavelength scale in plasmonic nanostructures, which could generate electromagnetic (EM) field enhancement and boost many optical phenomena such as Raman, fluorescence, harmonic generation and two-photon luminescence (TPL). In this respect, considerable attention has been paid to further improve the light concentration in plasmonic systems. Meanwhile, most plasmonic nanostructures are passive systems, which largely limit the scope and flexibility of their applications. Therefore, it is of great importance to realize all-optical modulation in active plasmonic systems. Based on above-mentioned points, plasmonic nanogap systems (PNSs) have been recently selected as one of the best candidates for both passive and active control of optical emissions. In the PNS, EM field is highly localized in the gap region, thus leading to ultrasmall mode volume compared with conventional dielectric microcavities. In addition, all-optical modulation of the optical responses in PNS can also be achieved by filling the gap with active materials.

This thesis covers my research on investigating all-optical modulation of both linear and nonlinear responses in two specific PNSs, i.e. plasmonic metal particle-on-film nanocavities (MPoFNs) and gold sphere plasmonic nanomatryoshkas (GSPNs). On the one hand, I collected and analyzed the light scattering and Raman enhancement in graphene- and molecule-sandwiched MPoFNs to probe two common quantum size effects, namely spatial nonlocality and quantum charge transport, respectively. I also achieved reversible plasmon resonance tuning in photoswitchable molecule-sandwiched MPoFNs, which demonstrates my study on all-optical modulation of linear optical emissions in the PNS. On the other hand, I continued to explore the influence of electron transport on TPL response of GSPNs

embedded with molecular nanojunctions, which lays the foundation for active control of nonlinear optical phenomena in PNSs. The main contents and conclusions for each work are listed as follows:

First and foremost, surface-enhanced Raman spectroscopy (SERS) was taken as a tool to probe the horizontal near-field enhancement limit in graphene-coupled MPoFNs, where one to four layers of graphene were sandwiched between a gold nanosphere (Au NS) and the underlying gold thin film (Au TF). In combination with the high-resolution transmission electron microscopy (TEM) cross-sectional imaging and calculations based on nonlocal hydrodynamic model (NLHD), the gap distance correlated SERS and dark-field scattering spectroscopies were performed on graphene-sandwiched MPoFNs, which unravel that the intrinsic nonlocal effect of gold sets a limit to the near-field enhancement factors (EFs) and mitigates the red-shift of plasmon resonance when the gap distance was reduced to sub-nanometer level. The results not only prove former theoretical predictions under both near- and far-field regime but also show the feasibility of tuning the optical response in the versatile graphene-sandwiched MPoFNs, which has a great potential in designing the graphene-based optical devices ranging from visible to near-infrared frequencies.

Next, I carried out far- and near-field optical characterizations on MPoFNs embedded with two types of organic molecules. Specifically, a clear blue-shift of major plasmon resonance modes was observed in conductive molecule (BPDT)-sandwiched MPoFNs in comparison to that in insulating counterparts (B4T). The physical origins of the hybridized plasmon modes were also disclosed via polarization-dependent dark-field spectroscopy, and the reduced SERS intensity of the vibrational modes verifies the quenching of near-field plasmonic enhancement which originates from electron transport in the molecular tunnel junctions. After discussing quantum size effects in the passive plasmonic system, I further investigated the active modulation of plasmon resonance in MPoFNs embedded with photoactive molecules under ultraviolet (UV)-visible light irradiation, and reversible tuning of major plasmon

resonance was preliminarily realized in individual MPoFN under ambient conditions. Based on the findings in this part, molecule-sandwiched MPoFNs can be employed as a versatile platform to achieve active control of optical signals under quantum regime, thus opening up a new avenue in the study of molecular electronics.

In the final part of this thesis, TPL spectroscopy was utilized to explore the influence of electron transport on the plasmonic characteristics of GSPNs with varied junction width. Together with the measured linear and TPL responses of different GSPNs, theoretical and numerical analyses unraveled that the TPL emission of the nanojunctions is closely related to the near-field enhancement within the metal regions, and is largely influenced by the electron transport across the molecular nanojunctions. Besides, the excitation-wavelength dependent TPL intensities of three typical nanojunctions (0.7 nm, 0.9 nm and 1.5 nm junction widths) and an Au NS of the similar size were measured under femtosecond laser illumination, and no perceivable contribution from the low-energy plasmon modes (LEM) of those nanojunctions was discovered. This experimental observation is consistent with the numerical results based on quantum-corrected model (QCM), assuming the value of conductance for molecular layers and the efficient electron transport across the nanojunctions. These results provide possibilities for investigating charge transport in molecular nanojunctions by plasmon-mediated nonlinear spectroscopies and can be further applied in active PNSs.

List of Publications and Conference Presentations

Journal publications based on this thesis work:

([#] equally contributed, * corresponding author)

1. **Liu, D.**[#]; Wu, T.[#]; Zhang, Q.[#]; Wang, X.[#]; Guo, X.; Su, Y.; Zhu, Y.; Shao, M.; Chen, H.; Luo, Y.; Lei, D.[*] "Probing the in-Plane Near-Field Enhancement Limit in a Plasmonic Particle-on-Film Nanocavity with Surface-Enhanced Raman Spectroscopy of Graphene." ***ACS Nano*** 2019, 13, 7644–7654.
2. Zhang, Q.[#]; **Liu, D.**[#]; Ren, Q.; Panoiu, N.-C.; Lin, L.; Ye, J.; Huang, Y.; Liu, S.-D.; Leung, C. W.; Lei, D.[*] "Probing Electron Transport in Plasmonic Molecular Junctions with Two-Photon Luminescence Spectroscopy." ***Nanophotonics*** 2021, 10, 2467-2479.

Journal publications during my PhD study but not included in this thesis:

([#] equally contributed, * corresponding author)

3. Hu, H.[#]; Ren, Z.[#]; Fong, P. W. K.; Qin, M.; **Liu, D.**; Lei, D.; Lu, X.; Li, G.[*] "Room-Temperature Meniscus Coating of >20% Perovskite Solar Cells: A Film Formation Mechanism Investigation." ***Adv. Funct. Mater.*** 2019, 29, 1900092.
4. Wu, S.[#]; Zhang, J.[#]; Li, Z.[#]; **Liu, D.**; Qin, M.; Cheung, S. H.; Lu, X.; Lei, D.; So, S. K.; Zhu, Z.[*]; Jen, A. K.-Y.[*] "Modulation of Defects and Interfaces through Alkylammonium Interlayer for Efficient Inverted Perovskite Solar Cells." ***Joule*** 2020, 4, 1248-1262.
5. Li, Z.[#]; Zhang, J.[#]; Wu, S.; Deng, X.; Li, F.; **Liu, D.**; Lee, C.-C.; Lin, F.; Lei, D.; Chueh, C.-C.; Zhu, Z.[*]; Jen, A. K.-Y.[*] "Minimized Surface Deficiency on Wide-Bandgap Perovskite for Efficient Indoor Photovoltaics." ***Nano Energy*** 2020, 78, 105377.

6. Li, F.[#]; Deng, X.[#]; Qi, F.; Li, Z.; **Liu, D.**; Shen, D.; Qin, M.; Wu, S.; Lin, F.; Jang, S.-H.; Zhang, J.; Lu, X.; Lei, D.; Lee, C.-S.; Zhu, Z.[*]; Jen, A. K.-Y.[*] "Regulating Surface Termination for Efficient Inverted Perovskite Solar Cells with Greater Than 23% Efficiency." ***J. Am. Chem. Soc.*** 2020, 142, 20134-20142.
7. Sun, X.[#]; Li, Z.[#]; Yu, X.; Wu, X.; Zhong, C.; **Liu, D.**; Lei, D.; Jen, A. K.-Y.; Li, Z.[*]; Zhu, Z.[*] "Efficient Inverted Perovskite Solar Cells with Low Voltage Loss Achieved by a Pyridine-based Dopant-free Polymer Semiconductor." ***Angewandte Chemie.*** 2020, 133, 7303-7309.
8. Cai, N.[#, *]; Li, F.[#]; Chen, Y.; Luo, R.; Hu, T.; Lin, F.; Yiu, S.-M.; **Liu, D.**; Lei, D.; Zhu, Z.; Jen, A. K.-Y.[*] "Synergistical Dipole-Dipole Interactions Induced Self-Assembly of Phenoxazine-Based Hole-Transporting Materials for Efficient and Stable Inverted Perovskite Solar Cells." ***Angewandte Chemie.*** 2021.

Acknowledgments

Creating a PhD thesis is not an individual experience. During my three-years PhD study, many people have given me the strength to finish this study. Therefore, I would like to give thanks to all the persons that have become a big part of this journey.

Foremost, I would like to express my deep gratitude to my first supervisor Dr. Dangyuan Lei for the continuous support of my PhD study, and pushing me farther than I thought I could go. Under his guidance I have learned how to complete a research project and collaborate with researcher in different fields. Without his guidance and persistent help this thesis would not have been possible. I would also like to thank my second supervisor Dr. Chi Wah Dennis Leung for supporting the research and providing me some useful suggestions during the last one and half year of my PhD study.

My appreciation also extends to both former and current laboratory colleagues. Dr. Qiang Zhang and Dr. Guang-Can Li are experts on nano-plasmonics and nano-photonics research field. I have learnt a lot from their energy and enthusiasm for research. They always provide insightful comments and help me to overcome obstacles. Thanks also go to other groupmates: Dr. Zhiyong Bao, Dr. Meng Qiu, Dr. Siqi Li, Dr. Tsz Wing Lo, and Miss Han Gao for both theoretical and experimental assistance and suggestions throughout my project. Besides, I take this opportunity to record my sincere thanks to all the faculty members in the university who, directly or indirectly, have lent their helping hand in this venture.

Last but not least, I would like to give special thanks to my friends and family for helping me survive all the stress from these years and not letting me give up, especially my mother who always show

understanding and encourage me spiritually even when I faced many ups and downs throughout my life. Without their unconditional love and support, I won't go this far in my career.

Table of Contents

Abstract I
List of Publications and Conference Presentations IV
Acknowledgments VI
Table of Contents VIII
Nomenclature X
Chapter 1 Introduction and Literature Review 2
1.1 Light-Matter Interactions at the Nanoscale 2
1.2 Surface Plasmon Polaritons and Localized Surface Plasmons 3
1.3 Plasmon Coupling in Plasmonic Nanostructures 6
1.4 Quantum Size Effects in Plasmonic Nanogap Systems (PNSs) 10
1.4.1 Classical Local Response 11
1.4.2 Nonlocal Response 11
1.4.3 Vacuum Tunneling and Molecular Charge Transport 14
1.5 Two-Photon Photoluminescence in Metallic Nanostructures 17
Chapter 2 Plasmonic Nanostructure Fabrication and Characterization 20
2.1 Preparation of Graphene-Sandwiched Plasmonic Metal Particle-on-Film Nanocavities (MPoFNs) 20
2.2 Synthesis of Gold Sphere Plasmonic Nanomatryoshkas (GSPNs) 23
2.3 Synthesis of Molecule-Decorated Au NPs 24
2.4 Synthesis of Photoswitchable Molecule-Sandwiched MPoFNs 25
2.5 Ultraviolet-Visible (UV-Vis) Spectroscopy 26
2.6 Single-Particle Dark-Field Spectroscopy 27
2.7 Raman Spectroscopy 29
2.8 Confocal Nonlinear Optical Spectroscopy 30
Chapter 3 Passive Control of Light Scattering and Raman Enhancement in Graphene-Sandwiched Plasmonic Metal Particle-on-Film Nanocavities (MPoFNs): Spatial Nonlocality Effect 31
3.1 Gap Widths Characterization on Graphene-Sandwiched MPoFNs 34
3.2 Far- and Near-Field Spectroscopies of Graphene-Sandwiched MPoFNs 36
3.3 Observation of Horizontal Near-Field Enhancement Limit in Graphene-Sandwiched MPoFNs 47
3.4 Conclusion 49

Chapter 4 Passive and Active Modulation of Light Scattering and Raman Enhancement in Molecule-Sandwiched Plasmonic Metal Particle-on-Film Nanocavities (MPoFNs): Molecular Charge Transport 51
4.1 Molecular Conductance Induced Plasmon Resonance Shift and Its Influence on Near-Field Enhancement 52
4.2 Spectral Decomposition of Plasmonic Modes in Molecule-Sandwiched MPoFNs 56
4.3 Reversible Plasmon Resonance Tuning in Photoswitchable Molecule-Sandwiched MPoFNs 58
4.4 Conclusion 60
Chapter 5 Unveiling Electron Transport in Gold Sphere Plasmonic Nanomatryoshkas (GSPNs) with Two-Photon Luminescence (TPL) Spectroscopy 62
5.1 Linear Optical Response of GSPNs 63
5.2 Two-Photon Luminescence Response of GSPNs with Different Molecular Junctions 69
5.3 Influence of Electron Transport on Two-Photon Luminescence Response of GSPNs 74
5.4 Conclusion 79
Chapter 6 Conclusion and Outlook 81
Appendices 84
References 88

Nomenclature

EM	Electromagnetic
PNSs	Plasmonic Nanogap Systems
TM	Transverse Magnetic
SPPs	Surface Plasmon Polaritons
SPRs	Surface Plasmon Resonances
LSPs	Localized Surface Plasmons
LSPRs	Localized Surface Plasmon Resonances
TIR	Total Internal Reflection
Au NPs	Gold Nanoparticles
Au NS	Gold Nanosphere
Au TF	Gold Thin Film
MPoFNs	Plasmonic Metal Particle-on-Film Nanocavities
MIM	Metal-Insulator-Metal
2-D TMDs	Two-Dimensional Transition Metal Dichalcogenides
SLG	Single-Layer Graphene
RMS	Root-Mean-Square
SERS	Surface-Enhanced Raman Spectroscopy/Scattering
EFs	Enhancement Factors
SEF	Surface-Enhanced Fluorescence
CW	Continuous Wave
TPL	Two-Photon Luminescence
CTAB/ CTAC	Cetyltrimethylammonium Bromide/ Cetyltrimethylammonium chloride
SEM	Scanning Electron Microscopy
TEM	Transmission Electron Microscope
STEM	Scanning Transmission Electron Microscope
NA	Numerical Aperture
CEM	Classical Electromagnetic Model

QM	Quantum Model
QCM	Quantum-Corrected Model
TDDFT	Time-Dependent Density Functional Theory
AFM	Atomic Force Microscopy
EELS	Electron Energy Loss Spectroscopy
BDP	Bonding Dipolar Plasmon
SBDP	Screened Bonding Dipolar Plasmon
CTP	Charge Transfer Plasmon
tCTP	Tunneling Charge Transfer Plasmon
SAM	Self-Assembly Method/ Self-Assembled Monolayer
DC	Direct Current
EDT	1,2-ethanedithiol
BDT	1,4-benzenedithiol
BPDT	4,4'-biphenyldithiol
TPDT	4,4'-terpheyldithiol
MBT	4-methylbenzenethiol
B4T/BPT	biphenyl-4-thiol
LEM	Low-Energy Mode
HEM	High-Energy Mode
GSPN	Gold Sphere Plasmonic Nanomatryoshka
PML	Perfect Matched Layer
ED	Electric Dipole
EQ	Electric Quadrupole

Chapter 1 Introduction and Literature Review

1.1 Light-Matter Interactions at the Nanoscale

The interaction between light and matter that leads to several optical phenomena (such as fluorescence, Raman scattering and nonlinear optical emissions) has been extensively studied both theoretically and experimentally during the last decades[1]. Classically, light-matter interactions could be amplified through reducing the mode volume of the structure. To achieve this, nanomaterials or plasmonic nanostructures with small feature sizes could be used to control light-matter interactions beyond the diffraction limit in the range from visible to near-infrared frequencies[2-6]. However, when the dimension of nanostructures reaches to few atoms, exploring the coupling between incident photons and atoms could reveal quantum mechanical information of these nanostructures. Although studies relevant to these pioneering research areas remain a challenging task and usually requires extreme experimental conditions[7], there have been plenty of breakthroughs and prosperity is expected in research field of nano-optics or nano-photonics with the rapid growth of nano-fabrication and characterization.

Recently, plasmon-enhanced light-matter interactions such as surface-enhanced fluorescence (SEF), surface-enhanced Raman scattering (SERS) as well as other plasmon-enhanced linear and nonlinear optical signals have been widely investigated and applied in various fields, including photocatalysis, photovoltaics, molecular cavity optomechanics and biosensing[8-10] (Fig. 1.1). The mechanism behind these optical phenomena can be well interpreted within the context of plasmonics[11], which results from the resonant excitations of surface plasmons (SPs). Besides, phonon-enhanced light-matter interactions

are also investigated in polar dielectrics, which would open a new avenue in high-field nonlinear physics[12].

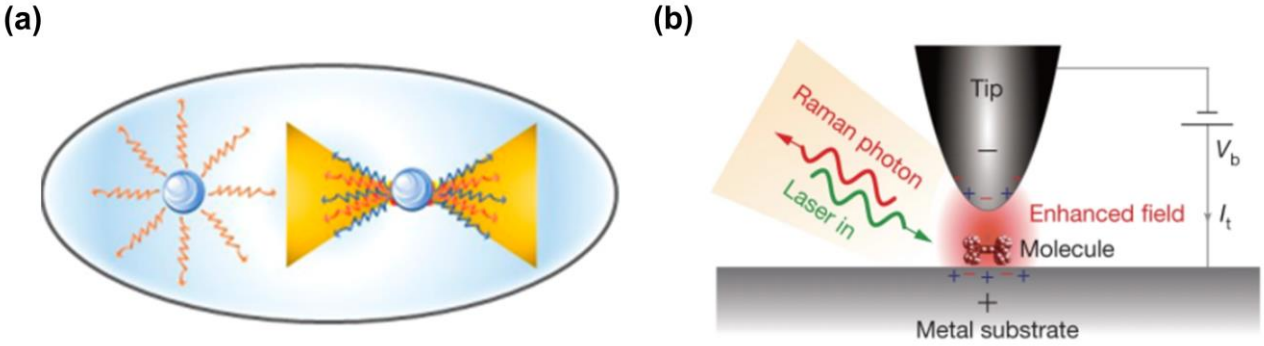

Figure 1.1 Schematics of light-matter interaction in (a) quantum emitter (QE)/gold-bowtie nanoantenna hybrid nanostructure[13] and (b) tunneling-controlled confocal-type TERS testing configuration[14].

1.2 Surface Plasmon Polaritons and Localized Surface Plasmons

SPs usually occurs at the interface between two materials exhibiting opposite signs (negative or positive) in the real part of dielectric functions. In most cases, metal-dielectric interface can satisfy the condition for exciting SPs by inducing collective oscillations of free electrons in metal. When the oscillation is on resonance, the so-called surface plasmon resonance (SPR) will largely boost light-matter interactions, which is applied to measure absorption of materials on both rough and planar metal surfaces. Generally, two kinds of SPs (surface plasmon polaritons (SPPs) and localized surface plasmons (LSPs), Fig. 1.2 (a, b)) resides in the plasmon-enhanced interactions between incident photons and nanostructures, which will be discussed in detail as below.

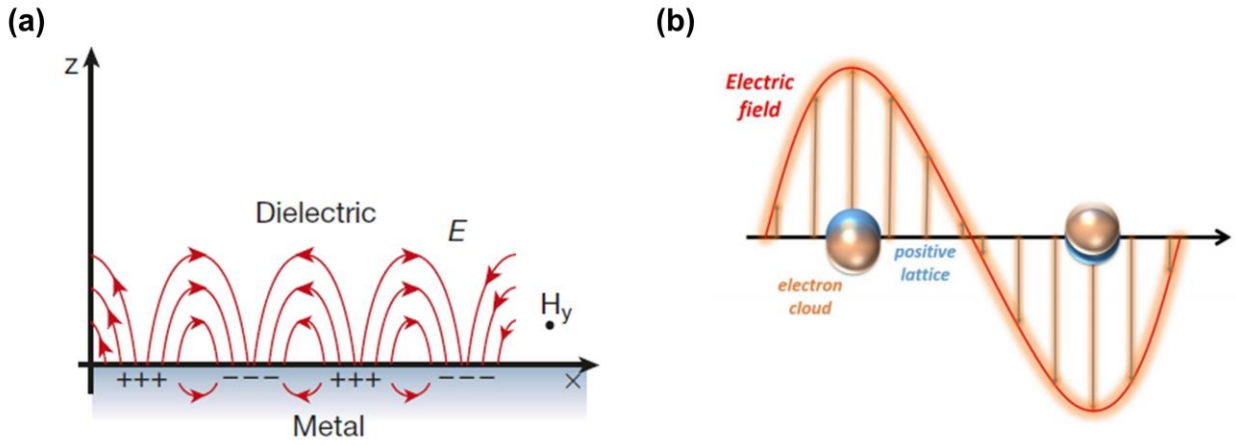

Figure 1.2 Illustration of (a) surface plasmon polariton (or propagating plasmon)[15] and (b) a localized surface plasmon[16]. The whole electron cloud in (b) is shifted relative to the positively charged lattice, and oscillates back and forth until it finally reaches the equilibrium.

Based on the theory of electromagnetics (EMs), SPPs can be regarded as a type of surface wave generated at the interface between metal and dielectric. The dispersion relation of this surface wave is obtained by solving Maxwell's equations under appropriate boundary conditions, which can be derived as follows:

$$k_{\mathrm{SPP}} = \frac{\omega}{\mathrm{c}}\left(\frac{\varepsilon_{\mathrm{m}}\varepsilon_{\mathrm{d}}}{\varepsilon_{\mathrm{m}}+\varepsilon_{\mathrm{d}}}\right)^{1/2} \tag{1.1}$$

where ω is the angular frequency of incident light, c is the speed of light wave, ε_{m} and ε_{d} are the permittivities of metal and dielectric respectively. The propagation length L_{SPP} can be written as $L_{\mathrm{SPP}} = 1/(2k''_{\mathrm{SPP}})$, where k''_{SPP} is the imaginary part of k_{SPP}, i.e., $k_{\mathrm{SPP}} = k'_{\mathrm{SPP}} + \mathrm{i}k''_{\mathrm{SPP}}$. Due to the absorption of metal, there is a strong lateral confinement at the interface. Besides, as the electric field decays instantly in the direction perpendicular to the surface of metal, there is a penetration depth of SPPs in both metal (L_{m}) and dielectric (L_{d}), both setting the limits in the vertical direction. In short, SPPs propagates along the metal-dielectric interface, but attenuates exponentially in the direction perpendicular to such interface. Therefore, tightly lateral (vertical) confinement at the interface and high

field localization are generally observed under the excitation of SPPs[13, 15, 17]. Although SPPs can be excited by both incident photons and electrons, the momentum-matching between free-space photon and SPPs needs to be satisfied. Generally, prisms or gratings are employed to match the difference in the wave vectors of both free-space photon and SPPs. For prism coupling method (Fig. 1.3(a)), the lateral momentum of light beam reflecting at the prism-metal interface would satisfy the condition for generating SPPs at metal-air interface. For grating coupling method (Fig. 1.3(b)), wave vectors of incident light and SPPs could be matched by providing a vector from the grating[11].

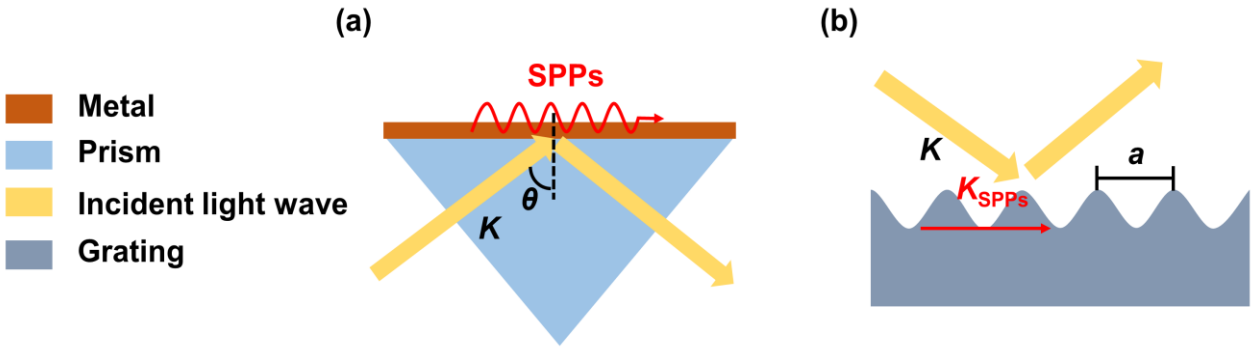

Figure 1.3 Two approaches used for the excitation of SPPs at metal-dielectric interface. (a) Prism coupler (Kretschmann configuration): Metal film is attached onto the surface of prism. Light illuminates the prism at critical angle of total internal reflection (TIR) to generate an evanescent wave that penetrates through the metal film. SPPs are generated at the outer side of the gold thin film (Au TF). (b) Grating coupler: light illuminates the grating with a constant period to activate SPPs (provide momentum match).

In comparison to SPPs which is a kind of propagating SPs, LSPs is the non-propagating SPs and usually occurs when light impinges on noble metallic nanoparticles (NPs). The generation of LSPs would confine light into nanometer scale, thus largely enhancing electric fields near NP surface and exhibiting maximum value at plasmon resonant frequency in the absorption spectra of NPs which can be tailored through changing NP shape and size[18]. Hence, localized surface plasmon resonances (LSPRs) reveals

the interaction between incident photons and surface electrons in metallic NPs (the so-called optical antennas), and exists in various surface-enhanced spectroscopic processes such as SERS and SEF[19-22]. Meanwhile, LSPRs related spectroscopies have become a powerful tool for both biological and chemical sensing due to the fact that LSPRs is very sensitive to the local environment[23-25]. Furthermore, as the interaction between the optical antennas and emitters (such as fluorescent molecule[26], quantum dots, etc.) strongly modifies the radiative character of the emitters, it is of great importance to investigate the physical mechanism of plasmon-mediated optical emissions in such a hybrid system.

1.3 Plasmon Coupling in Plasmonic Nanostructures

When two or more plasmonic nanostructures are placed close to each other, the plasmon resonance of each individual nanostructure could hybridize and generate multiple modes upon investigation[27-29]. The hybridized mode energy would either blue-shift or red-shift as a consequence of the differences in surface charge distributions of adjacent nanostructures[30-34]. For instance, in metallic bowtie nanoantennas system, the plasmonic resonance first blue-shifts as the interparticle distance increases, then red-shifts when the gap distance is further enlarged[35]. To quantitatively resolve the plasmon response in coupled NPs, plasmon hybridization model (as schematically depicted in Fig. 1.4(a)) is introduced and has been expanded to other plasmonic nanostructures such as metal particle-on-film nanocavities (MPoFNs)[36-41] and four-layer concentric nanoshell[27]. For example, in a nanosphere dimer system, the plasmon resonance in each metallic nanosphere can be expressed as $\omega_{\mathrm{NS}} = \omega_{\mathrm{p}}\sqrt{\frac{l}{2l+1}}$, where ω_{p} is the bulk plasmon frequency, l is the angular momentum representing spherical harmonics of different orders (dipole (l = 1) and quadrupole (l = 2) and higher order modes). When the distance between two NPs becomes small enough, splitting of the dimer plasmon appears and thus forming both

bonding and antibonding modes. The highest energy mode (antibonding) has no dipole moment and therefore cannot couple to incident light, leading to the "dark" optical character in the far field. While the lowest energy mode (bonding) is "bright" due to the large dipole moment.

As for another robust system (MPoFNs) which is easy to fabricate, NP couples to its image within the metal film (Fig. 1.4(b)). This plasmonic nanostructure is more like a metallic nanosphere dimer as solutions of the EM boundary conditions at the planar surface equal to an image NP within the metal. When the optical field is polarized in the substrate plane, the induced transverse plasmons which are spaced far above the metal surface induce only a weak coupling and a plasmon resonance close to that of individual Au NPs[42]. The other type of plasmon modes is sensitive to the optical field component along the dimer axis, and it is highly localized due to the relatively small cross section. Similarly, higher order plasmon modes would generate and tailor both the near- and far-field optical responses of MPoFNs[43]. In summary, this model is beneficial to understand the physical picture of hybridized mode evolution in coupled nanostructures and design various plasmonic devices.

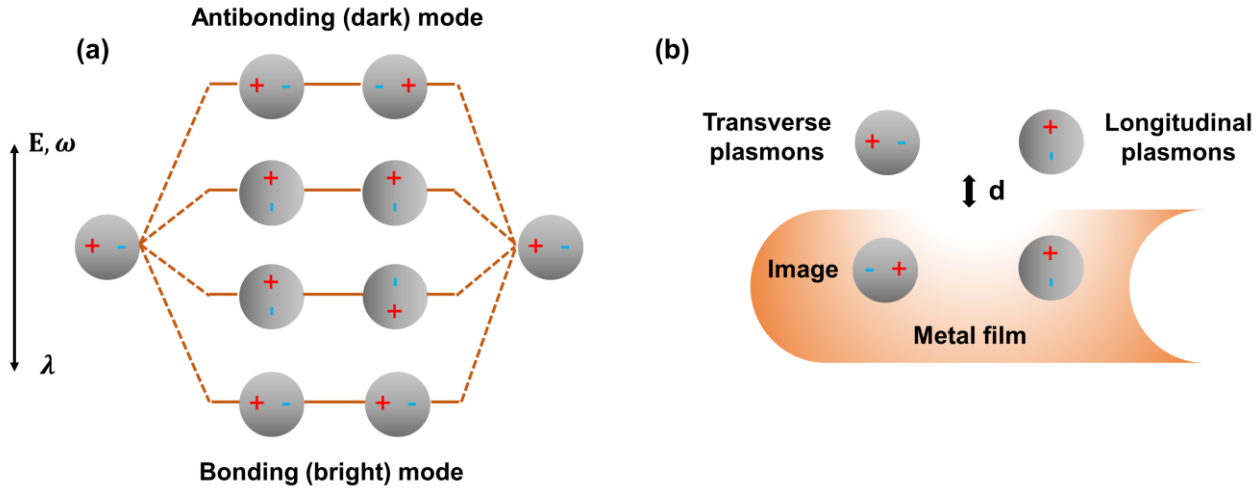

Figure 1.4 Plasmon hybridization in (a) metallic NP dimer: The dipole plasmon of individual spherical NPs is three-fold degenerate (along the three space axes). When two NPs are put closely enough, the dimer exhibits modes that result from the hybridization of that in individual NPs. The mode resides in lowest energy level is bright which leads to a large dipole moment. The highest energy mode has no dipolar moment and cannot couple to radiation (dark mode); (b) metal particle-on-film nanocavities (MPoFNs): The NP sees its reflection within the mirror and couples to it, so that each charged region generates a dipole in combination with the oppositely charged image NP.

Another intuitive model for analysing the coupled plasmonic nanostructures is the circuit model, which is utilized to investigate the optical resonance frequency regarding the morphology as well as the gap width within the coupled system[44]. In this model, the coupled nanostructures can be regarded as a circuit with resistance R and capacitance C, and plasmon resonance wavelength of a specific nanostructure can be derived by solving equations based on R-C oscillator circuit method. In particular, when the two adjacent nanostructures are separated by materials with varied refractive indices or conductivities, this model can provide an analytical solution on the spectral shift under different coupling regimes, which is helpful to guide experiments[45].

In addition to flexible modulation of plasmon resonance, plasmon coupling can also cause large near-field enhancement in the gap area, which could amplify both linear and nonlinear optical emissions[46]. Here, plasmonic coupling in metallic nanostructures is partially summarised in Fig. 1.5. With the progress of both nanofabrication and optical characterization, we could observe more interesting optical coupling in plasmonic nanostructures.

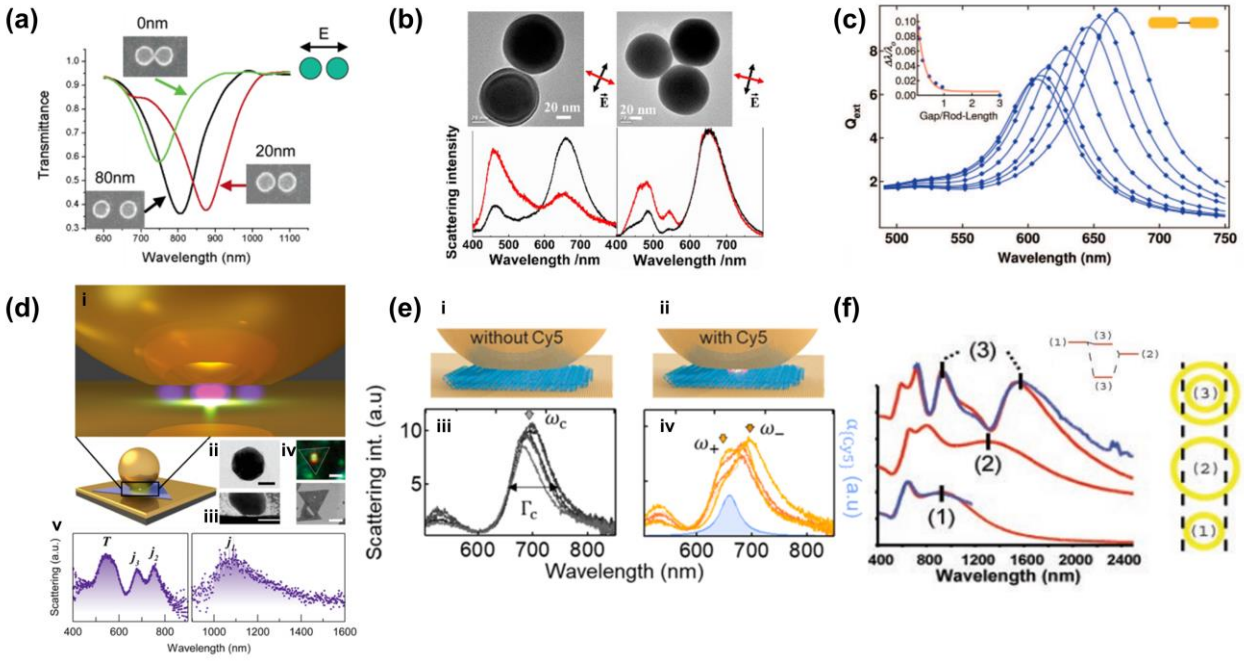

Figure 1.5 Mode hybridization via various plasmonic nanostructures. (a) Polarized transmission spectra in periodic arrays of pairwise interacting Au NPs. The lattice constant is 800 nm in parallel direction to the pair axis, 400 nm perpendicular, and the height of Au NP is 30 nm[30]. (b) Polarization-resolved dark-field scattering spectra of Ag nanosphere dimer and trimer and corresponding TEM images[47]. (c) Polarization averaged extinction of a pair of gold hemispherically-capped rods with aspect ratio 2.0 interacting end-to-end as a function of interparticle separations 56.5, 42.4, 28.2, 14.1, 7.1, 5.3, and 3.5 nm with smaller separations more red shifted. Inset: Fractional shift of the longitudinal plasmon band as a function of interparticle distance scaled for rod length. The point at Gap/Rod-Length = 3 represents the plasmon resonance of a fully decoupled rod with the same dimensions as those in the dimer[31]. (d) Scattering of NP-on-mirror (NPoM) with semiconductor nanospacers. (i) Au NP spaced above gold surface by 2-D semiconductor sheet, forming MIM cavity. (ii) TEM image of a faceted Au NP (scale bar 50 nm). (iii) Dark-field-STEM image of single NPoM cross section. The MIM cavity formed by facet and surface is clearly visible (scale bar 50 nm). (iv) Dark-field scattering and SEM characterization of NP on MoS_2 (scale bar 1 μm). (v) Dark-field scattering spectra of individual NPoMs. Labels are resonances arising from hybridized MIM cavity modes (j_1, j_2, j_3) and the transverse single NP mode (T)[48]. (e) Characterization and coherent coupling with single-Cy5 in NPoM. (i, ii) NPoM without and with Cy5 molecule in DNA origami. (iii, iv) Experimental dark-field scattering of five individual NPoMs, with resonance peaks $\omega_{c,+,-}$ and linewidths Γ_c marked. Absorption spectrum is also illustrated (blue)[49]. (f) Concentric nanoshell with dimensions $a_1/b_1/a_2/b_2$ = 80/107/135/157 nm; the inner- and outer-nanoshell plasmons interact strongly, leading to strongly hybridized plasmons[27]. Experimental (blue) and theoretical (red) extinction spectra for concentric nanoshells (3) in contrast to the inner (1) and outer (2) nanoshell plasmon resonances in various coupling regimes.

Nanostructures were derivatized with 1-dodecanethiol and either suspended in CS_2 in a 1 mm path length sealed cell or dried and mixed with KBr and pressed into a pellet to obtain the spectra. The peak positions of the dipole resonance modes are marked for clarity. The theoretical extinction spectra were calculated with a vector basis function solution of Mie scattering theory for a coated sphere. The inner-nanoshell spectra (1) were measured in solution before the growth of the a_2 and b_2 layers.

1.4 Quantum Size Effects in Plasmonic Nanogap Systems (PNSs)

As mentioned above, metallic NPs with nanometric gaps are generally regarded as plasmonic nanocavities which have intriguing virtues in terms of the ultrasmall mode volume and remarkable near-field enhancement in the gap region. Due to these advantages, plasmonic nanocavities are widely applied in the plasmon-enhanced spectroscopies such as SERS[50], plasmon-enhanced photoluminesces[51], nonlinear harmonic generations[52, 53], plasmon-exciton strong coupling[54, 55], etc. Intuitively, reducing the mode volume as far as possible would boost the near-field enhancement, which benefits the plasmon-enhanced optical phenomena. However, many recent studies have disclosed that quantum size effects such as quantum tunneling and spatial nonlocality can put a limit on both the mode volume and the near-field enhancement of individual plasmonic nanocavities with gap width approaching sub-nanometer level[56-61]. Essentially, all these quantum size effects stem from strong electron-electron interactions in the metal, resulting in large difference in optical response compared to that under classical predictions. For instance, plasmon-induced charges at the surface of two metallic nanostructures can tunnel through a barrier within the gap region[59]. Therefore, studying the impact of quantum size effect on the optical resonances of plasmonic nanocavities has become one of the main parts of quantum plasmonics[59, 62].

1.4.1 Classical Local Response

Within the classical regime, the optical response of plasmonic nanostructures can be well predicted by classical Drude model. The equation of this model can be expressed as $\nabla \times \nabla \times \mathbf{E}(\mathbf{r},\omega) = k_0^2 \varepsilon_{\mathrm{D}}(\omega)\mathbf{E}(\mathbf{r},\omega) + \mathrm{i}\omega\mu_0\mathbf{J}(\mathbf{r},\omega)$. Where k_0 is wave vector in vacuum, μ_0 is the permeability of the vacuum. For free electron gas the dielectric function $\varepsilon_{\mathrm{D}}(\omega) = 1 - \frac{\omega_{\mathrm{p}}^2}{\omega^2 + \mathrm{i}\gamma_0\omega}$, where γ_0 is collision frequency, ω_{p} is the unscreened plasma frequency, which can be calculated via $\omega_{\mathrm{p}} = \sqrt{\frac{n\mathrm{e}^2}{\varepsilon_0 \mathrm{m}}}$, in which n is the number density of free electrons, e is the electric charge, m and ε_0 are the effective mass of the electron and electric permittivity of free space, respectively.

1.4.2 Nonlocal Response

In the above discussion on classical local response of nanostructures with typical feature size $\geq \lambda/2$, the induced polarization density at a given point $\mathbf{r}$ is $\mathbf{P}(\mathbf{r}) = \varepsilon_0 \chi_{\mathrm{e}} \mathbf{E}(\mathbf{r})$, where χ_{e} is the electric susceptibility in the homogeneous material, $\mathbf{E}$ is the electric field. While as the feature size $\ll \lambda/2$ in plasmonic metallic nanostructures, description of the plasmon waves within the picture of classical EM fields would be insufficient, calling for quantum description of the plasmons. One of the quantum effects is nonlocal screening, which is also called spatial nonlocality, and can be well interpreted by the theory of surface screening. Spatial nonlocality treats electron-electron Coulomb interaction and Pauli repulsion as an electron gas pressure, excluding electron tunneling and quantum oscillations. Under this kind of microscopic description, polarization density at a given point $\mathbf{r}$ is $\mathbf{P}(\mathbf{r}) = \varepsilon_0 \int \chi_{\mathrm{e}}(\mathbf{r}' - \mathbf{r})\mathbf{E}(\mathbf{r}')dV'$, where χ_{e} is a function of $\mathbf{r}$ and thus spatially dispersive. The nonlocal response is the result of a large number of individual microscopic interactions over a certain volume surrounding the point $\mathbf{r}$[63, 64]. In addition, due to the selection of boundary conditions on the charge current[65, 66], charge distribution

spreads out in the bulk region of the metal, exhibiting both transverse and longitudinal modes under nonlocal description. While in local model the induced charge is strictly distributed along the metal-air interface[67]. (Fig. 1.6 (a, b)).

As for the models which are employed to explain the observed nonlocal response in coupled plasmonic nanostructures[68-72], the nonlocal hydrodynamic (NLHD) model is mainly used due to its high compatibility and calculation efficiency[63, 65, 73, 74]. This model can well predict the blue-shift of plasmon resonances with respect to that calculated by classical local model[57, 75].

In principle, the NLHD model can be implemented by solving the coupled Eq. (1.2) and Eq. (1.3) with an additional boundary conditions (ABC) $\mathbf{n} \cdot \mathbf{J}(\mathbf{r}, \omega) = 0$ at the boundaries of the metal, where $\mathbf{n}$ is the normal vector of the metal surface,

$$\nabla \times \nabla \times \mathbf{E}(\mathbf{r}, \omega) = k_0^2 \varepsilon_{\text{core}}(\omega) \mathbf{E}(\mathbf{r}, \omega) + \mathrm{i}\omega\mu_0 \mathbf{J}(\mathbf{r}, \omega) \tag{1.2}$$

$$\beta^2 \nabla[\nabla \cdot \mathbf{J}(\mathbf{r}, \omega)] + \omega(\omega + \mathrm{i}\gamma_0)\mathbf{J}(\mathbf{r}, \omega) = \mathrm{i}\varepsilon_0 \omega \omega_{\text{p}}^2 \mathbf{E}(\mathbf{r}, \omega) \tag{1.3}$$

Here k_0 is the wave vector in a vacuum, $\varepsilon_0(\mu_0)$ is the permittivity (permeability) of the vacuum, $\varepsilon_{\text{core}}(\omega)$ is the local permittivity of gold responsible for the bound ions and electrons, and β is the nonlocal screening parameter; γ_0 and ω_{p} are the collision and plasmon frequency of the Drude model, respectively. β is related to the Fermi velocity of gold, v_{F} = 1.39×10^6 m/s via $\beta^2 = 3v_{\text{F}}^2/5$. $\varepsilon_{\text{core}}(\omega)$ of gold is obtained by subtracting the Drude part from the empirical data, i.e., $\varepsilon_{\text{core}}(\omega) = \varepsilon_{\text{m}}(\omega) + \frac{\omega_{\text{p}}^2}{(\omega^2 + \mathrm{i}\gamma_0\omega)}$, where $\varepsilon_{\text{m}}(\omega)$ is the experimentally measured permittivity of real metals[64].

Recently, the study on spatial nonlocality has been conducted in various plasmonic nanostructures, such

as dimers (Fig. 1.6(c)), metallic cylinders (Fig. 1.6(d)) and MPoFNs (Fig. 1.6 (e, f)), which will trigger a great deal of applications in the field of quantum plasmonics.

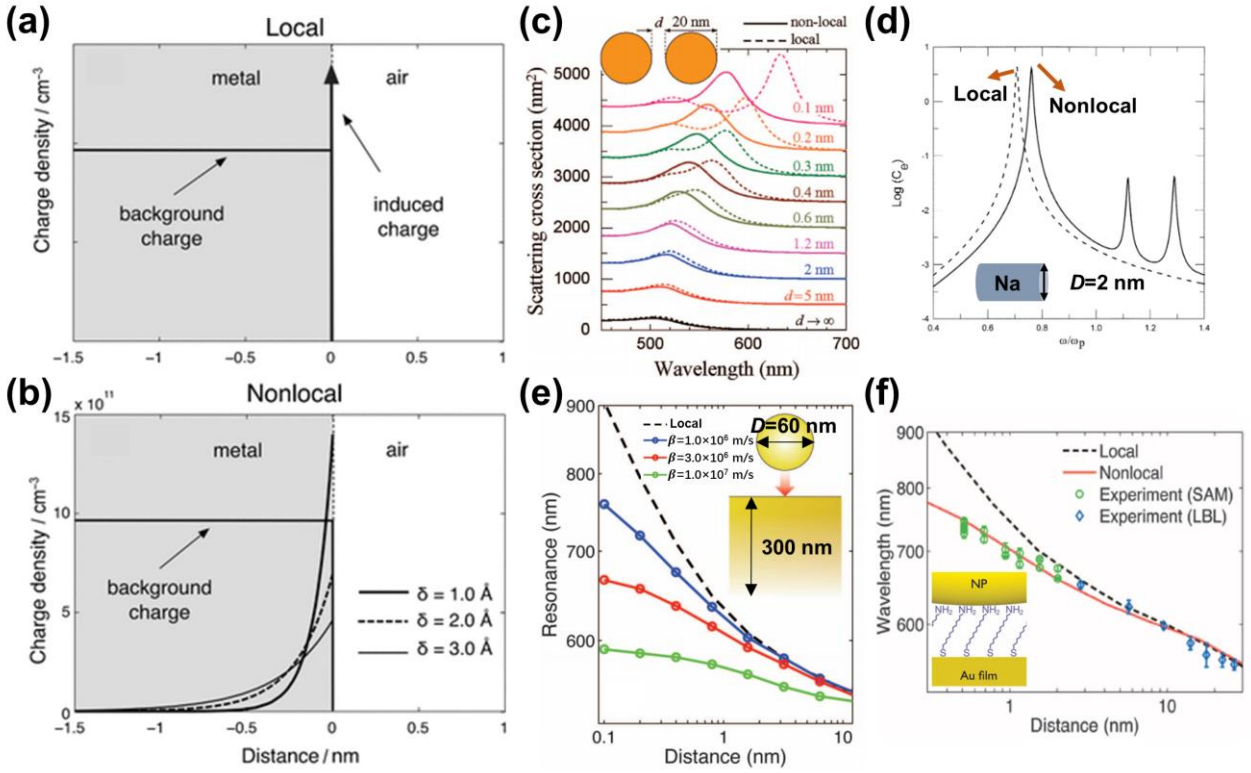

Figure 1.6 Spatial nonlocality in metallic nanostructures. (a, b) Induced electron density as a function of position at the interface between a metal nanowire and the vacuum[67]. The metal–air interface is centred at $x = 0$. Assuming a local description (a), the induced charge density decreases to a Dirac delta function at the metal-air interface. In the framework of the hydrodynamic model (b), the induced charge density spreads out in the bulk region of the metal along a distance determined by the nonlocal parameter $\delta = \beta/\omega_p$; (c) Extinction spectra of dimers formed by spherical gold particles of 20 nm in diameter[63]. Local (dashed curves) and nonlocal (solid curves) calculations are compared for several separations between the particle surfaces, d. Consecutive curves are offset vertically by 500 nm^2 for clarity. The external electric field is parallel to the interparticle axis. (d) Extinction width, in units of the geometric width, of a Na cylinder of radius 1 nm, in a medium with $\varepsilon_m = 1$, (full curve). The dashed curve shows the result of the local theory[76]. (e, f) Behavior of the film-coupled nanosphere, assuming a local and nonlocal model with different values of β, as a function of separation distance[57]. Calculations refer to a gold nanosphere (Au NS) of radius $r = 30$ nm on a film with 300 nm thickness. (e) Resonance peak position as a function of gap distance. (f) Comparison between numerical calculations with $\beta = 1.27 \times 10^6$ m/s and experimental results from SAM- and LBL-type spacers. Inset: Schematic of the MPoFN spaced by an amine-terminated

alkanethiol self-assembled monolayer (SAM). Note that in the absence of nonlocal screening, the peak scattering wavelength is extreme; nonlocality places a limit on the ultimate enhancement.

1.4.3 Vacuum Tunneling and Molecular Charge Transport

In addition to nonlocal effect, quantum tunneling is another quantum size effect which plays a major part in the investigation of optical characteristics of coupled metallic NPs with sub-nanometer gap size. In 2012, Esteban *et al*. carried out a theoretical study on the near- and far-field optical responses of metallic dimers with sub-nanometer vacuum gaps (see Fig. 1.7(a)), in which quantum-corrected model (QCM) is proposed based on time-dependent density functional theory (TDDFT). This model could be employed to investigate quantum tunneling process within classical framework[77], which opens a new avenue to solve the quantum tunneling issue in plasmonic nanocavities. After that, Savage *et al*. used two atomic force microscopy (AFM) tips to precisely control the distance between the coupled metallic NPs (as shown in Fig. 1.7(b)), and found that quantum tunneling become the dominant effect when the space between the two tips was reduced to 0.3 nm, which is highly consistent with the calculations based on QCM[78]. Scholl *et al*. also proved the quantum tunneling effect in the dimers and trimers formed by silver nanospheres with the help of transmission electron microscope (TEM) and electron energy loss spectroscopy (EELS)[60, 79]. So far, numerous similar experimental and theoretical studies have clarified the influence of quantum tunneling effects on resonance wavelength of plasmonic nanocavities. Specifically, the tunneling current will short circuit the coupling between metallic NPs, thus leading to the transition from bonding dipolar plasmon (BDP) mode to charge transfer plasmon (CTP) mode, and large reduction of the local field inside the nanocavities.

Apart from coupled NPs with vacuum gap, molecular self-assembly method (SAM) is usually employed in the preparation of plasmonic nanocavities with sub-nanometer gaps. Under this circumstance, electrons would tunnel through the molecular junctions between metallic nanostructures, which is more sophisticated than that through vacuum gap. On the one hand, the charge transfer mechanism has been extensively studied in the metal-molecule-metal nanojunctions under an applied direct current (DC) bias. Back in 2004, Kushmerick *et al*. studied the resonant charge transport in the metal-molecule-metal nanojunctions under applied bias, which indicates the strong coupling between tunneling charge carriers and the longitudinal vibration mode of molecules[80]. Subsequently, together with the electronic structures of metal-molecule-metal junctions, Kim *et al*. investigated the influence of metal work function, surface anchoring groups and molecular length on molecular tunneling process[81]. On the other hand, plasmonic nanocavities with molecular junctions offer a solution to the mechanism of charge transport through molecular junctions at optical frequencies. The representative work is the EELS study on the plasmon resonances of the plasmonic nanocavity formed by silver NP dimer with the monolayer molecular junctions. The results indicate that charge transport can take place at a relatively large gap distance by means of molecular frontier orbital. The CTP mode also appears within the Ag-molecule-Ag nanojunctions as a result of the quantum tunneling effect[82]. González *et al*. conducted a systematic study on the relationship between optical properties of the molecule-bridged dimer nanocavity and its molecular conductance based on QCM, and derived the threshold molecular conductance under the generation of CTP mode[83] (Fig. 1.7 (c, d)). In addition to NP dimers, MPoFNs and Au core-molecule-shell nanostructures are also employed to investigate charge transport across molecular junctions. In this respect, both theoretical and experimental studies were conducted on the higher order CTP mode induced by quantum tunneling effect in the MPoFN and its influence on Fano resonance[84]. Besides, a type of hot

electron-mediated resonant charge transfer process was also proposed in Au core-molecule-shell nanostructures with the help of SERS[85].

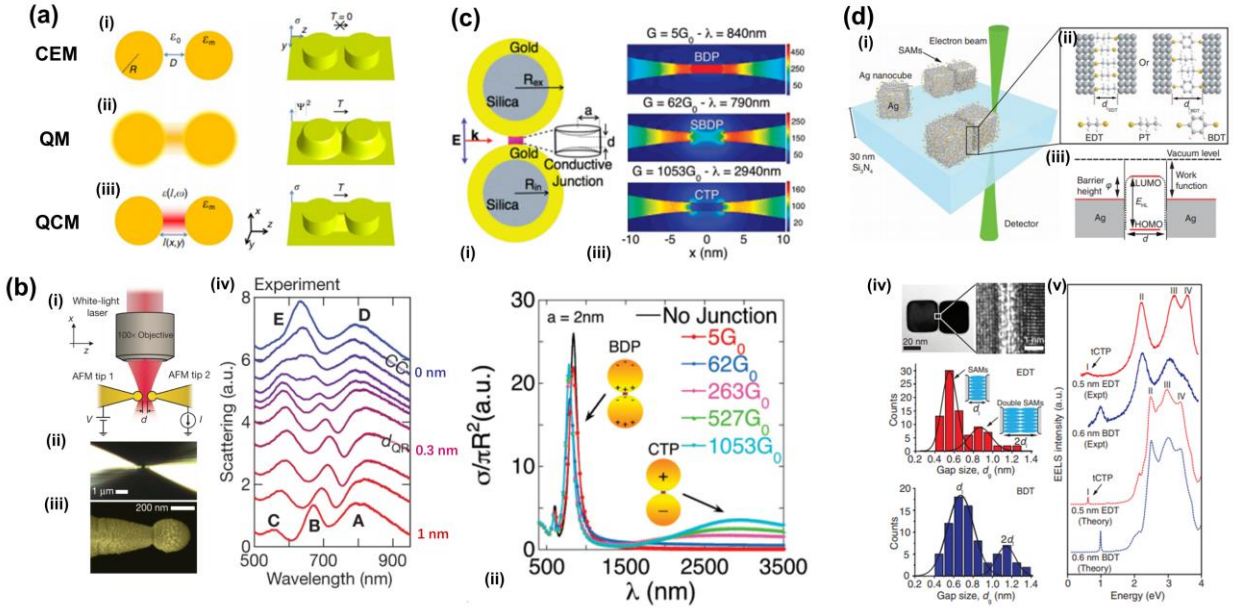

Figure 1.7 Quantum tunneling and charge transport in metallic nanostructures. (a) Investigation of the material properties of a metallic dimer using both classical and quantum models[77]. Schematics of a metallic dimer formed by two spherical NPs with gap width D under (i) CEM, (ii) QM and (iii) QCM. The schematics demonstrate the change of the dielectric characters of the materials at the boundaries of the dimers. The joint sketches show the corresponding absolute value of the conductivity σ (i, iii) and electron density distribution $|\Psi|^2$ (ii). Within the classical regime (i), the conductivity is different from zero only inside the nanospheres and no electron transfer can occur between the NPs (electron tunneling probability $T = 0$). In a fully quantum mechanical treatment (ii), the electron densities in the gap is non-zero for small D and electron can transfer between the NPs ($T > 0$). In the QCM (iii), the electron tunneling is accounted for by describing the material in the junction with a fictitious dielectric medium (illustrated by a shaded red color) characterized by a local dielectric permittivity $\varepsilon(l(x,y),\omega)$ that depends only on the local width $l(x,y)$ of the junction and the NP material at both sides. (b) (i), Scheme for simultaneous optical and electrical measurements of plasmonic cavity formed between two Au-coated tips, shown in dark-field microscope images (ii) and false-color scanning electron microscope image (iii) of a typical tip, end radius $R = 150$ nm. (iv), Selected experimental spectra from the last 1 nm to contact, shown vertically shifted[78]. (c) (i) Schematic illustration of the PCC[83]. A nanoshell dimer connected by a cylindrical conductor of radius a and internal length d. The radius of the

silica core is R_{int} = 45 nm, the outer gold surface R_{ext} = 55 nm. k is the wavevector of the incident EM wave. (ii) Extinction spectra of a PCC for a = 2 nm as a function of junction conductance. Insets illustrate the charge distributions for the BDP and the CTP. (iii) Near-field maps at the resonance wavelengths for some of the systems in (ii): BDP at λ = 840 nm (top); SBDP at λ = 790 nm (middle); CTP at λ = 2940 nm (bottom). (d) (i-iii) Quantum plasmonic tunnel junctions. (i) Schematic illustration of the molecular tunnel junctions made of silver nanocube dimers connected by a SAM on an electron-transparent silicon nitride membrane. The contactless electron nanoprobe was placed near the functionalized silver NPs to excite and measure the surface plasmons of individual dimers. (ii) The distance between two adjacent NPs is defined by the thickness of the SAMs of EDT or BDT. (iii) A schematic energy-level diagram of the junctions. (iv-v) Direct observation of quantum tunneling between plasmon nanostructures. (iv) A high-resolution TEM image of the molecular junctions and histograms of the gap sizes. (v) Two examples of measured EELS spectra with the occurrence of quantum tunneling directly observed by the tCTP peak and quantum-corrected simulations of the extinction spectra, confirming the identification of the peaks[82].

1.5 Two-Photon Photoluminescence in Metallic Nanostructures

In the past few decades, exploring nonlinear optical properties in metallic nanostructures has also become a research hotspot in the field of plasmonics. In this context, plasmon-mediated nonlinear optical responses including second-harmonic generation (SHG), third-harmonic generation (THG), four-wave mixing (FWM) and two-photon photoluminescence (TPL) were widely investigated in different plasmonic nanostructures[86-90].

As one of the nonlinear optical phenomena, TPL occurs by absorbing two low energy photons with short-lived intermediate states. After excitation process, the fluorophore relaxes to the lowest energy level of the first excited electronic states through vibrational processes, followed by the subsequent fluorescence emission process (as schematically and experimentally demonstrated in Fig. 1.8 (a, b)). In addition, TPL

is a third-order nonlinear phenomenon and scales quadratically with the intensity of the incident light wave[91]. Therefore, TPL is very sensitive to plasmon resonance in metallic nanostructures. Previous studies have indicated that Au nanosphere usually exhibits weak TPL response due to its small two-photon absorption cross section as well as low emission quantum yield. While anisotropic Au nanorod exhibits strong TPL emission due to the lightening rod effect[92, 93].

Recently, coupled nanostructures (aggregated metal NPs) are well-known for generating strong TPL[87, 94, 95], which can be applied in two-photon bio-sensing and bio-imaging[96, 97]. The observed strong TPL can be attributed to local field enhancement resulting from the longitudinal plasmon resonance of these nanostructures at the wavelength range coinciding with the excitation wavelength. Besides, recent study shows that TPL intensity of Au NP clusters significantly rises from monomer to linear trimer, which results from strong interaction between TPL and longitudinal plasmon resonance modes of Au clusters. Moreover, the TPL spectra of these single Au nanosphere clusters behave similarly as their corresponding scattering spectra, indicating strong correlation between their TPL and plasmon resonance[98] (Fig. 1.8(c, d)). Up to now, various approaches have been employed to explore TPL mechanisms within plasmonic nanostructures, including two-pulse emission modulation (TPEM) and pump-probe measurements[99].

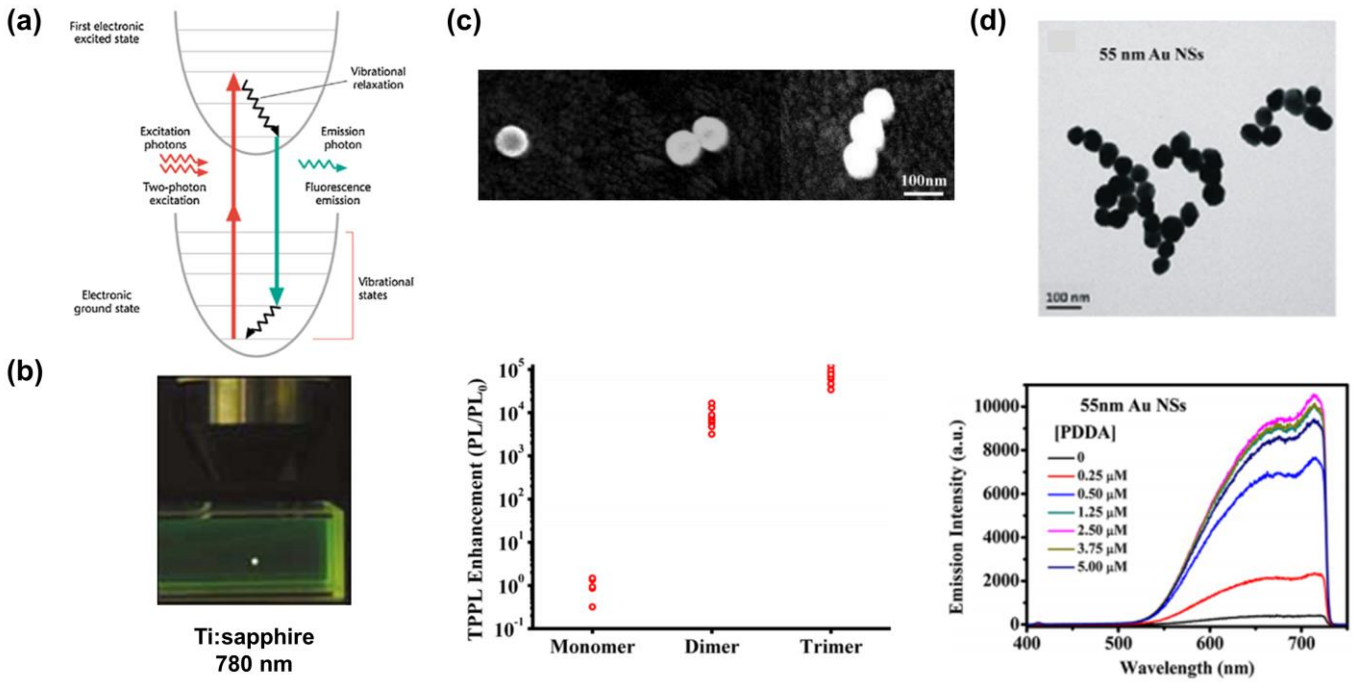

Figure 1.8 (a) Jablonski diagrams of two-photon photoluminescence (TPL), which occurs when fluorophores are excited from the ground state to the first electronic states[100]. (b) Experimental illustration of TPL[101]. Because of the quadratic relationship between the excitation intensity and fluorescence emission, light is emitted only at the focal point of the focused laser beam. (c) SEM image and statistics of relative TPL emission intensity of Au NS monomers, dimers, and linear trimers[98]. (d) TEM image and TPL spectra of 55 nm Au NSs under different concentrations of poly(diallyldimethylammonium chloride) (PDDA)[94].

Chapter 2 Plasmonic Nanostructure Fabrication and Characterization

2.1 Preparation of Graphene-Sandwiched Plasmonic Metal Particle-on-Film Nanocavities (MPoFNs)

To fabricate graphene-coupled MPoFNs, a gold mirror is needed. Here, thermal evaporation procedure of Au film was schematically shown in Fig. 2.1(a). The source (bulk Au) in crucible was heated in high vacuum chamber (10^{-7} Torr level), vaporized and eventually reached the substrate (silicon wafer) to form Au thin layer. The evaporation rate and vacuum level mainly determines the roughness of the Au film. While the thickness of Au film was tuned by changing the exposure time of the substrate to the source. Figure 2.1(b) demonstrates AFM characterization of Au thin film (about 100 nm thickness) which was prepared by thermal evaporation on a silicon wafer at a deposition rate of ~ 1 Å/s. Besides, electron beam (E-beam) evaporation is another gold film evaporation approach, in which the resistive heating filament is replaced with an electron gun which emits high-energy electron beam.

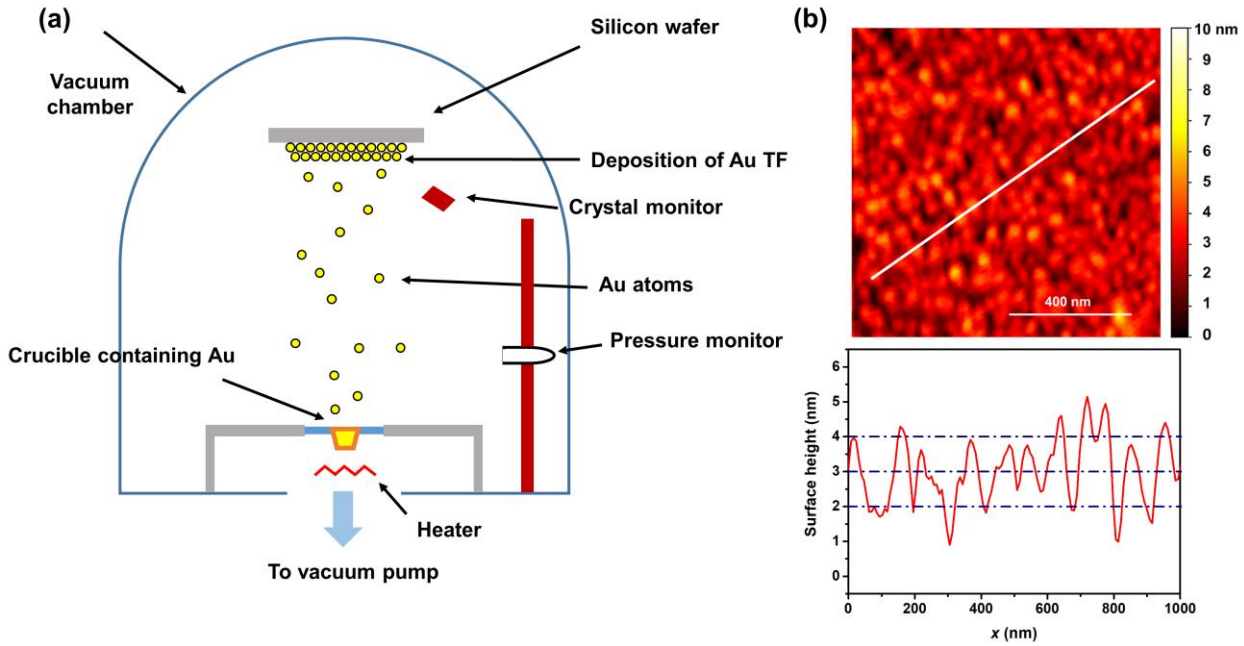

Figure 2.1 (a) Schematic of thermal evaporation of gold film. (b) Atomic force microscope characterizations of Au TF prepared via above approach. The root-mean-square (RMS) roughness was determined to be 0.9 nm, and gold deposition rate is 1 Å/s.

To further reduce roughness of the prepared Au TF, template stripping method[102] was investigated and widely applied to form the well-defined plasmonic nanocavities. Figure 2.2 is the flow chart of the whole process in Au TF preparation. Briefly, a gold thin layer was deposited on a silicon wafer by E-beam evaporation, then glued to glass slides using UV sensitive adhesive (Norland Optical Adhesive 61, Norland Products), then the adhesive was cured by about 30 minutes under UV light exposure. After peeling off the film from silicon wafer, we could obtain a fresh Au TF with ultrasmooth surface.

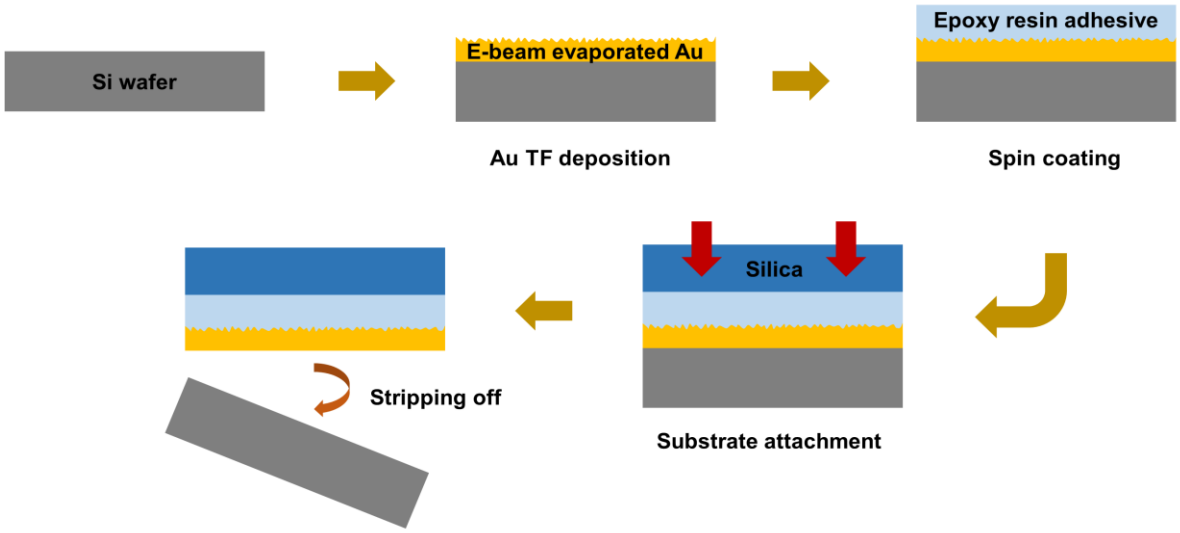

Figure 2.2 Schematic of the template stripping method employed to prepare ultrasmooth gold film.

After the preparation of smooth Au TF, large-area graphene flakes with various number of layers were grown on a copper substrate by chemical vapor deposition. The copper substrate was then spin-coated with poly (methyl methacrylate) (PMMA) at 3000 revolutions per second (rps). The copper substrate (with PMMA-covered graphene flakes) was then put into a 10% $FeCl_2$ solution for 2 h. After the dissolution of copper, the remaining PMMA/graphene film was transferred onto the Au TF. The whole sample was then kept in acetone for 2 h for dissolving the PMMA layer. Colloidal Au NSs of 80 nm diameter (NanoSeedz) were stabilized in an aqueous solution of cetyltrimethylammonium bromide (CTAB). The Au NSs were washed twice by centrifugation, before being re-dispersed in H_2O and drop-casted on the graphene/Au TF sample and subsequently dried in air at room temperature to produce graphene-sandwiched MPoFNs. The whole process is schematically shown in Fig. 2.3.

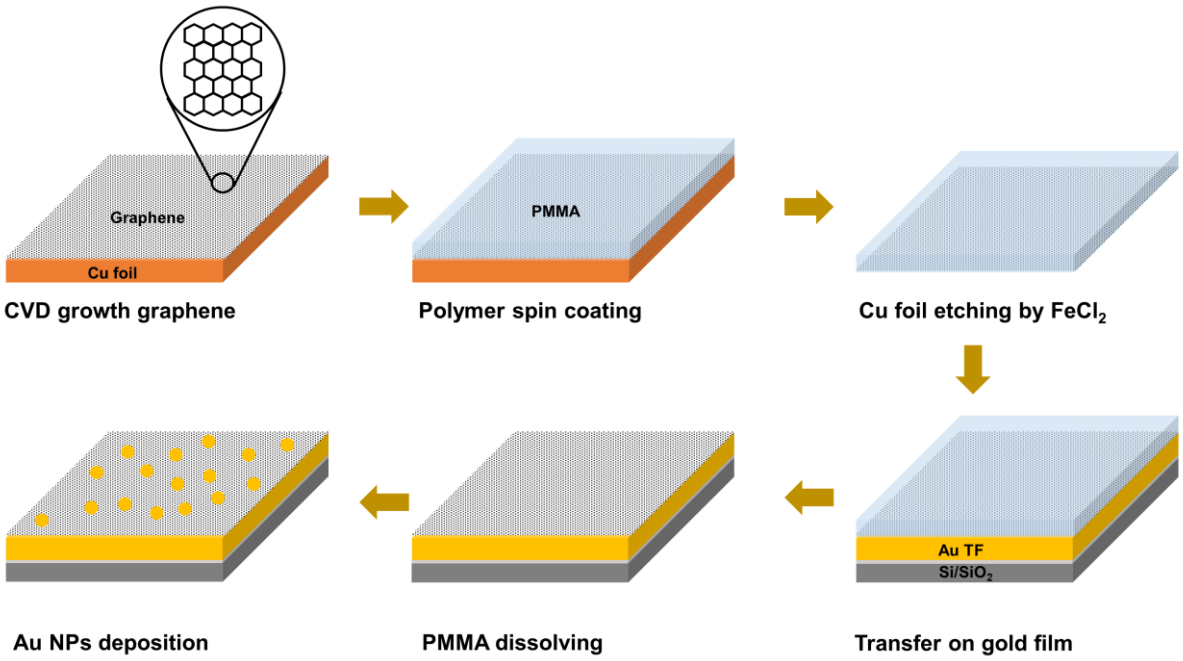

Figure 2.3 Flow chart of preparation for graphene-sandwiched MPoFNs.

2.2 Synthesis of Gold Sphere Plasmonic Nanomatryoshkas (GSPNs)

The 20 nm Au cores were firstly synthesized by the seed-mediated method. The obtained cetyltrimethylammonium chloride (CTAC)-capped Au cores were washed once and re-dispersed in water. The molecule powder was dissolved in ethanol. Then 50 μL of molecule ethanol solution (1 mM) were slowly added to the 1 mL of Au core (1 nM) colloids under vigorous ultra-sonication. The mixtures were then incubated for different time durations of 0.5, 3, and 9 hours, for samples with 1,4-benzenedithiol (BDT), 4,4'-biphenyldithiol (BPDT), and 4,4'-terpheyldithiol (TPDT) molecules, respectively. After that, the molecule-modified Au cores were centrifuged and washed by water to remove excess molecules. The Au core-shell NPs were prepared by adding 190 μL of molecule-modified core colloids into the aqueous mixture of 4 mL CTAC solution (0.1 M), 200 μL of ascorbic acid (0.04 M), and 200 μL of $HAuCl_4$ (4.86 mM). Finally, the obtained GSPNs were washed and kept in CTAC solution (0.08 nM) (Fig. 2.4).

Then, these synthesized GSPNs with varied molecular nanojunctions were washed by centrifugation and then re-dispersed in H_2O before drop-casting onto the glass substrate and subsequently dried in air at room temperature to do the optical characterization[103]. The refractive indices of the BDT and BPDT (TPDT) molecular layers were quantified as 1.59 and 1.65 (1.65), respectively, by fitting experimental and calculated shifts of plasmon resonance of the NPs using the least squares method[104].

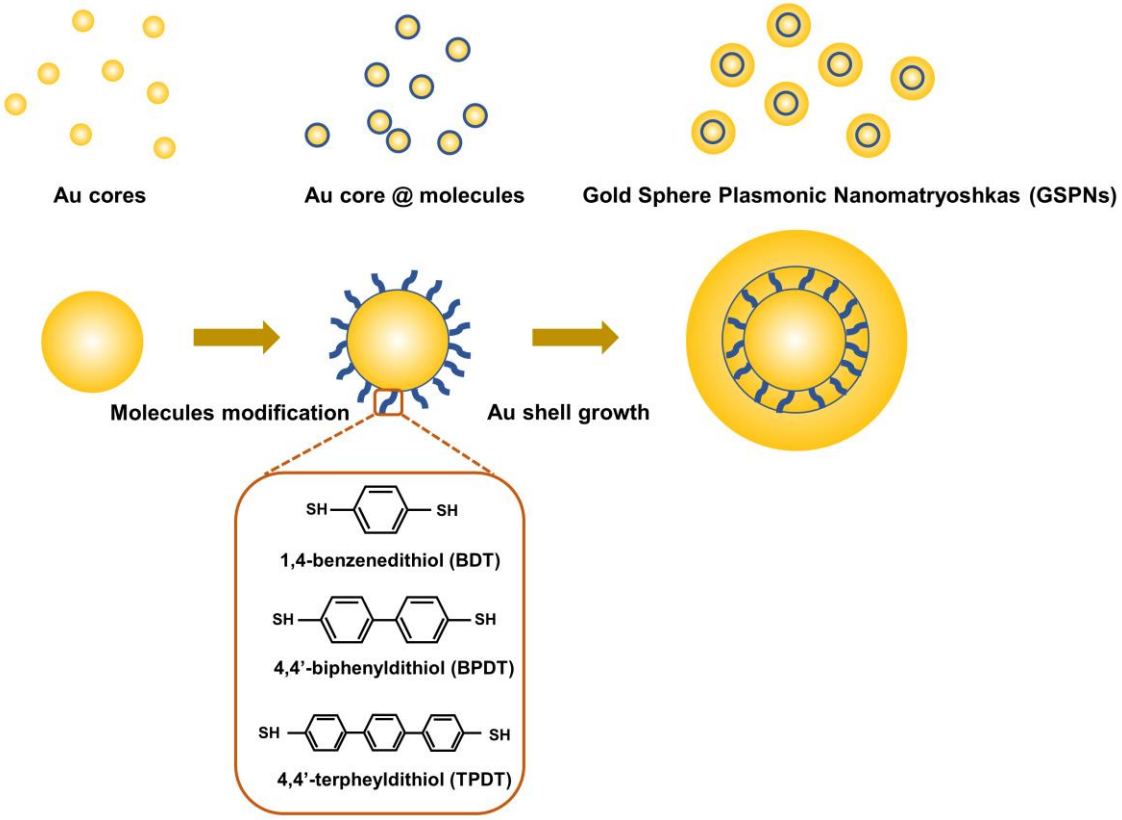

Figure 2.4 Schematic of the synthesis process for gold sphere plasmonic nanomatryoshkas (GSPNs).

2.3 Synthesis of Molecule-Decorated Au NPs

The Au NSs were synthesized using a reported method[105] with diameters about 88.6 nm. All Raman molecule powders were dissolved in ethanol. Then a certain volume (500-1000 μL) of 5 mM BDT;

BPDT; biphenyl-4-thiol (B4T) and 4-methylbenzenethiol (MBT) molecules solution were slowly added to the 5 mL Au NS (0.01 nM) solution under vigorous ultrasonication for 30 minutes, respectively. The mixtures were then thoroughly washed by water and finally dispersed in CTAC (5 mM) aqueous solution.

2.4 Synthesis of Photoswitchable Molecule-Sandwiched MPoFNs

I have prepared a type of particle-on-film nanocavities by linking Au NSs on the Au TF with a self-assembled monolayer (SAM) of host-guest molecular complex. Ultrasmooth Au TF was fabricated via template stripping method (see Fig. 2.2). Then the thio-β-cyclodextrin (thio-β-CD) (host) and diarylethene (1,2-Bis[2-methylbenzo[b]thiophen-3-yl]-3,3,4,4,5,5-hexafluoro-1-cyclopentene) (guest) molecules were both dissolved in dimethylformamide (DMF) with concentration of 5.66×10^{-4} M. Next, two of the target molecules were mixed together, followed by sonication for several minutes to encapsulate the diarylethene molecule in thio-β-CD cavity.

The Au TF was functionalized with a SAM of the host-guest molecules by simply immersing the film in the solution for overnight, followed by rinsing with DI water and blow-drying with high-purity nitrogen. Finally, the CTAB-capped Au NSs with about 80 nm diameter was drop-cast on the functionalized Au TF. After keeping the drops of NP solution on the film for several minutes, the sample was blow-dried with nitrogen flow to remove additional solution and therefore avoid unwanted aggregation of NPs.

2.5 Ultraviolet-Visible (UV-Vis) Spectroscopy

Ultraviolet-visible (UV-Vis) absorption spectroscopy is a type of spectroscopy that measures the absorbance of light after it passes through an analyte (solid or solution) at a certain wavelength. The light source of the UV-Vis spectrophotometer (as schematically shown in Fig. 2.5) covers UV to visible frequencies of EM spectrum, which is able to influence the excitation of electrons from the atomic or molecular ground state to higher energy levels and results in an absorbance at wavelengths specific to each molecule.

When the incident light passes through an analyte with a specific path length, part of the light is absorbed and the remainder transmits through it. Therefore, the absorbance of a sample can be defined as $A = -\log(T)$, $T = I/I_0$, where transmittance T is the ratio of the transmitted light intensity I to the incident light intensity I_0 at the particular wavelength. In addition, from Beer-Lambert Law the absorbance of a sample can be written as $A = \varepsilon \cdot L \cdot c$, where ε and c are the absorptivity and concentration of the sample, respectively; L is the distance of the light travels through the sample. As both ε and L are constant, A is proportional to c, i.e. $A \propto c$. Based on above analyses, quantitative determination of the analyte can also be carried out via UV-Vis spectroscopy.

Moreover, as extinction spectrum reveals the electronic transition and absorption band of the compounds under EM wave continuous spectrum illumination, UV-Vis spectroscopy is normally used to investigate the optical resonance of Au colloids. Inset in Fig. 2.5 illustrates the typical measured extinction spectrum of 60 nm Au nanospheres solution, which exhibits a broad band and the peaks at 538.5 nm.

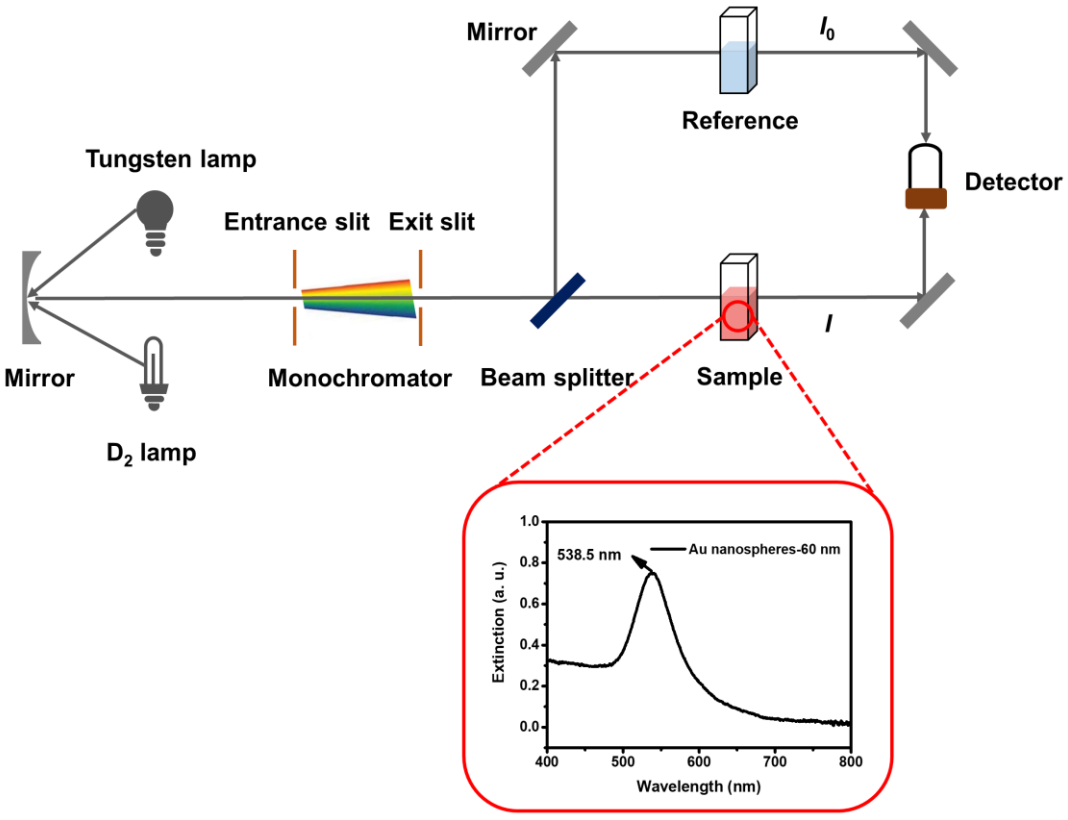

Figure 2.5 A schematic diagram of double-beam UV-Vis spectrophotometer: The light source is generally a tungsten lamp for the visible region of the spectrum, and a deuterium or hydrogen lamp for UV wavelengths. Then the monochromator can produce a beam of monochromatic illumination from incident light by either a prism or diffraction grating based dispersion system. After that, a beam of radiation from a monochromator is split into two separate beams before reaching to the sample and reference cell with about 1 cm thickness. Lastly, the two half beams passed through the detector (usually photomultiplier, silicon diode and the diode array). Inset shows the measured extinction spectrum of 60 nm Au nanospheres solution.

2.6 Single-Particle Dark-Field Spectroscopy

In the last decades, there is a great interest in studying dark-field microscopy of various nanostructures. Due to the high signal-to-noise ratio and contrast of dark-field microscopy, a bunch of researches regarding live biological samples and optical scattering properties of Au NPs are becoming promising topics. The main difference between dark- and bright-field microscopy lies in the illumination part, in

which central incident beam is blocked and focused by condenser lens, leading to outer ring of illumination within dark-field microscopy. While for bright-field illumination light source direct goes to sample after being focused by objective lens. Specifically, when investigating linear scattering characters of individual Au NPs, it is critical to collect only the signal from Au NPs and exclude scattering from nearby nanostructures or the substrate. Figure 2.6 illustrates two types of dark-field illumination configurations (reflection (a) and transmission (b)). Firstly, center of the lamp source was blocked such that the Au NPs were illuminated by the incident light at high angles. Then the non-interaction light would keep the same high angles as it either reflects or transmits on the Au NPs. While the scattered light will be collected by objective and finally reach to the detector (CCD camera).

In my single-particle dark-field imaging and spectroscopy, a customized Olympus BX51 upright microscope paired with a 100× dark-field objective (LMPlanFLN-BD, NA=0.8) was utilized to focus white-light beam from an incandescent lamp onto the sample plane. Scattered light was collected through the same objective and analyzed with an imaging spectrometer (Acton SP2300, Princeton Instruments) equipped with a gray CCD camera (PIXIS: 400BR eXcelon, Princeton Instruments). Moreover, this system could combine with the oblique illumination module to realize polarized excitations on individual Au NPs.

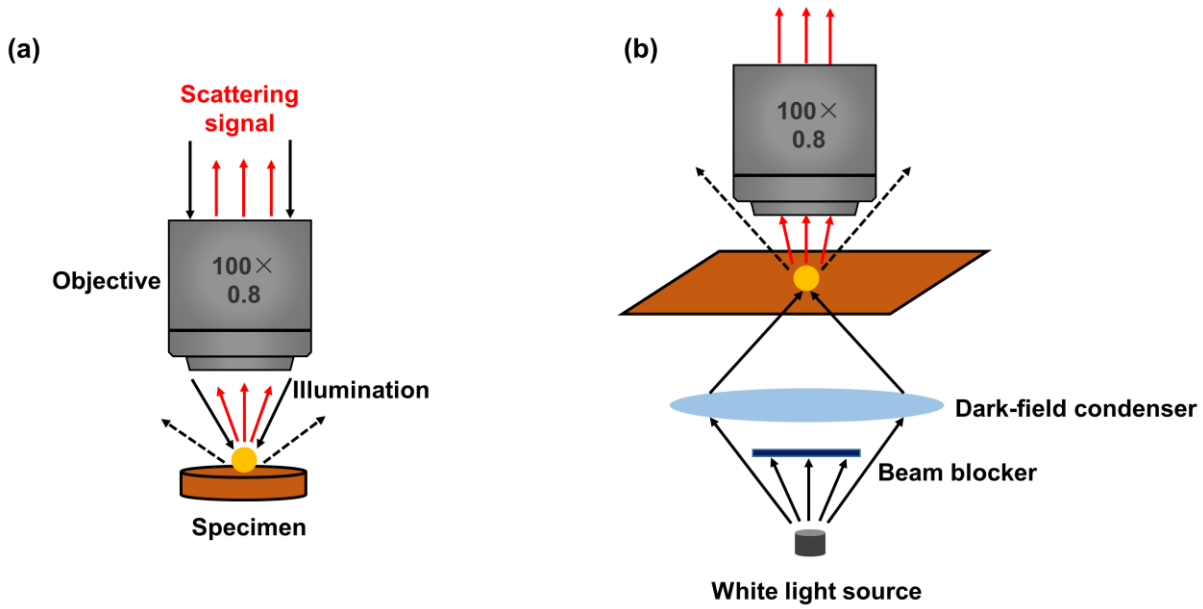

Figure 2.6 Schematic illustration of (a) reflected and (b) transmitted dark-field microscopy. The incident light hits the substrate at high enough angles such that the collective objective cannot capture any non-diffracted light.

2.7 Raman Spectroscopy

Raman and SERS spectroscopy were collected with a WITec alpha300 M+ confocal Raman microscope (WITec GmbH) equipped with a 633 nm He−Ne gas laser (Fig. 2.7). The incident laser power was fixed at 3 mW for graphene Raman and 0.3 mW in the SERS measurements, in order to suppress laser-induced thermal effects or photodamages. A diffraction-limited spot size of ~ 340 nm in radius was obtained for the incoming 633 nm laser beam through a 100× objective (NA = 0.90). Raman scattered light was dispersed by a high-resolution grating of 300 grooves/mm and then analyzed by a 600 mm focal length spectrometer (UHTS 600).

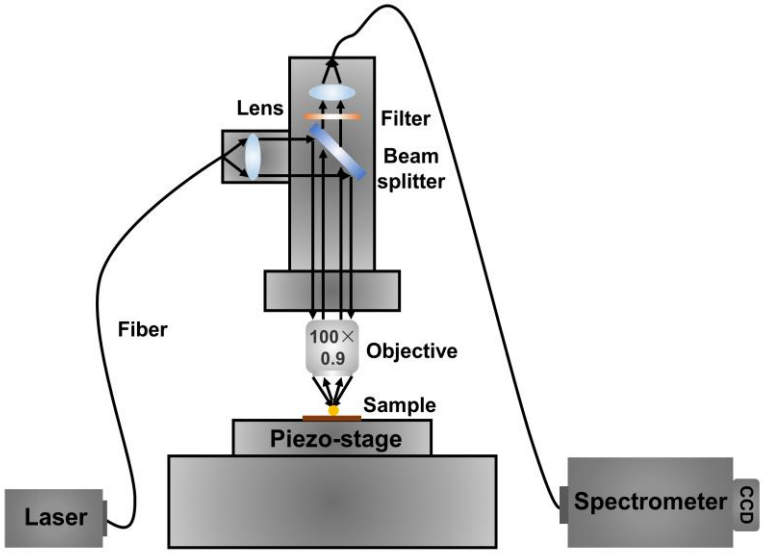

Figure 2.7 Experimental setup for the confocal Raman microscopy.

2.8 Confocal Nonlinear Optical Spectroscopy

TPL emissions from individual nanomatryoshkas are tested on a commercial laser scanning confocal microscope system (TCS SP8, Leica) combined with a mode-locked Ti:sapphire femtosecond laser (Mai Tai HP, Spectra-Physics). The pulse duration and repetition rate of the femtosecond laser is about 100 fs and 80 MHz, respectively. The laser beam is tightly focused by a dry 100× objective with a high NA of 0.95. The scanning of the laser beam at the focal plane is controlled by the scan field rotation module. After continuous scanning over the sample, TPL emission signals are detected by a HyD detector.

Chapter 3 Passive Control of Light Scattering and Raman Enhancement in Graphene-Sandwiched Plasmonic Metal Particle-on-Film Nanocavities (MPoFNs): Spatial Nonlocality Effect

There is growing interest in studying light−matter interactions at the nanoscale in recent years. One of the important themes in this research field is to investigate light localization in MPoFNs, which can confine light into the small gap area and lead to field enhancements by several orders of magnitude[11, 106]. Such a highly-localized light in the gap region enables strong light−matter interaction, thus reflecting fundamental properties of individual plasmonic junctions[48, 107, 108]. According to the classical EM theory, which is interrogated by a local model, reducing gap size in MPoFNs would eventually result in a continuous increase of near-field enhancements and red-shift of plasmonic modes[45, 59, 109]. However, when the gap width approaches nanometer or even sub-nanometer level, quantum mechanical effects including spatial nonlocality and electron tunneling gradually appear and change the far- and near-field optical response of MPoFNs[110, 111]. Previous studies indicate that the charge spill-out of electrons leads to quantum tunneling at extremely small gaps between metallic NPs. Above the quantum tunneling scale, spatial nonlocality plays a major part in the optical properties of the metallic NPs. As one of the quantum mechanical effects, spatial nonlocality can be interpreted under the theoretical framework of surface screening[70, 112-114]. Different models such as the non-retarded specular reflection model and retarded hydrodynamic model were employed to describe the conduction electron movement at sub-nanometer gaps[5, 72]. Among them, the most common approach applied to describe spatial nonlocality is the nonlocal

hydrodynamic (NLHD) model (as mentioned in Section 1.4.2) resulting from its high precision and easy implantation with commercially numerical codes[63, 65, 73, 74]. In this model, the movement of free electrons is not defined solely by the local field at a specific point, but by the integration of the adjacent electric field. Therefore, NLHD model can well predict the observed blue-shift of plasmon modes in contrast to the classical local model, which is the result of surface charge thickening[57, 115].

As stated above, quantum mechanical effects, such as spatial nonlocality and electron tunneling, in both far- and near-field optical properties of PNSs have been observed and analyzed[57, 78, 82, 116, 117]. In the far-field regime, dark-field scattering spectroscopy at single NP level has been used to investigate the spatial nonlocality-induced red-shift saturation of plasmon resonance with reducing the thickness of molecular spacer between Au TF and Au nanosphere[57] and also the electron tunneling-induced occurrence of a CTP mode in a pair of gold-coated AFM tips with sub-nanometer gaps[78]; Meanwhile, EELS has been employed to observe and analyze quantum plasmon resonances in small silver NPs with diameters down to 1.7 nm[116] and also molecular nanojunction controlled tCTPs[82]. In the near-field regime, nonlinear optical spectroscopy[117] and SERS[56, 118, 119] have been taken as indirect approaches to study the influence of those quantum mechanical phenomena quantitatively, especially the plasmonic near-field enhancement limit, in different plasmonic nanostructures. In particular, SERS of graphene and two-dimensional transition metal dichalcogenides (2-D TMDs) have been employed to investigate the spatial nonlocality in rough silver films[118] and calculate plasmonic near-field enhancement factors (EFs) in MPoFNs[119]. Specifically, the SERS intensities of both out-of-plane and in-plane lattice vibrations of layered MoS_2 sandwiched in an MPoFN are used to explore the vertical and horizontal electric field enhancements in plasmonic nanocavities: a significant quenching of the vertical local field enhancement,

in comparison to the classical EM prediction, is observed when the layer number of MoS_2 decreases to monolayer[119]. However, the horizontal electric field enhancement calculated from their measured SERS EFs is even larger than that under classical predictions, which leaves a question whether the opposite variation trends of vertical and horizontal field components result from the wrinkles in the MoS_2 layer or the relatively large thickness of monolayer MoS_2 (0.62 nm). Moreover, the MPoFNs with gap distances defined by high-resolution TEM cross-sectional imaging are not correlated with that employed in the dark-field scattering and SERS measurements, and no quantum calculations are carried out to fully understand the far- and near-field properties of the MoS_2-sandwiched MPoFNs.

Actually, the horizontal near-field enhancement in the MPoFNs is of equal importance as many distinct optical phenomena, for example, plasmon−exciton couplings in monolayer TMD-sandwiched MPoFNs are related with the horizontal electric field component as a consequence of the horizontal orientation of bright exciton dipole moments in monolayer TMDs[120, 121]. Additionally, the horizontal electric field components in the MPoFNs also have a great influence on determining the plasmon-induced hot-carrier generation efficiency at relatively large gap distances[122]. Hence, there is a strong interest to study the horizontal near-field enhancement limit of the MPoFNs with a proper methodology where the gap width can be further decreased and TEM characterizations as well as optical spectroscopies can be exactly one-to-one correlated. Besides, a comprehensive comparison between results from experimental measurement and classical/quantum calculations for the same MPoFNs can further sharpen our understanding of the near-field enhancement limits in different plasmonic nanocavities and their related quantum mechanical origins.

In this Chapter, layered graphene was employed as a spacer to separate the metallic NP and the underlying Au TF in MPoFNs (as schematically shown in Fig. 3.1 (a, b)) and SERS spectroscopy of graphene was also used to indirectly explore the quantum mechanical limit of the horizontal near-field component enhancement within the sub-nanometer gap area. Graphene is a 2-D honeycomb lattice of carbon and exhibits two prominent peaks (G and 2D) in Raman spectrum. The measured SERS intensities of these two major Raman vibrational modes of layered graphene correspond respectively to a primary in-plane vibration mode and a second-order overtone of another in-plane vibration[123], are analyzed as a function of graphene layer number as it varies from one to four. Therefore, there is a possibility to study the influence of quantum mechanical effects on in-plane local field enhancements by measuring the SERS EFs of these two in-plane vibrational modes as the gap width reaches the sub-nanometer level. In addition, I conducted correlated TEM imaging and optical spectroscopies exactly on the same MPoFNs. Together with both classical local and quantum nonlocal calculations, it was demonstrated that the SERS EFs of the in-plane vibrational modes of layered graphene are distinctly affected by the spatial nonlocality, enabling further quantitative investigation of the light−graphene interaction in the range from visible to near-infrared frequencies[124].

3.1 Gap Widths Characterization on Graphene-Sandwiched MPoFNs

In my experiment, high-resolution TEM cross-sectional imaging was employed to precisely define the Au NS−Au TF gap distances of these graphene-sandwiched nanocavities. Figure 3.1(c) and (e) illustrate the TEM cross-sectional image of a SLG-sandwiched MPoFN and the corresponding average count profile in a local region (enclosed in the white box of Fig. 3.1(c)) across the gap, respectively. Firstly, the average count profile in Fig. 3.1(e) shows two predominant peaks, as denoted by two vertical red

lines, which correspond to the edges of the graphene layer (see horizontal red lines in Fig. 3.1(c)). Then, the thickness of the SLG can be estimated to be 0.37 nm, which is close to the theoretical value (0.34 nm). Secondly, Figure 3.1(e) also indicates that the prominent count peaks are not very sharp, suggesting the appearance of transition areas between the SLG and the Au NS or the Au TF. Such transition areas originate from air gaps between the layered graphene and the metals (both Au NS and Au TF). Emergence of the metal−graphene air gaps results from several factors such as the surface roughness of Au TF (as shown in Fig. 3.1(c)), the van der Waals force relaxed metal−graphene distances[125, 126], and the ripples of the layered graphene. It should be stressed that these air gaps are important for the plasmonic response of each MPoFN as both the resonance wavelength and near-field properties of the nanocavity are extremely sensitive to the Au NS−Au TF gap distance, especially when the possible quantum effects were considered within such small gap regions. Hence, I define the graphene−NP air gap width from Fig. 3.1(e) as the distance between the top edge of the graphene layer (as denoted by left vertical red line) and the bottom edge of the Au NS (as denoted by the left vertical yellow line). Similarly, the graphene−Au TF air gap width is the distance between the bottom edge of the graphene layer (as denoted by the right vertical red line) and the top edge of the Au TF (as denoted by the right vertical yellow line). Note that the edges of both Au NS and Au TF were chosen at about half position of the transition areas between graphene and metals. Therefore, the total size of the air gap which is measured from the TEM characterization results is the summation of the sizes of these two air gaps. According to this method, the total air gap sizes in the SLG- (Fig. 3.1(c) and (e)), 2LG-, and 4LG- (Fig. 3.1(d) and (f)) sandwiched MPoFNs are estimated as 0.22, 0.19, and 0.25 nm, respectively. Since the best resolution of the TEM is around 0.1 nm, it is assumed the total size of the local air gap is identical for all the MPoFNs, i.e. 0.2 nm. Note that this air gap is only determined within a local area.

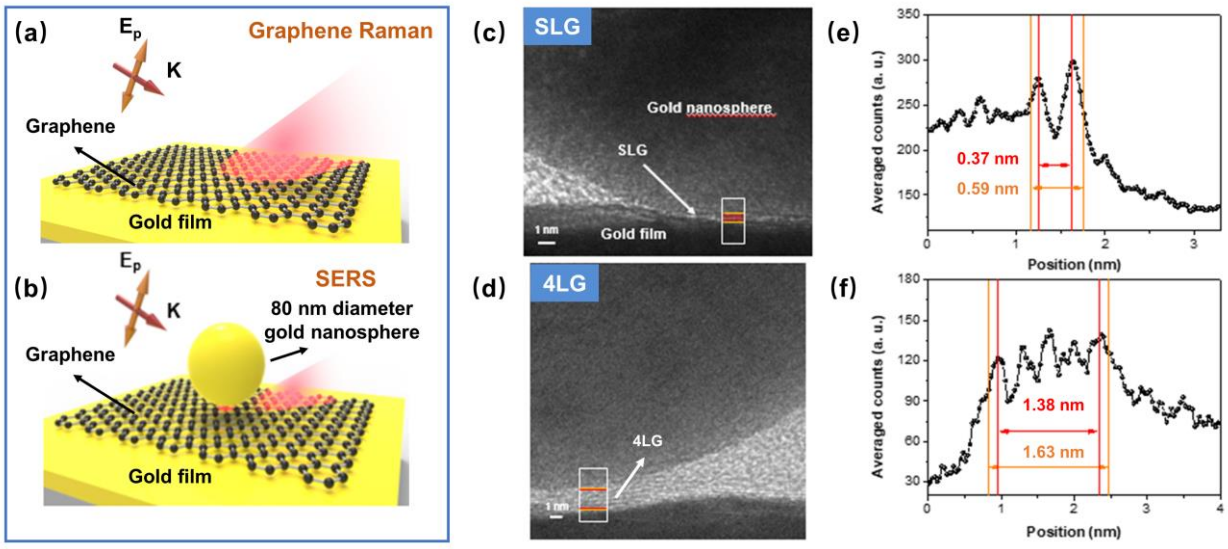

Figure 3.1 (a, b) Schematics of a monolayer graphene (a) and SLG-sandwiched MPoFN (b) deposited on Au TF under an oblique p-polarized incidence. (c, d) High-resolution TEM cross-sectional images of an SLG- (c) and 4LG- (d) sandwiched MPoFN. The white box encloses a local region across the gap, while the red and yellow lines denote the edges of the graphene layer and the metals, respectively. (e, f) Average count profile of SLG- (e) and 4LG- (f) sandwiched MPoFN across the local region enclosed in the white box in (c) and (d) respectively. The vertical red and yellow lines mark the positions of the edges of the graphene layer and the metals, respectively.

3.2 Far- and Near-Field Spectroscopies of Graphene-Sandwiched MPoFNs

To investigate the far-field optical properties of the graphene-sandwiched MPoFNs, I used a standard dark-field optical microscope equipped with an unpolarized light source to measure the single-particle scattering spectra of those plasmonic nanocavities. The light beam is tightly focused on the sample plane via a 100× dry objective (NA = 0.8), which generates, apart from the in-plane field component, a large amount of out-of-plane electric field components. As a consequence, both the transverse and vertical mode of the MPoFNs can be effectively excited. According to the scattering spectra illustrated in Fig. 3.2(a), two major scattering peaks can be observed. The short-wavelength scattering peak occurs in the

range from 530 to 540 nm, which is the horizontal plasmon resonance mode of the MPoFN and therefore insensitive to the change of gap distance. While the long resonance mode originates from the vertical gap mode with a much stronger scattering intensity, which significantly blue-shifts with increasing the graphene layer number (i.e., as the gap width increases) and matches well with previous reports[108, 127-130]. To be more specific, the resonance mode blue-shifts from about 670 nm to 600 nm with the graphene layer number varying from SLG to 4LG.

As discussed above, the air-gap width obtained from the TEM imaging is for a local region much smaller than the effective interaction region between the NP and the Au TF. Besides, the Au TF prepared by thermal evaporation has a RMS surface roughness of around 0.9 nm as measured by AFM mapping (see Fig. 2.1(b)). Based on these two factors, I determined the average air-gap size (d_{air}) in the effective interaction region to be the summation of the local air-gap width (0.2 nm) and an additional thickness of 0.5·RMS, i.e., d_{air} = 0.2 nm + 0.5·0.9 nm = 0.65 nm. Following this approach, the total effective gap width (d) in each MPoFN is expressed as $d_{\mathrm{Gr}} + d_{\mathrm{air}}$, where d_{Gr} = N·0.34 nm is the thickness of N-layer graphene. Consequently, the maximum and minimum effective gap widths in the graphene-coupled MPoFNs are around 2 nm (for the 4LG-coupled nanocavity) and 1 nm (for the SLG-coupled nanocavity), respectively. It is expected that, at such a length scale (1 nm $\leq d \leq$ 2 nm), the nonlocal screening effect greatly influences both the far- and near-field optical responses of the plasmonic nanostructures. To prove this, I calculated the scattering spectra for the four graphene-sandwiched MPoFNs by employing both classical local and quantum nonlocal models implemented in a commercial numerical software, COMSOL Multiphysics. In the simulations, a transverse magnetic (TM) polarized plane wave was incident on the nanostructures at an angle of 53°, and NLHD model was employed to calculate the

nonlocal screening effect (as shown in Section 1.4.2). However, direct solving the coupled equations (Eq. (1.2) and Eq. (1.3)) for a large-scale plasmonic nanostructures in COMSOL such as a MPoFN always occupies enormous memory and is therefore very time-consuming. To overcome this issue efficiently, I used the dielectric-layer model[131, 132], where the nonlocality is interpreted as an inward shift of the metal−dielectric boundary; namely, a thin layer of metal is substituted with a dielectric material with a suitable calculated dielectric function ε_{d}. Then the thickness of dielectric layer Δd can be determined via the following expression:

$$\Delta d = \frac{\varepsilon_{\mathrm{d}}(\varepsilon_{\mathrm{m}}-\varepsilon_{\mathrm{b}})}{\varepsilon_{\mathrm{b}}\varepsilon_{\mathrm{m}}k_{\mathrm{L}}} \tag{3.1}$$

Where ε_{b} is the dielectric constant of the background, and k_{L} is the longitudinal plasmon normal wave vector, which is inversely proportional to the decaying length of the surface charges.

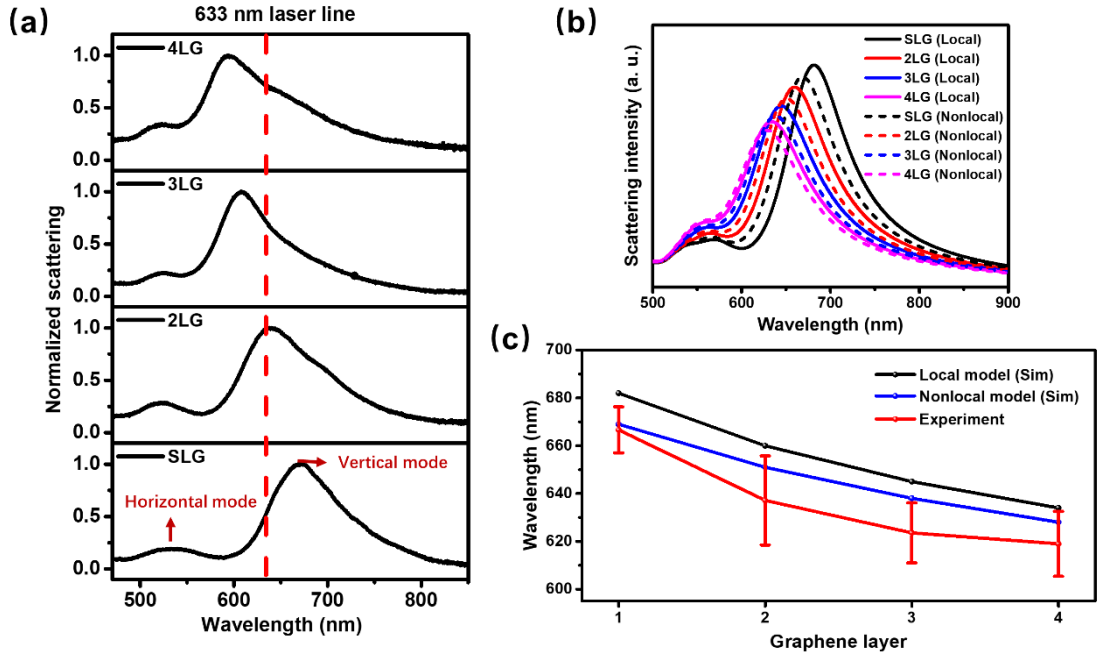

Figure 3.2 (a) Measured scattering spectra of graphene-sandwiched MPoFNs with the graphene layer number varied from one to four. (b) Calculated classical local and nonlocal scattering spectra of the graphene-sandwiched MPoFNs. (c) Calculated

and measured resonance wavelength of the vertical gap mode as a function of graphene layer number. The simulations were carried out under both classical local and quantum nonlocal models.

Figure 3.2(b) demonstrates the simulated local and nonlocal scattering spectra for the four graphene-coupled MPoFNs. One can see that the vertical gap mode for each graphene-coupled MPoFN is clearly blue-shifted through the nonlocal screening effect. This blue-shift can be directly understood as a consequence of an increased effective gap width due to the centroid displacement of the conduction charge density inward towards the metal surface from the geometry boundary in the gap area in which the Au NS and the Au TF have the strongest interaction. Nevertheless, the increased effective gap width has no significant impact on the transverse plasmon resonance mode since this mode is intrinsically insensitive to the gap width as mentioned above. Furthermore, the blue-shift of the gap mode in contrast to the classical local prediction reduces as the total effective gap width increases when more layers of graphene was sandwiched in the MPoFN, which has been both theoretically predicted[133] and experimentally proved[134] in plasmonic NP dimers with similar gap distances.

In Fig. 3.2(c), the measured and simulated plasmon resonance wavelengths were compared for the vertical gap mode. It is as expected that the resonance wavelength calculated by the nonlocal model blue-shifts compared to that by the classical local model for each graphene-sandwiched MPoFN. The error bars demonstrate standard deviations of the measured resonance wavelengths for the four graphene-sandwiched MPoFNs. Explicitly, Figure 3.2(c) indicates that the resonance wavelengths of the vertical gap mode calculated by the nonlocal model agree much better with the measured results than those calculated from the classical local model. The disparity between the measured and nonlocal results

is acceptable because it is impossible to assure that all the parameters used in the calculations are exactly the same as those of the prepared samples. First and foremost, the total gap width of MPoFN used in each calculation inevitably have a certain amount of discrepancy from that for the corresponding real sample, which is due to the fact that surface roughness of Au TF and the local morphologies of Au NSs lead to varied gap distances at different regions. Besides, the sizes of the Au NSs have fluctuation around 40 nm, which is verified by the TEM characterization of different graphene-sandwiched MPoFNs (as shown in Fig. 3.3). Finally, the current modeling of the anisotropic dielectric characters of graphene (see Eq. (A.1) and Eq. (A.2)) may be too ideal to accurately describe the dielectric responses of graphene at visible frequencies. As seen from Eq. (A.1), the in-plane dielectric constant of the layered graphene largely depends on the surface conductivity, which in turn is determined by several inherent physical parameters of graphene as seen from Eq. (A.2), including Fermi energy, Fermi velocity, carrier relaxation lifetime and mobility. Nonetheless, after calculating the scattering spectra of the SLG-sandwiched MPoFN with different carrier mobilities and/or Fermi energy of graphene sheet (see Fig. 3.4), it is found that the scattering properties of the plasmonic nanocavity are insensitive to the in-plane dielectric constant of graphene. While the resonance wavelength of the gap mode clearly red-shifts (as shown in Fig. 3.4) when the out-of-plane dielectric constant of graphene was increased from 1.0 to 2.5. Even so, the nonlocal calculations have revealed the fundamental mechanisms of nonlocal screening in affecting the far-field optical property of the graphene-coupled MPoFNs.

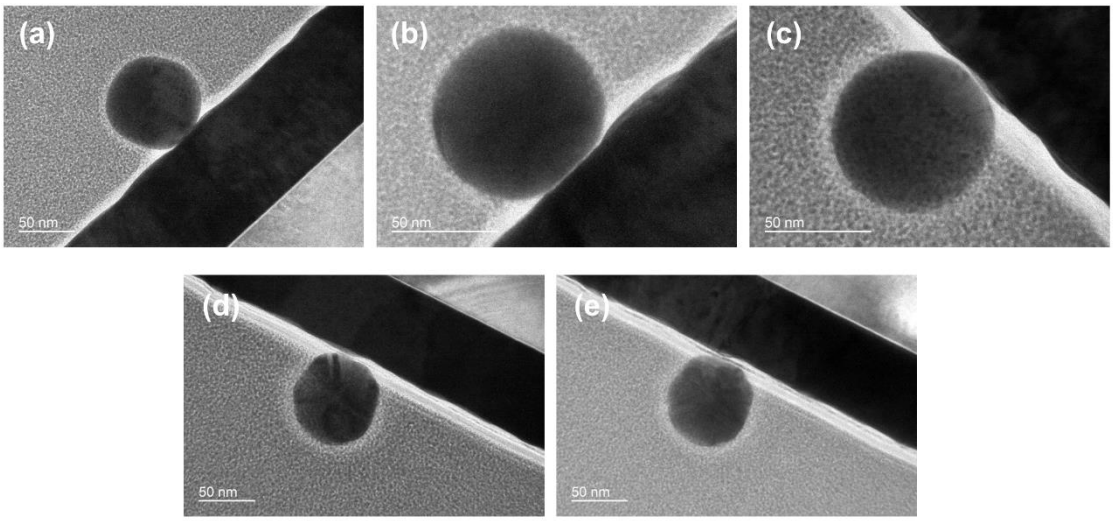

Figure 3.3 High-resolution TEM cross-sectional images of (a, b) 1LG- and (c, d, e) 4LG-, 5LG-, 6LG-coupled MPoFNs.

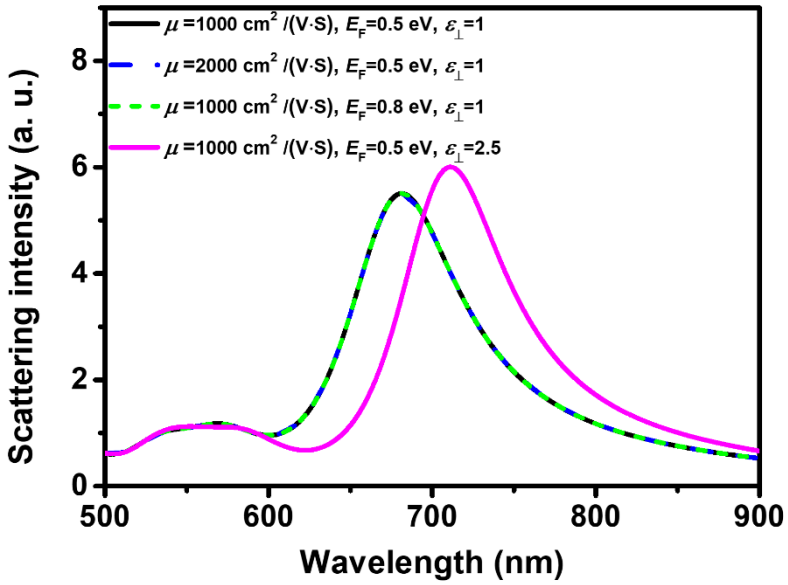

Figure 3.4 Simulated far-field scattering spectra (53° excitation) of an SLG-sandwiched MPoFN with varied carrier mobility (μ), Fermi energy (E_F) and out-of-plane permittivity ($\varepsilon_\perp$) of the graphene by the classical local model.

Except for the prominent influence in the far-field optical properties, the nonlocal screening effect also leads to an ultimate limit to the near-field enhancement and confinement within the small gap area of the MPoFNs. As mentioned above, SERS is a powerful tool that has been recently employed to

investigate the quantum effects on the plasmonic near-field EFs of different plasmonic nanostructures. In graphene-sandwiched MPoFNs, Raman scattering of the graphene layers can be largely enhanced by the strong local near-field intensity induced in the gap area. In the experiment, SERS intensities of both G and 2D bands were measured for the four graphene-sandwiched MPoFNs under 633 nm continuous wave (CW) laser excitation. The incident laser beam with a linear polarization is tightly focused onto the sample plane via a 100× objective lens (NA = 0.9), and the laser power is set as 0.3 mW to avoid probable photodamage to the plasmonic nanocavities or unwanted nonlinear optical effects within the local gap area. Note that here the Raman spectra of graphene were obtained under 3 mW power of the same laser and then scaled down by 10 times to make a comparison with the SERS spectra of the graphene-coupled MPoFNs. The reason for this treatment is that the Raman emissions of layered graphene under 0.3 mW laser irradiation are too weak for the Raman measurement. This treatment has been proved to be reasonable by observing a linear relationship between the incident laser power and Raman intensity of a pristine graphene (as illustrated in Fig. A1), although it causes the disparity of the noise between the SERS and Raman spectra.

Figures 3.5(a)−(d) demonstrate the SERS spectra (black line) of four graphene-sandwiched MPoFNs and the corresponding Raman spectra (red line) of the same graphene layers on the bare Au TF. Evidently, both the G and 2D band Raman peaks are largely enhanced due to the existence of the MPoFNs. Besides, structure-correlated dark-field scattering imaging and spectroscopy are also conducted on the same plasmonic nanocavities before and after the SERS measurements. The dark-field images as well as the scattering spectra collected before and after the SERS measurements are identical to each other,

indicating no perceivable photodamage caused by the CW laser irradiation (as shown in Fig. 3.6). Such control experiments ensure the precision and consistence of the measured results.

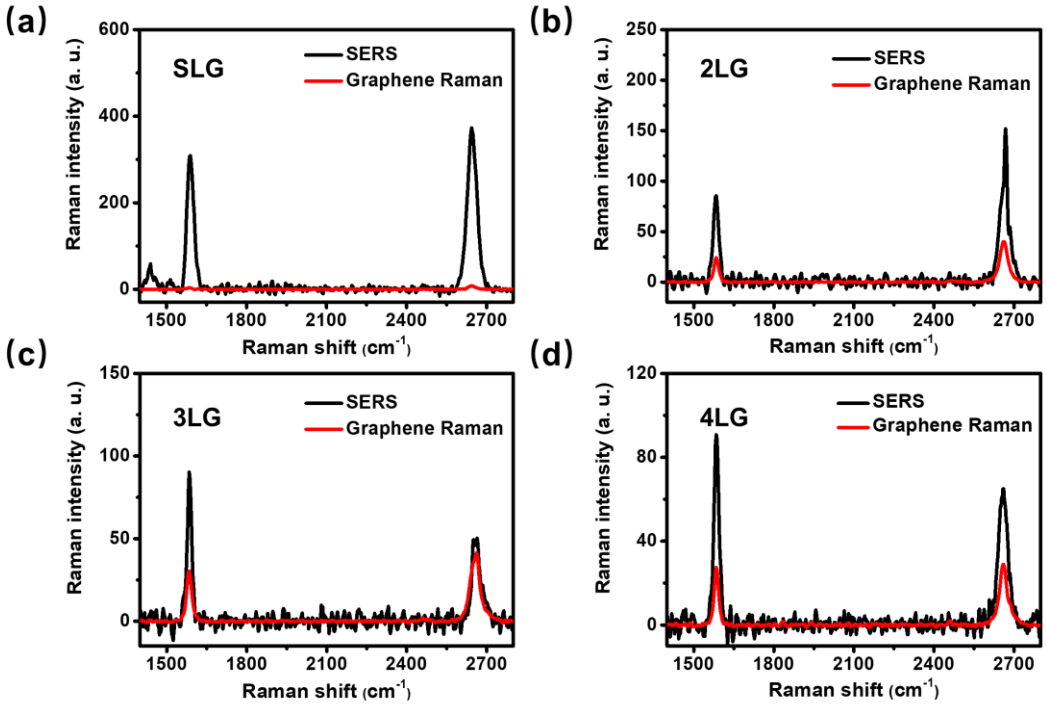

Figure 3.5 Raman spectra taken on (black) and off (red) each of the four MPoFNs with graphene layer number ranging from SLG to 4LG. The integration time of signal for both Raman and SERS spectra was 10 s.

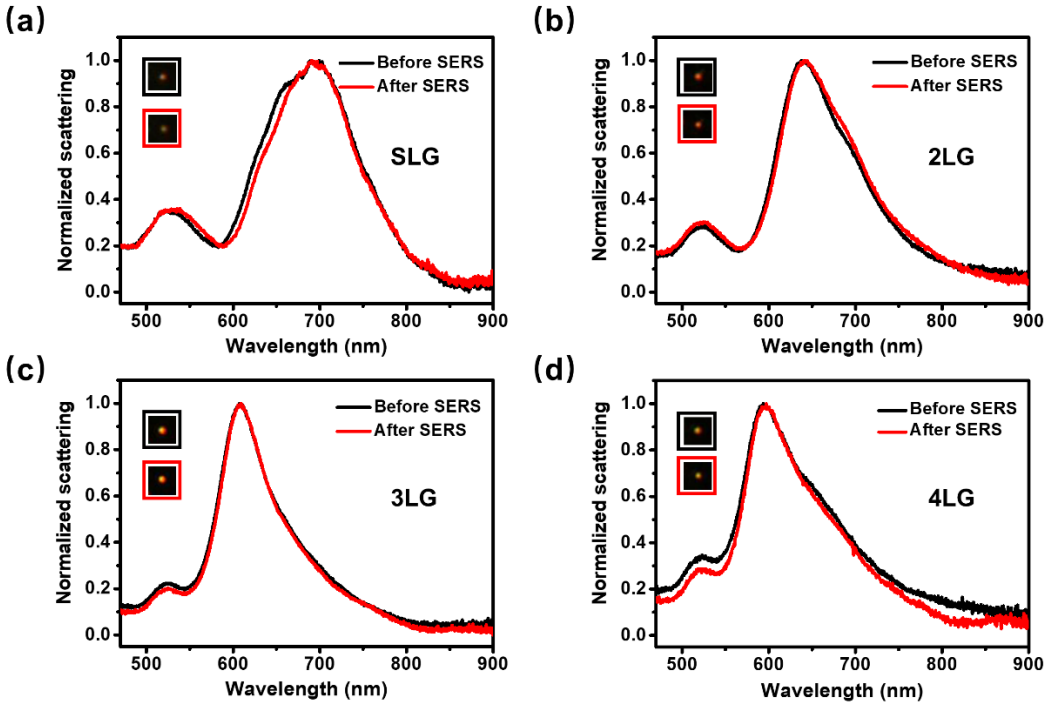

Figure 3.6 Scattering spectra and dark-field images (see insets) of the same nanostructure as in Fig. 3.5 taken before and after SERS measurements.

Moreover, I theoretically calculate the graphene layer dependence of SERS EFs in the four graphene-sandwiched MPoFNs. Here, the SERS EF is defined as:

$$\overline{EF_{\parallel}} = \frac{I_{\mathrm{NP}}}{I_{\mathrm{Gr}}} \cdot \frac{A_{\mathrm{eff}}}{A_{\mathrm{SERS}}} \tag{3.2}$$

where I_{NP} is the SERS signal collected from the confocal region including a MPoFN. I_{Gr} is the Raman signal collected from the graphene layer that is close to the MPoFN (to make sure the same graphene quality and thereby the same inherent Raman response). A_{eff} is the valid laser excitation region with a spot size of around 340 nm in radius for the 633 nm laser, which corresponds to a 0.36 μm^2 spot region, and A_{SERS} is the valid local field region of the plasmonic nanocavity, which is defined by:

$$A_{\mathrm{SERS}} = \pi R_{\parallel}^2 \tag{3.3}$$

where $R_{\parallel}$ denotes the effective radius of the in-plane near-field "hot spot" in each graphene-sandwiched MPoFN and is attained from the calculated electric field distribution profile of each nanostructure. In

my simulation, the SERS EF for each graphene-coupled MPoFN can be approximately defined by the surface-averaged in-plane near-field EF with the following equation:

$$\overline{EF_{\parallel}} = \frac{1}{\pi R_{\parallel}^2} \int_A \left| \frac{\mathbf{E}_{\parallel}(\lambda_{\mathrm{in}})}{\mathbf{E}_{\parallel 0}(\lambda_{\mathrm{in}})} \right|^2 \cdot \left| \frac{\mathbf{E}_{\parallel}(\lambda_{\mathrm{out}})}{\mathbf{E}_{\parallel 0}(\lambda_{\mathrm{out}})} \right|^2 da \tag{3.4}$$

where $\left|\mathbf{E}_{\parallel}(\lambda_{\mathrm{in}}, \lambda_{\mathrm{out}})\right| = \sqrt{|E_{\mathrm{x}}|^2 + \left|E_{\mathrm{y}}\right|^2}$ is the amplitude of the overall in-plane near field at the incident (outgoing) wavelength. $\left|\mathbf{E}_{\parallel 0}(\lambda_{\mathrm{in}}, \lambda_{\mathrm{out}})\right| = \sqrt{|E_{\mathrm{x0}}|^2 + \left|E_{\mathrm{y0}}\right|^2}$ denote the amplitude of the corresponding background in-plane electric field. In the calculations, the near fields at the outgoing wavelengths were acquired by setting the excitation wavelengths the same as the emission wavelengths of the corresponding Raman scattering signals, that is, 704 nm and 760 nm for the G peak and the 2D peak, respectively. To determine $R_{\parallel}$, I have calculated the fraction of in-plane SERS EF according to the following equation:

$$f_{\parallel}(\rho) = \frac{\int_0^{\pi\rho^2} \left| \frac{\mathbf{E}_{\parallel}(\lambda_{\mathrm{in}}) - \mathbf{E}_{\parallel 0}(\lambda_{\mathrm{in}})}{\mathbf{E}_{\parallel 0}(\lambda_{\mathrm{in}})} \right|^2 \cdot \left| \frac{\mathbf{E}_{\parallel}(\lambda_{\mathrm{out}}) - \mathbf{E}_{\parallel 0}(\lambda_{\mathrm{out}})}{\mathbf{E}_{\parallel 0}(\lambda_{\mathrm{out}})} \right|^2 da}{\int_0^{\infty} \left| \frac{\mathbf{E}_{\parallel}(\lambda_{\mathrm{in}}) - \mathbf{E}_{\parallel 0}(\lambda_{\mathrm{in}})}{\mathbf{E}_{\parallel 0}(\lambda_{\mathrm{in}})} \right|^2 \cdot \left| \frac{\mathbf{E}_{\parallel}(\lambda_{\mathrm{out}}) - \mathbf{E}_{\parallel 0}(\lambda_{\mathrm{out}})}{\mathbf{E}_{\parallel 0}(\lambda_{\mathrm{out}})} \right|^2 da} \tag{3.5}$$

Note that in the calculations I employed 350 nm as an actual integral radius in the denominator of Eq. (3.5). Figure 3.7 demonstrates the fraction of in-plane SERS EF as a function of integral radius ρ at the middle plane of the SLG (a, c) and 4LG (b, d) calculated via the nonlocal model. It is seen that the fraction saturates quickly with enlarging integral radius. Here I determine $R_{\parallel}$ when the fraction of in-plane SERS EF reaches 99%, meaning that the corresponding gap area would contribute the total in-plane near-field enhancement. The insets in Fig. 3.7(a) and (b) ((c) and (d)) illustrate the effective in-plane electric field distribution profiles for the SLG- and 4LG-coupled MPoFNs in correspondence to the G peak (2D peak). As shown by the profiles, the electric near fields within the SLG-coupled MPoFN gap area are more tightly restricted than that in the gap areas including multilayer graphene sheets, resulting in smaller $R_{\parallel}$ when the gap width reduces. The fractions of in-plane SERS EF as a function

of integral radius for 2LG- and 3LG-sandwiched MPoFNs and the corresponding effective in-plane electric field distribution are illustrated in Fig. 3.8. The obtained values of $R_{\parallel}$ are then employed to determine the surface-averaged in-plane near-field EF of each graphene-coupled MPoFN given by Eq. (3.4) under both classical local and nonlocal regimes.

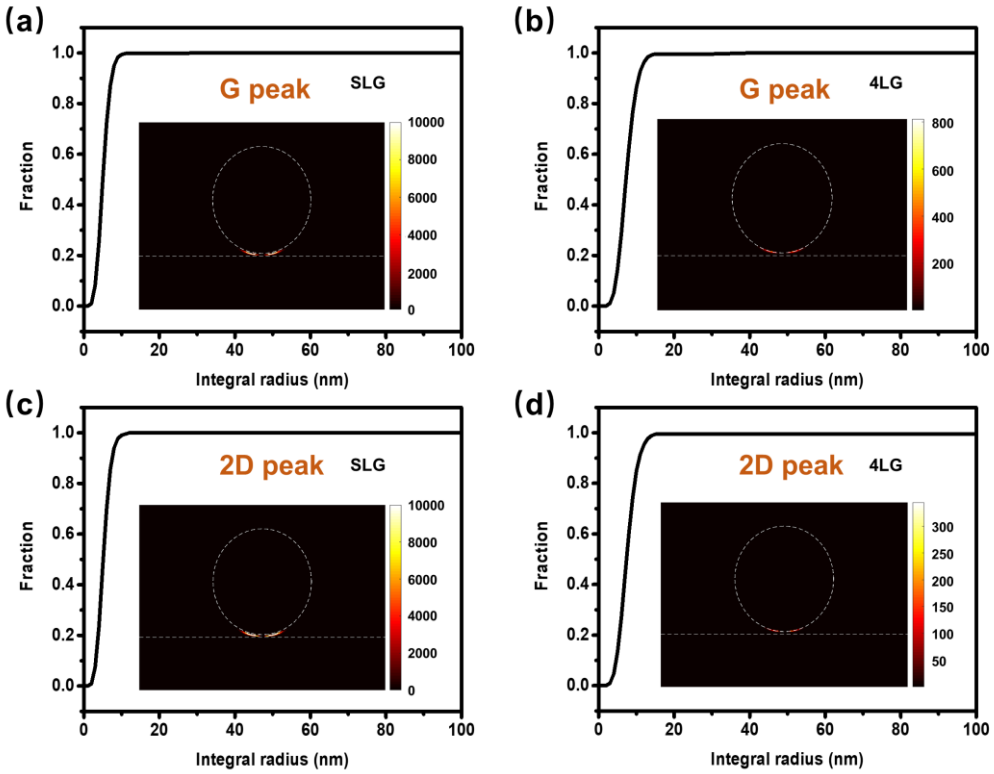

Figure 3.7 Fraction of in-plane SERS EF as a function of integral radius in the gap area of (a, c) SLG- and (b, d) 4LG-sandwiched MPoFNs by the quantum nonlocal model. The insets in (a) and (b) demonstrate the effective in-plane electric field distribution (under 633 nm excitation and emission at 704 nm, corresponding to the G peak) for the SLG- and 4LG-sandwiched MPoFN, respectively. The insets in (c) and (d) demonstrate similar results to those in (a) and (b) (under 633 nm excitation and emission at 760 nm, corresponding to the 2D peak) for the same MPoFNs. Numerically, a p-polarized plane wave excites the graphene-sandwiched MPoFNs at an incident angle of 64°. The white dashed lines in the insets denote the boundaries of the Au NSs and the underlying Au TFs.

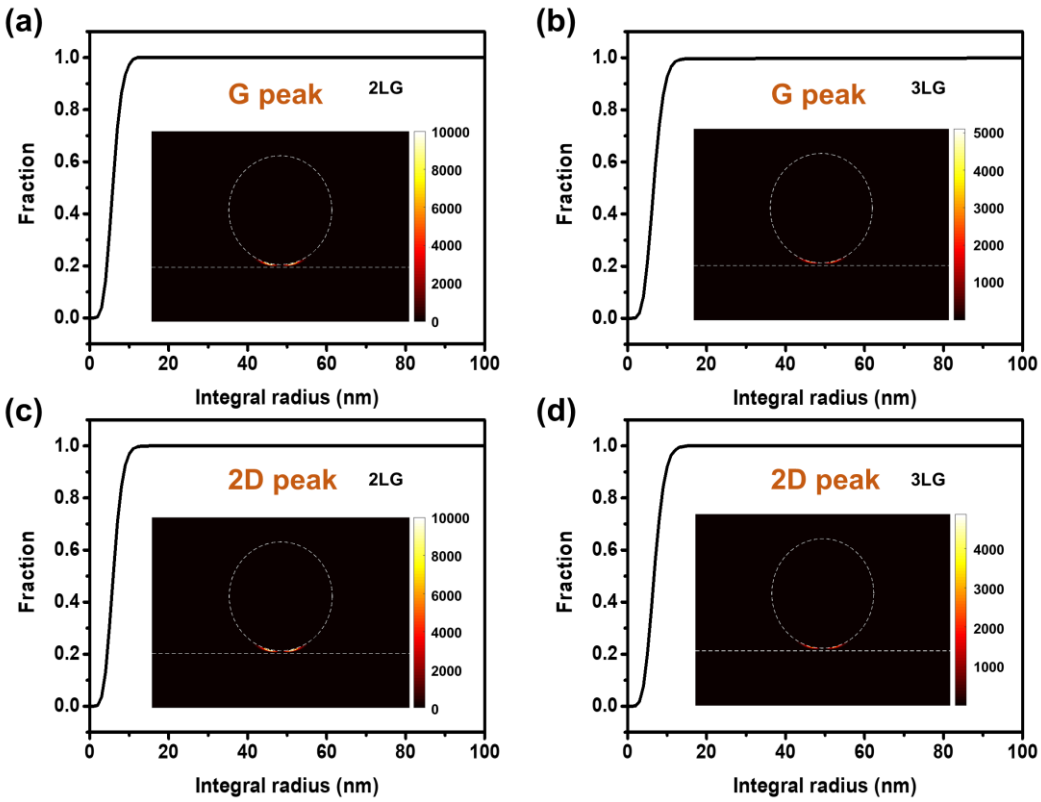

Figure 3.8 Fraction of in-plane SERS EF as a function of integral radius in the gap region of (a, c) 2LG- and (b, d) 3LG-sandwiched MPoFNs by the quantum nonlocal model. The insets in (a) and (b) demonstrate the effective in-plane electric field distribution (under 633 nm excitation and emission at 704 nm, corresponding to the G peak) for the 2LG- and 3LG-sandwiched MPoFN, respectively. The insets in (c) and (d) demonstrate similar results to those in (a) and (b) (under 633 nm excitation and emission at 760 nm, corresponding to the 2D peak) for the same MPoFNs. Numerically, a p-polarized plane wave excites the graphene-sandwiched MPoFNs at an incident angle of 64°. The white dashed lines in the insets denote the boundaries of the Au NSs and the underlying Au TFs.

3.3 Observation of Horizontal Near-Field Enhancement Limit in Graphene-Sandwiched MPoFNs

By calculating the corresponding $R_{\parallel}$ values for the four graphene-sandwiched MPoFNs, both experimental and simulated SERS EFs can be determined by Eq. (3.2) and Eq. (3.4), with results shown in Fig. 3.9(a) and (b). Here the experimental results represent statistics of SERS EFs measured over dozens of similar nanostructures for each graphene-sandwiched MPoFN (see Fig. A2). The error bars

were attained from the standard error in Gauss fitting of the statistic EFs that can be seen in the zoomed-in views in the insets of Fig. 3.9(a) and (b). Besides, the measured SERS EFs illustrated in Fig. 3.9(a) and (b) are scaled up 20 times to better view the comparison to the simulated results. This is due to the fact that the measured SERS EFs are approximately an order of magnitude smaller than the calculated values because of the relatively low collection efficiencies during the SERS test. Clearly, Figure 3.9(a) and (b) demonstrate that the variation of the measured SERS EFs for both the G and 2D bands as a function of the graphene layer number shows a similar variation trend to that of the nonlocal calculations. In sharp contrast, when the layer number of graphene sheet reduces, the calculated local SERS EFs for both the G and 2D Raman bands increase much more rapid than the measured results. In particular, the calculated local SERS EFs for both Raman bands in the SLG-sandwiched MPoFN exhibit a sharp rise, which apparently deviates from the measured trends. Hence, it can be summarized that the in-plane near-field EF of the graphene-coupled MPoFN is evidently attenuated by the spatial nonlocality effect. In the meanwhile, it is worth noting that the near-field enhancement has not reached saturation yet even in the SLG-sandwiched MPoFN due to its relatively large gap distance. Further improvement in the preparation of such graphene-sandwiched MPoFNs, for instance by using ultrasmooth Au TF, may be able to further reduce the gap distance such that more prominent quantum effects including surface charge spill-out and electron tunneling could be observed in both far-field scattering and near-field SERS measurements.

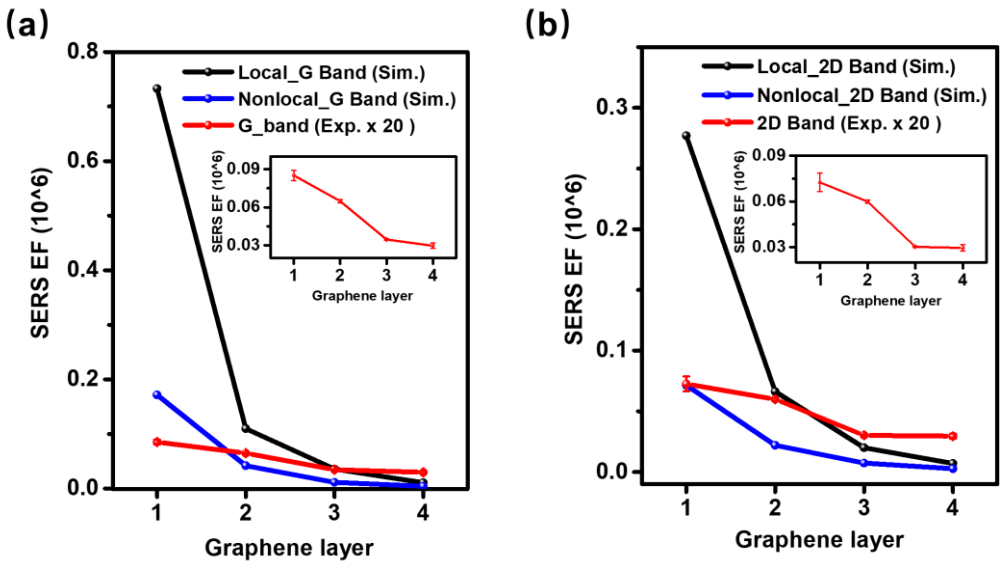

Figure 3.9 Simulated and measured in-plane SERS EFs (a, b) as a function of graphene layer number. The SERS EFs for both G and 2D bands of graphene sheets were calculated with Eq. (3.2) and Eq. (3.4). The measured SERS EFs are scaled up 20 times, and the error bars can be seen in the zoomed-in views in the insets.

3.4 Conclusion

To sum up, I have combined comprehensive theoretical calculations as well as far- and near-field optical characterizations to explore the near-field enhancement limit in graphene-sandwiched MPoFNs. In contrast to the classical local and quantum nonlocal simulation results, the measured SERS EFs clearly disclose that the in-plane near-field enhancement is largely mitigated by the spatial nonlocality effect as the gap distance reaches to the sub-nanometer level. Distinctively different from many previous studies, I first performed rigorously correlated morphological characterizations and optical spectroscopies exactly on the same graphene-coupled MPoFNs so as to avoid ambiguities caused by possible geometric difference from structure to structure. In accordance with the predictions using quantum nonlocal model, both near-field SERS EF and far-field plasmon resonance shift exhibit a quantum limit to the gap distance of the MPoFNs. This work not only helps us deepen the understanding of the plasmonic

response of nanocavities with sub-nanometer gaps but also is a step forward in exploring modulation of plasmonic resonances in graphene-based nanophotonic devices.

Chapter 4 Passive and Active Modulation of Light Scattering and Raman Enhancement in Molecule-Sandwiched Plasmonic Metal Particle-on-Film Nanocavities (MPoFNs): Molecular Charge Transport

Plasmonic nanocavity with small gap distances can achieve strong light confinement and enhancement[135]. Light being trapped into the gap region leads to the quantum mechanical effects when the dimension between two metallic nanostructures further decreases. Specifically, plasmonic nanocavity that consists of single metallic NP separated from metal film by a nanometer-thick spacer (either a self-assembled molecular monolayer or a dielectric oxide layer) has attracted lots of attention as this system provides a versatile platform for plasmon resonance tuning and hybridization[29, 42, 136-139], enhanced Raman scattering[140-142], nonlinear plasmonics[143], quantum plasmonics[117] and so forth.

In this Chapter, I used MPoFNs embedded with two types of organic molecules and thoroughly investigated the quantum charge transfer process under ambient conditions. Particularly, charge transfer effect on the hybridized plasmon modes was observed and their physical origins were also disclosed via polarization-dependent dark-field scattering spectra. These results could provide effective guidance for investigation of quantum size effects on plasmon resonance modes induced by large metallic NPs

coupled to the metal film underneath[144]. Next, I investigated active modulation of plasmon resonance in MPoFNs embedded with photoactive molecules.

4.1 Molecular Conductance Induced Plasmon Resonance Shift and Its Influence on Near-Field Enhancement

Charge transfer effect through molecular junctions has been thoroughly explored in plasmonic particle-on-film nanocavities[57, 62, 145-147]. Applying dark-field scattering spectroscopy, a clear blue-shift of the coupled plasmon mode in a particle-on-film nanocavity due to the charge transport between NP and the underlying metal film has been verified[148]. In another similar system, higher order CTP modes and quenching of plasmonic near-field enhancement induced by the charge transport across the molecular junction formed by Au nanoplate-Au NS heterodimers were also reported[84].

According to Mie theory, the plasmon modes of Au NSs induced in the range from visible to near-infrared frequencies depend on their dimensions. The lowest order plasmon mode that originates from electric dipoles (EDs) will exist in all Au NSs with diameters varying from 20 nm to over 400 nm[144]. When the diameter of individual Au NS increases, higher order plasmon modes can be observed in its scattering spectrum. Moreover, if large NPs are placed onto the metal film, higher order plasmon modes are induced in the nanocavities, which differs from regular dipole mode both in peak position and linewidth[149]. In addition, placing active or passive materials including 2-D materials and molecules in this narrow gap area would cause the variation of gap distance and refractive index and therefore change both the far- and near-field optical properties in MPoFNs. Thereby, these higher order modes together

with other hybridized plasmon modes not only influence the far-field scattering spectra but also substantially affect the near-field response in the MPoFNs sandwiched by different materials such as molecules[43].

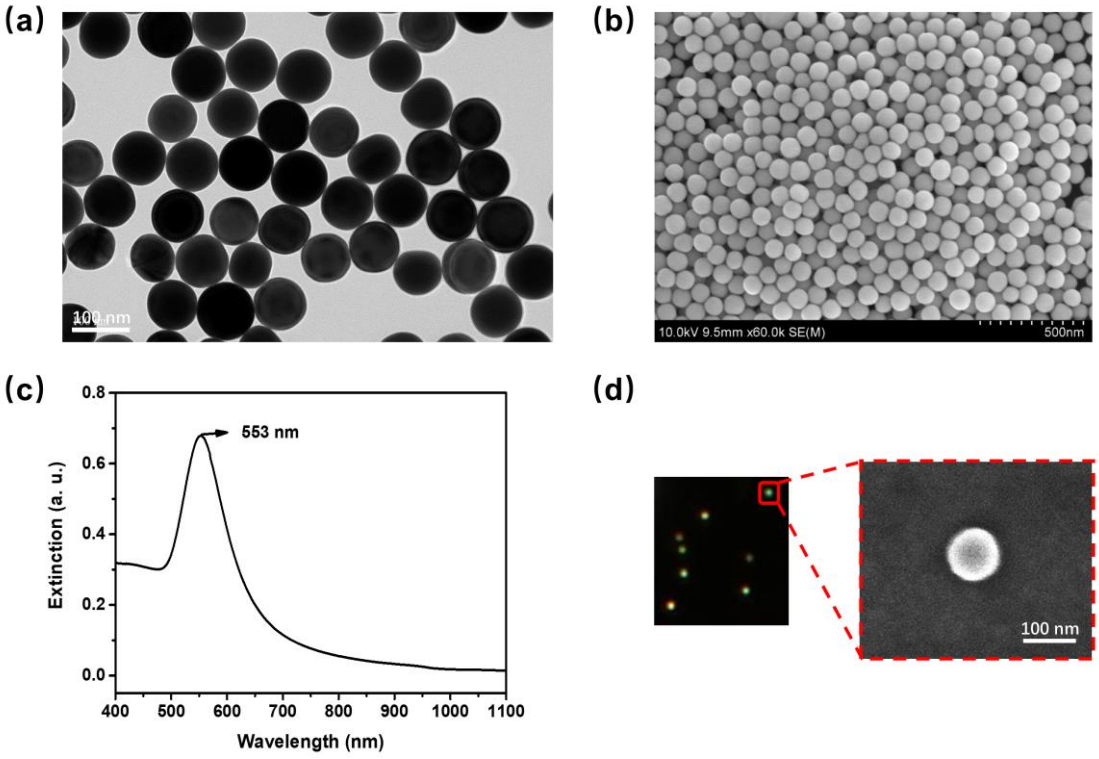

Figure 4.1 High-resolution TEM (a) and SEM (b) images of the Au NSs. (c) Extinction spectrum of the Au NSs solution. (d) Dark-field scattering image of the individual BPDT-sandwiched MPoFNs and SEM image of a BPDT-sandwiched MPoFN (marked by the red square).

Motivated by this insight, I fabricated MPoFNs containing relatively large Au NSs with an average diameter of 88.6±4.8 nm (as shown in Fig. 4.1(a) and (b)), and the extinction spectrum of Au NSs in aqueous solution exhibits a plasmon resonance wavelength of 553 nm (Fig. 4.1(c)). The synthesized Au NSs were firstly decorated by SAM of both conductive (BPDT) and insulating (B4T) molecules (as shown in Section 2.3) then deposited onto the ultrasmooth Au TF obtained by template stripping method

to form molecular nanojunctions within the gap region (see Fig. 4.1(d)). Note that BPDT and B4T have the similar molecular length (~1.3 nm) and refractive index[148]. For dithiol molecules (BPDT) which connect the Au NS and the underlying Au TF through forming Au-S covalent bond, electrons could transfer across molecular nanojunctions. Yet, charge transport rarely happens in nanojunctions formed by monothiol molecules (B4T) because of the difficulty in creating conductive links. In the dark-field scattering spectra of the as-prepared molecule-sandwiched MPoFNs (shown in Fig. 4.2(a)), transverse modes of both BPDT- and B4T-sandwiched MPoFNs appear in the wavelength range from 500 to 600 nm. More importantly, vertically and horizontally mixed mode as well as dipolar plasmon mode were also observed[150], which is determined by the corresponding surface charge distributions. A clear blue-shift of these two modes was observed in BPDT-sandwiched MPoFNs compared to B4T-sandwiched MPoFNs, which can be analyzed by the circuit model (Section 1.3). Specifically, in the above Au NPs-BPDT/B4T-AuTF nanocavities, one can consider the nanojunction as a capacitor shorted by each molecule with a conductance G_{i}. Then the resonance wavelength of the molecule-sandwiched MPoFNs at G is derived based on R-C circuit model[148]. The expression is depicted below:

$$\lambda_{\mathrm{MPoFN}}(G) = \frac{\lambda_0}{1+\frac{k}{\sqrt{1+(\omega\tau_{\mathrm{RC}})^2}}} \tag{4.1}$$

where λ_0 is the resonance wavelength when $G = 0$, k is a constant, ω is plasmon frequency, $\tau_{\mathrm{RC}} = RC$ is R-C time constant. Using the plate capacitor model, τ_{RC} can be further expressed as:

$$\tau_{\mathrm{RC}} = \frac{n_{\mathrm{g}}^2 \varepsilon_0 A_{\mathrm{i}}}{G_{\mathrm{i}} d} \tag{4.2}$$

where n_{g} is the refractive index within gap region, A_{i} is the area of each molecule, d is gap distance.

As indicated by above relation between coupled plasmon resonance and conductance G (Eq. (4.1)), molecule with relatively large conductance would decrease the R-C time constant, which eventually results in a blue-shift of the resonance frequency. In addition to far-field measurement, I also conducted SERS characterization on individual molecule-sandwiched MPoFNs to investigate the effect of charge transfer within molecular nanojunctions on near-field enhancement. As illustrated in Fig. 4.2(b), the three main Raman peak intensities are larger in insulating B4T-sandwiched MPoFNs than that in conductive BPDT-sandwiched MPoFNs, indicating the quenching of near-field enhancement.

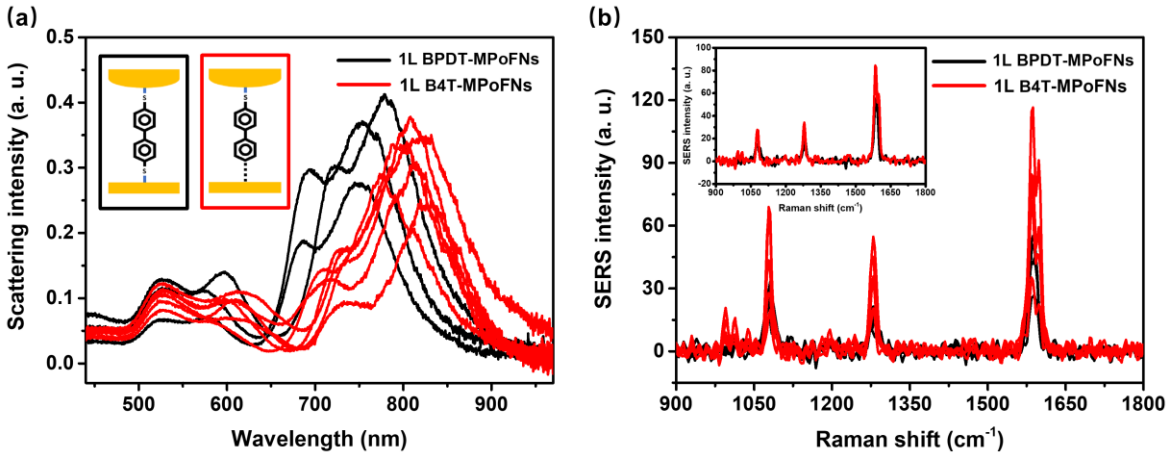

Figure 4.2 (a) Measured single-particle dark-field scattering spectra of the MPoFNs spaced by BPDT (black) and B4T (red) molecules. Insets show the plasmonic nanojunctions formed by these two molecules. (b) SERS spectra of the corresponding structures with BPDT and B4T molecules. The representative SERS spectra of two individual MPoFNs with BPDT and B4T molecules in the gap area are illustrated in the inset. Laser wavelength used in SERS measurement is 633 nm.

To study charge transport through the molecular tunnel nanojunctions quantitatively, I measured dark-field scattering and corresponding SERS spectra of more than a dozen of BPDT/B4T-sandwiched MPoFNs. As illustrated in Table 4.1, the blue-shift of plasmon resonances, together with reduction of SERS intensities in conductive molecule (BPDT) sandwiched nanocavities were also observed

compared with that in insulating counterparts (B4T), further confirming the above conclusions on both far- and near-field measurements. Note that instead of Raman scattering peak intensity, integral intensity of the Raman peaks was employed to better demonstrate the electron transport on local near-field enhancement.

	Plasmon resonance wavelength (nm)		SERS intensity (a. u.)		
	Mode Ⅰ	Mode Ⅱ	Raman peak Ⅰ	Raman peak Ⅱ	Raman peak Ⅲ
1L BPDT-MPoFNs	698 ± 14	762 ± 11	600 ± 266	442 ± 210	1014 ± 494
1L B4T-MPoFNs	723 ± 17	799 ± 14	610 ± 229	572 ± 240	1725 ± 788

Table 4.1 Statistics of the measured resonance wavelength of the vertically and horizontally mixed mode as well as vertically dipolar mode (defined as mode Ⅰ and Ⅱ, respectively) and the integral SERS intensity of the three main Raman scattering peaks in 1L BPDT-MPoFNs (around 1081 cm^{-1} for peak Ⅰ; 1280 cm^{-1} for peak Ⅱ; 1587 cm^{-1} for peak Ⅲ) and 1L B4T-MPoFNs (around 1078 cm^{-1} for peak Ⅰ; 1280 cm^{-1} for peak Ⅱ; peak Ⅲ is split into two peaks at about 1587 cm^{-1} and 1598 cm^{-1}).

4.2 Spectral Decomposition of Plasmonic Modes in Molecule-Sandwiched MPoFNs

To further unravel the physical origins of the plasmon modes observed in scattering spectra. I measured the polarization-dependent dark-field spectra of the BPDT- and B4T-sandwiched MPoFNs as depicted in Fig. 4.3(a) and (b), respectively. Using a homebuilt dark-field microscope, an oblique white light was focused on the sample at an incident angle of 75 degrees (shown in inset of Fig. 4.3(a)). In Fig. 4.3(a), scattering peak at around 775 nm gradually disappears when the polarization changes from p to s, indicating this plasmon mode only responds to vertical polarization. This result verifies my prediction

in the previous section. Therefore, this mode can be referred as vertically dipolar plasmon mode. Meanwhile, the peak at around 700 nm is relatively weak under s-polarized illumination, which indicates that this plasmon mode is a mixture of both vertical and horizontal mode. Besides, the resonance at about 600 nm exhibits same trends as that at around 775 nm, suggesting that it is a higher order vertical plasmon mode. The mode evolution of B4T-sandwiched MPoFNs also shares the similar trend as that of BPDT-sandwiched MPoFNs but is different in the peak positions and relative intensities. Therefore, the plasmon modes of BPDT/B4T-sandwiched MPoFNs can be completely decomposed in the far-field regime and well explained from a perspective of the mode hybridization.

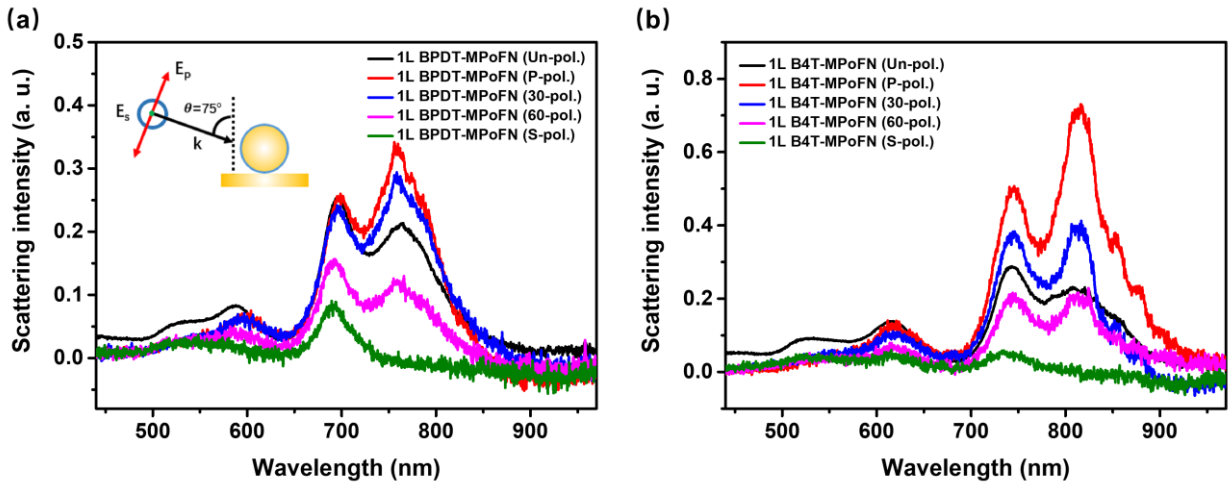

Figure 4.3 Measured dark-field scattering spectra of MPoFNs separated by 1L BPDT (a) and 1L B4T (b) thiol molecules under oblique excitation of incident white light with different polarizations. Excitation configuration is schematically shown in the inset.

4.3 Reversible Plasmon Resonance Tuning in Photoswitchable Molecule-Sandwiched MPoFNs

In above-mentioned nanostructures, various kinds of materials such as graphene and thiol molecules were used to alter the plasmon resonance. However, these demonstrations were all achieved in a passive manner. Therefore, it is strongly desirable to realize active control of plasmon resonance in a reversible way and at ultrafast timescales[151-154], which is of essential importance for optical information processing and designing novel on-chip devices. Recently, host-guest molecular configuration has been proved to be a well candidate in studying strong coupling in plasmonic nanocavities[155]. In particular, photochromic behavior of the diarylethene molecules included in cyclodextrins becomes attractive due to the high cyclization quantum yield of such host-guest molecular system[156].

Here I studied active tuning of linear plasmon resonance in photoswitchable molecule-sandwiched MPoFNs. The MPoFNs were prepared by depositing individual Au NSs (80 nm in diameter) onto the Au TF functionalized with a nanometer-thick SAM of photoactive host-guest molecules in which the thiol-β-cyclodextrin has thiol group that can bind to the gold surface by forming Au-S bond. Figure 4.4(a) and 4.4(b) show the powder Raman characterization on both diarylethene molecule and thiol-β-cyclodextrin in which various peaks were observed. Specifically, in Fig. 4.4(b), Raman peak at 2571 cm^{-1} occurs as the evidence of thiol groups bonded in β-cyclodextrin[157]. From Fig. 4.4(c) one can observe appearance of new bands at about 358 and 523 nm in the absorption spectra of diarylethene molecule solution by gradually increasing UV exposures, which has been identified as the closed ring form of diarylethene molecules, i.e. the increase of the π-conjugation length of the molecule[158, 159]. After visible light illumination, the absorption spectrum returned to the initial state, indicating the reversibility of

switching process. This kind of photochromic reaction process is based on reversible hexatriene-cyclohexadiene type photocyclization[160]. Typically, the opened ring form of diarylethene has two different conformations, parallel and antiparallel. The photocyclization can only proceed from the antiparallel conformation while the parallel conformation is photochemically inactive[156, 161]. Physical trapping of a diarylethene molecule inside a thio-β-cyclodextrin cavity can largely increase the ratio of antiparallel to parallel conformations, thus benefiting the molecular photochromism, and will expand the application in active control of optical emissions in molecular-sandwiched nanocavities.

Next, I investigated the plasmon resonance tuning on the photoswitchable molecule-sandwiched MPoFNs. Firstly, each MPoFN was identified using a CCD camera. Once identified, dark-field spectra were taken on the MPoFNs. After that, the sample was exposed under 365 nm UV light for 5 minutes to stimulate the photochromic reaction process of host-guest composites and scattering spectra were measured to compare with the initial dark-field spectra. Finally, the UV light was turned off and another scattering spectrum was collected after 5 minutes of white light exposure to complete the whole switching cycle. As depicted in Fig. 4.4(d), the gap mode of single MPoFN initially peaks at about 726 nm. After UV illumination, the gap mode red-shifts by 6 nm in contrast to the initial peak position, then the resonance peak of the designated MPoFN shifts back to the initial position after white light irradiation, which is caused by the reversible change of the effective dielectric environment of the junction.

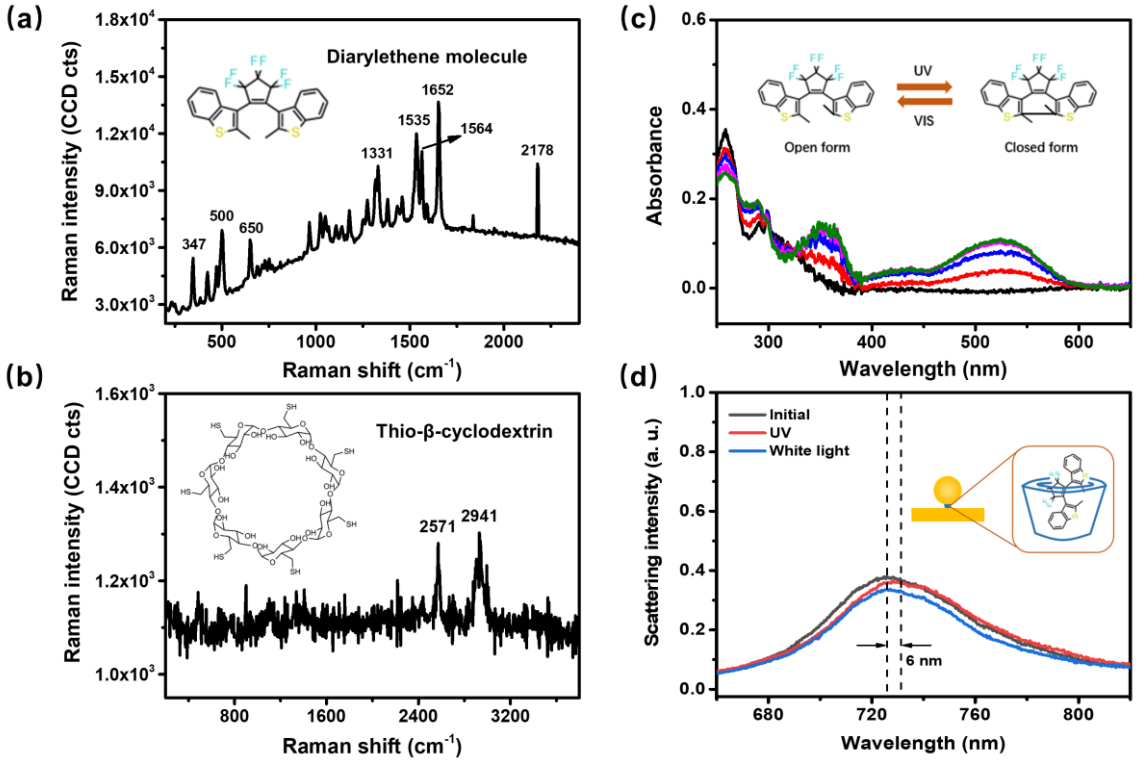

Figure 4.4 (a, b) Powder Raman spectra taken on diarylethene molecule (a) and thio-β-cyclodextrin (b). Raman spectra were measured under the 532 nm CW laser irradiation. Insets show the chemical configurations for both molecules (c) UV-Vis spectral change of the diarylethene molecule solution (6×10^{-5} M) upon irradiation with 365 nm light every 3 minutes (0-12 min). Inset illustrates the open and closed forms of the diarylethene molecule. (d) Dark-field scattering spectra of individual diarylethene-molecule-sandwiched MPoFN taken during one UV-white light exposure cycle. The host-guest molecule-sandwiched MPoFN was schematically shown in the inset.

4.4 Conclusion

To sum up, I have experimentally studied charge transport in two types of molecule-sandwiched MPoFNs. When the junction is connected by conductive molecule (BPDT), a clear blue-shift of both vertically and horizontally mixed mode as well as vertically dipolar plasmon mode in the dark-field spectra compared to insulating counterpart (B4T) indicates the direct charge transport across the molecular nanojunction. The physical origins for dominant plasmon resonance modes were also revealed by polarization-dependent dark-field spectroscopy. Besides, the reduction in the measured SERS spectra

of conductive molecule-sandwiched MPoFNs provides the evidence of plasmonic quenching of near-field enhancement which results from charge transfer in the molecular tunnel junctions. Furthermore, I demonstrated reversible tuning of the resonance mode within single photoswitchable molecule-sandwiched MPoFNs under UV light illumination. The above findings not only provide a well platform for studying charge transport in molecular nanojunctions, but also open up a new avenue in the field of active plasmonics.

Chapter 5 Unveiling Electron Transport in Gold Sphere Plasmonic Nanomatryoshkas (GSPNs) with Two-Photon Luminescence (TPL) Spectroscopy

In the plasmonic nanocavities, charge transport across molecular junctions is usually confirmed by observing a new plasmon mode, i.e. a CTP mode[60, 77, 82, 162]. Nevertheless, in other configurations, charge transport even if strong enough does not necessarily generate the CTP mode but leads to the quenching of several old modes. This is typically the case for plasmonic nanomatryoshkas that refer to metallic NPs with interior small gaps[163-171]. Several recent studies have shown that the low-energy mode (LEM) of a gold sphere plasmonic nanomatryoshka (GSPN) will disappear when the charge transport between the core and shell is prominent[167, 170-172]. Although absence of the LEM in principle can be inspected by some far-field spectroscopies such as dark-field scattering and UV-Vis spectra, these observations sometimes are not robust[85, 167]. This is because the far-field responses of the LEM are relatively weak in ultra-small junction width. Especially in experiments, the LEM may only exhibit weak scattering intensity and broad linewidth. On the contrary, the near-field enhancement of LEM can be quite sensitive, making it more appropriate to investigate the charge transfer effect in plasmonic nanomatryoshkas by various near-field spectroscopies.

Recently, molecule-assisted charge transport in GSPNs has been studied by SERS[85]. In this Chapter, I further demonstrate that the charge transport across molecular nanojunctions has strong impact on the two-photon luminescence (TPL) emission of the GSPN. Synthesized GSPNs with nanojunctions filled

with three types of dithiol molecules that have 1-3 benzene rings were employed to fully investigate their TPL responses. Particularly, QCM considering different assumptions of junction conductance is used in the simulations. Comparison between the measured TPL intensity as a function of excitation wavelength and the corresponding calculations reveals that the charge transfer effect dramatically impairs the TPL enhancement via LEM. The results of this work can provide a feasible way to study the molecular-assisted charge transport by nonlinear optical spectroscopies.

5.1 Linear Optical Response of GSPNs

Linear optical response of GSPNs has been extensively investigated both numerically and experimentally[166]. According to these studies, the optical resonances of a GSPN can be basically understood as the hybridization between plasmon modes of the outer shell and the inner core[85, 167, 170-172]. From this perspective, the distance between the shell and the core, i.e., the junction width, is one of the most important factors that determine the resonant properties (such as resonance wavelength, scattering cross section and near-field enhancement) of a GSPN.

In this work, GSPNs with interior nanojunctions were synthesized via a wet-chemistry approach (see Fig. 2.4). The junctions were formed by three kinds of dithiol molecules: 1,4-benzenedithiol (BDT), 4,4'-biphenyldithiol (BPDT), and 4,4'-terpheyldithiol (TPDT). Although a few metallic bridges may generate in such nanojunctions during the growth of shell, the impact of these bridges on the optical response of GSPNs is fairly limited compared to that by charge transfer effect[85]. The structures of molecules are shown by the top insets in Fig. 5.1(a)-(c), respectively. The statistically averaged junction

widths of the GSPNs embedded with BDT, BPDT, and TPDT molecules were obtained as 0.7 nm, 0.9 nm, and 1.5 nm, respectively. In addition, TEM images of the GSPNs are shown in the bottom insets in Fig. 5.1(a)-(c) from which the radii of the gold core and the outer gold shell are estimated as 10 nm and 30 nm for all the synthesized GSPNs.

I first studied the far-field response of the above samples by measuring their UV-Vis spectra. As can be seen from Fig. 5.1, each extinction spectrum exhibits a single peak of the HEM near 535 nm, whereas the feature of LEMs cannot be found in the spectra. This phenomenon is consistent with the previous studies, which imply that the LEMs in GSPNs embedded with such dithiol molecules are quenched because of the significant charge transfer effect. The corresponding dark-field spectra were also obtained as shown in Fig. 5.1(d)-(f) before and after TPL measurements, which indicates no photodamage induced by femtosecond laser irradiation.

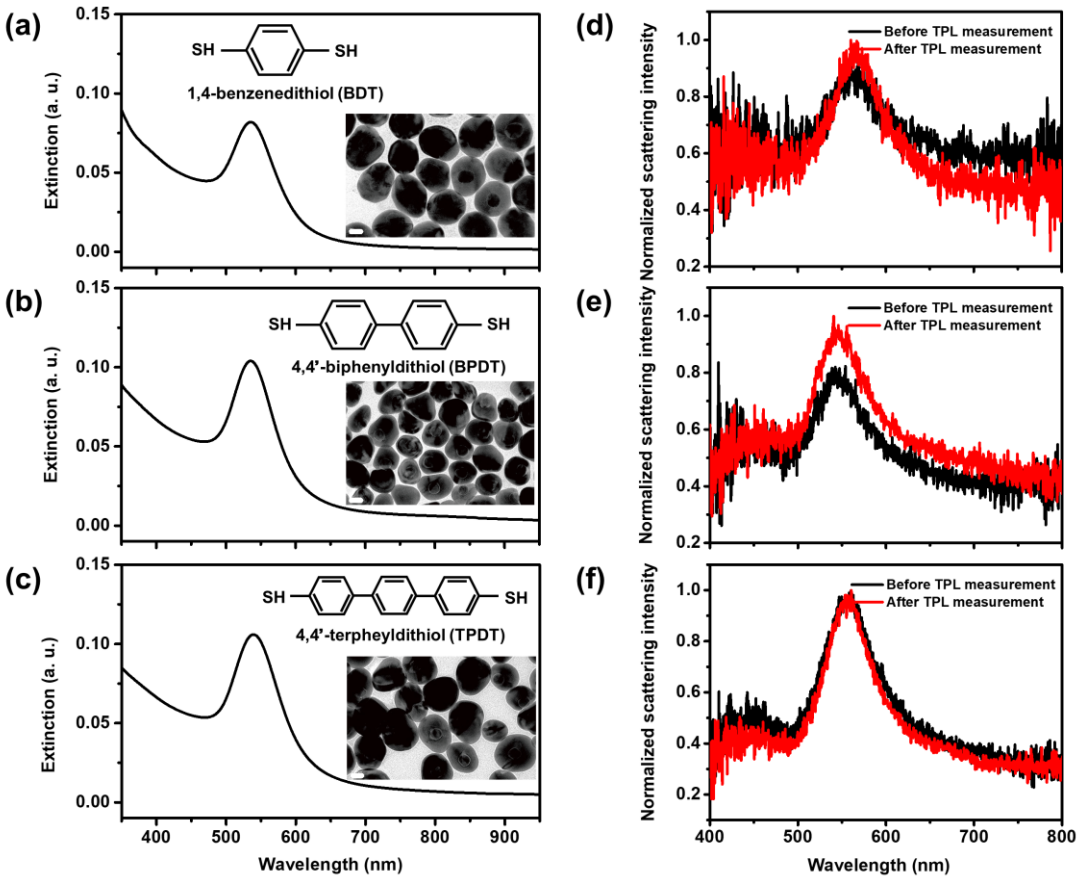

Figure 5.1 Far-field experimental characterization of GSPNs with (a) BDT molecular junction, (b) BPDT molecular junction, and (c) TPDT molecular junction. TEM images of the samples and the molecular structures are shown by the bottom and top insets, respectively. The scale bars of the TEM images in (a)-(c) are 20 nm. (d-f) Scattering spectra of the corresponding GSPNs in (a)-(c) taken before and after TPL measurements.

To obtain more information on the GSPN, I numerically investigated the linear optical response of a GSPN with junction width varying from 0.7 to 10 nm, whereas the radii of the inner core (r_1) and the outer shell (r_2) are kept as 10 and 30 nm, respectively (see the inset in Fig. 5.2(a)). For simplicity, the GSPN embedded with a dielectric junction (refractive index 1.60) is assumed to be free-standing in air. Mie scattering code is applied to acquire both the far-field and near-field optical responses of the GSPN under excitation of a linearly polarized plane wave[173].

Figure 5.2(a) shows map of the normalized extinction cross section of the GSPN as a function of the junction width in the wavelength range of 400-1200 nm. It can be seen that there are two prominent resonance bands of which the spectral features have different dependence on the junction width. The high-energy band is almost fixed at 515 nm, which can be viewed from the resonance wavelength as a function of the junction width (gray dotted-line). Meanwhile, the extinction cross section of this high-energy band is also insensitive to the junction width. Conversely, resonance wavelength of the low-energy band red-shifts as the junction width decreases (white dotted-line) along with reinforcing the extinction cross section. Figure 5.2(b) shows the extinction spectrum of the GSPN with a certain junction width (2 nm). The resonance peak at 515 nm corresponds to a high-energy mode (HEM), while the one at 800 nm is a low-energy mode (LEM). The transient surface charge distributions of the LEM and the HEM are shown by the insets close to the extinction peaks. Note that for the HEM (LEM) the charge density on the exterior surface of the GSPN is larger (much smaller) than that on the interior surfaces (the inner surface of the shell and the surface of the core). This discrepancy explains why the optical response of the HEM is less sensitive to the junction width than that of the LEM.

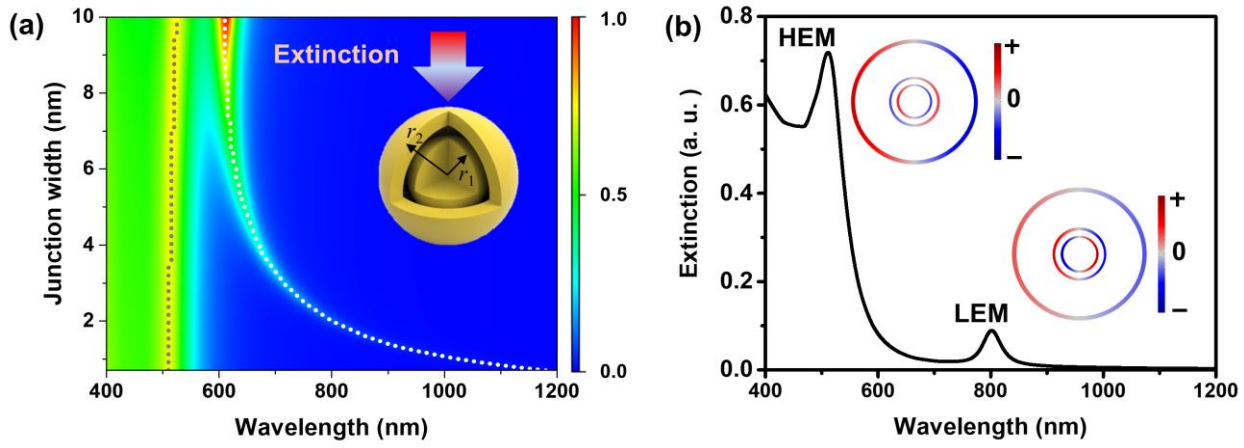

Figure 5.2 Linear optical responses of the GSPN as a function of the junction width varying from 0.7 to 10 nm. (a) Normalized extinction cross section as a function of the junction width in the wavelength range of 400-1200 nm. The GSPN

is assumed to be free standing in air and excited by a linearly polarized plane wave. The gray (white) dotted-line guides the wavelength of the maximum extinction of the high (low) energy band as a function of the junction width. (b) Spectrum of the normalized extinction cross section of the GSPN with 2 nm junction. The insets close to the extinction peaks illustrate the corresponding transient surface charge distribution on the metal surfaces at the LEM and HEM.

In addition to the far-field optical responses, the near-field properties of the GSPN is more attractive in this work as plenty of nonlinear optical phenomena such as SHG and TPL are closely related to the plasmonic near-field enhancement. At the same time, the conclusion drawn from the far-field experimental results may not be reliable due to the fact that the absence of the LEM in the UV-Vis spectra may also originate from the spectral suppression and broadening effects caused by the defects of the samples and the average effect of multiple NPs. Therefore, surveying the near-field response of GSPNs is arguably a more appropriate method to probe the charge transport in GSPNs with molecular nanojunctions.

Figure 5.3(a) plots the normalized near-field EF $|\mathbf{E}_{\mathrm{loc}}/\mathrm{E}_0|$ monitored at the center of the junction (see the red dot in the inset) as a function of the junction width in the wavelength range of 400-1200 nm, where $\mathbf{E}_{\mathrm{loc}}$ is the local electric field and E_0 is the amplitude of the incident plane wave. It is clearly seen that the near-field EF of the LEM in the junction area is much larger than that of the HEM. Hence, GSPNs can serve as excellent surface-enhanced Raman tags when dithiol molecules are embedded within the gap area[164-166, 174]. Interestingly, Figure 5.3(a) indicates that the near-field EF of the LEM in the junction region does not monotonously increase when the junction shrinks. That is to say, there exists an optimal junction width that provides the maximum local field enhancement in the junction region. Considering the geometrical symmetry of the GSPN, the spatial distribution of the near-field

enhancement can be simply studied by calculating $|\mathbf{E}_{loc}/E_0|$ along the *x*-coordinate from the center of the core (x = 0 nm) to 10 nm away from the outer surface of the shell (x = 30 nm). Figure 5.3(b) shows the spectra of $|\mathbf{E}_{loc}/E_0|$ with respect to the LEM and HEM for the GSPN with 2 nm junction width, which demonstrates that the strongest near-field EF of the LEM resides in the gap area and can be larger than 10. Besides, it is worthy to notice that the electric fields inside the gold core with respect to both the LEM and the HEM can also be magnified, though the EFs are not so large in comparison to that inside the junction region. However, the near-field enhancement inside the metal region is crucial for some bulk absorption related nonlinear optical phenomena, for example the plasmon-assisted TPL emission.

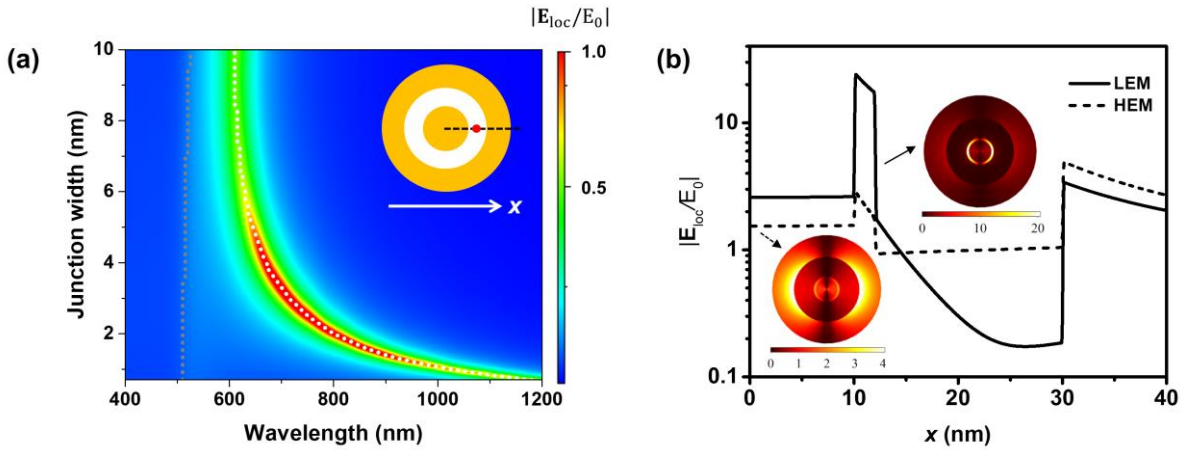

Figure 5.3 (a) Near field EF $|\mathbf{E}_{loc}/E_0|$ monitored at the junction center as a function of the junction width in the wavelength range of 400-1200 nm. The inset shows the monitoring point (red dot) and the *x*-coordinate. (b) Near field EF $|\mathbf{E}_{loc}/E_0|$ of the GSPN with 2 nm junction along the *x*-coordinate from the center to the edge of the GSPN as marked by the black dashed line in the inset in (a). The solid and dashed lines correspond to the LEM and HEM, respectively.

5.2 Two-Photon Luminescence Response of GSPNs with Different Molecular Junctions

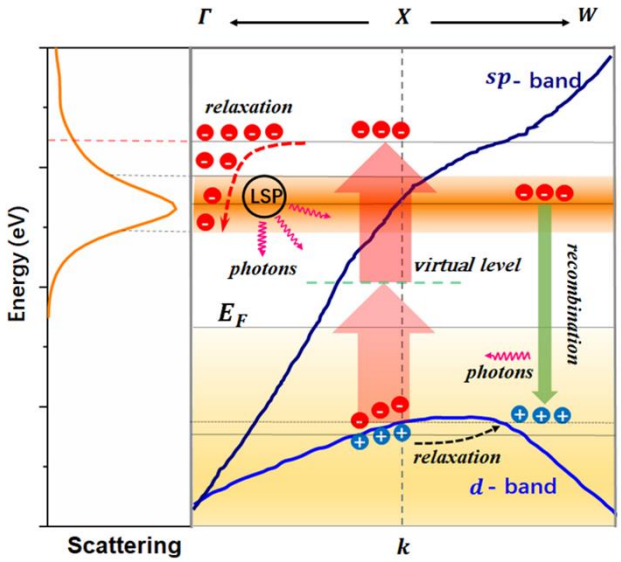

Figure 5.4 Schematic of the plasmon-assisted TPL emission process of Au NPs.

Based on the physical picture of the plasmon-assisted TPL emission (see Fig. 5.4), the TPL emission intensity from an infinitesimal volume dV of a plasmonic NP can be expressed as[175-179]:

$$I_{\mathrm{TPL}}(\omega_{\mathrm{em}}, \mathbf{r}) \cdot dV = I^2(\omega_{\mathrm{ex}}, \mathbf{r}) \cdot Y_{2\mathrm{abs}}(2\omega_{\mathrm{ex}}) \cdot Y_{\mathrm{R}}(\omega_{\mathrm{em}}) \cdot Y_{\mathrm{em}}(\omega_{\mathrm{em}}) \cdot dV \tag{5.1}$$

Here, $\omega_{\mathrm{em}}(\omega_{\mathrm{ex}})$ is the angular frequency of the emission (excitation), $I(\omega_{\mathrm{ex}}, \mathbf{r})$ denotes the excitation intensity at position $\mathbf{r}$, $Y_{2\mathrm{abs}}(2\omega_{\mathrm{ex}})$ refers to the absorption probability of two photons for generating energetic electron-hole pairs with energy of $2\hbar\omega_{\mathrm{ex}}$, $Y_{\mathrm{R}}(\omega_{\mathrm{em}})$ is the relaxation probability of the energetic electron-hole pairs with the emission energy of $\hbar\omega_{\mathrm{em}}$, and $Y_{\mathrm{em}}(\omega_{\mathrm{em}})$ refers to the emission probability of the radiative recombination in bulk metals but mediated by the plasmonic antenna effect. In Eq. (5.1), both $Y_{2\mathrm{abs}}(2\omega_{\mathrm{ex}})$ and $Y_{\mathrm{R}}(\omega_{\mathrm{em}})$ are determined by the intrinsic properties of the metal. The excitation intensity $I(\omega_{\mathrm{ex}}, \mathbf{r})$ is equal to $|\mathbf{E}_{\mathrm{loc}}(\omega_{\mathrm{ex}}, \mathbf{r})|^2$, where $\mathbf{E}_{\mathrm{loc}}(\omega_{\mathrm{ex}}, \mathbf{r})$ is the local electric

field at ω_{ex} and position $\mathbf{r}$. The plasmon-mediated emission probability $Y_{em}(\omega_{em})$ is essentially related to the local density of plasmonic states, which is proportional to the local field intensity at ω_{em}, i.e., $|\mathbf{E}_{loc}(\omega_{em}, \mathbf{r})|^2$. Actually, above-mentioned luminescence emission process is associated with the Purcell effect in which the magnitude of enhancement (Purcell factor) is closely related to field enhancement. Going back to Fig. 5.3(b), It can be concluded that the near-field enhancement of the LEM inside the metal region is beneficial for enhancing $I(\omega_{ex}, \mathbf{r})$, whereas the excitation at HEM contribute to photon emission at short wavelengths, i.e. promoting $Y_{em}(\omega_{em})$. Equation (5.1) can be further reduced to Eq. (5.2) by dropping $Y_{2abs}(2\omega_{ex})$ and $Y_R(\omega_{em})$ when we only consider about the relative TPL intensity of NPs with the same composition.

$$I_{TPL}^{rel}(\omega_{em}, \mathbf{r}) \cdot dV \propto L_{ex}(\omega_{ex}, \mathbf{r}) \cdot L_{em}(\omega_{em}, \mathbf{r}) \cdot dV \tag{5.2}$$

In Eq. (5.2), $L_{ex}(\omega_{ex}, \mathbf{r}) = |\mathbf{E}_{loc}(\omega_{ex}, \mathbf{r})/E_0|^4$ and $L_{em}(\omega_{em}, \mathbf{r}) = |\mathbf{E}_{loc}(\omega_{em}, \mathbf{r})/E_0|^2$ correspond to the near-field EFs at the excitation and emission wavelength, respectively.

To fully understand the plasmon-assisted TPL emission process, I first carried out single NP TPL experimental characterization, which is different from the UV-Vis spectroscopy measuring the extinction spectra of NPs in solution. Figure 5.5(a) schematically demonstrates the TPL testing system based on a commercial laser scanning confocal microscope equipped with a Ti:sapphire femtosecond laser. Figure 5.5(b) shows the false color image of the TPL emission from a sample of GSPNs embedded with a certain molecular nanojunctions, which exhibits light spots of different size. Then the nonlinear emission image was combined with the corresponding dark-field image from the same region to discern single NPs for further spectra acquisition. Moreover, the NPs were not evidently damaged by the femtosecond laser irradiation due to the fact that both the dark-field scattering spectra and images exhibited no

observable changes before and after the TPL measurements. The measured (symbols) and fitted (red line) TPL spectra of a single GSPN show an emission peak near 550 nm as illustrated in Fig. 5.5(c). Note that the TPL intensity was acquired by collecting the emission from the area that covers only one NP. The area size and excitation power of the laser were the same for each kind of sample.

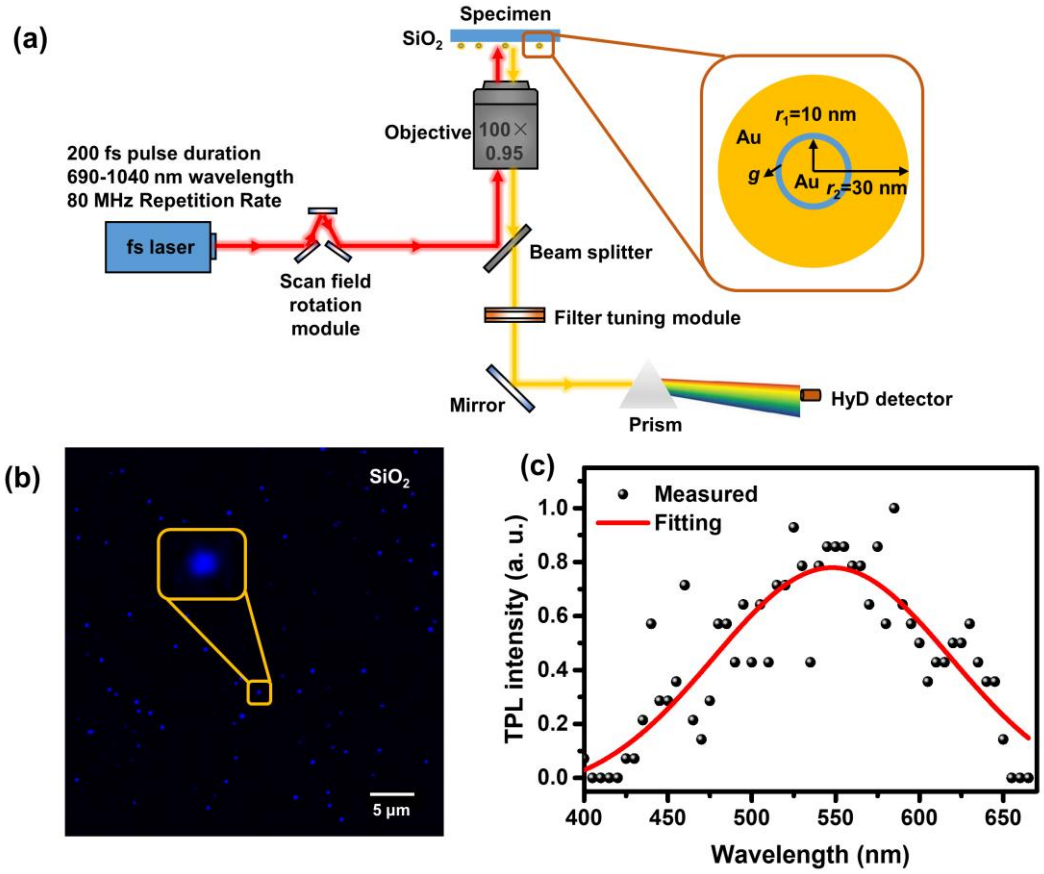

Figure 5.5 Experimental TPL characterization of GSPNs embedded with molecular junctions. (a) Schematic of the confocal TPL spectroscopy system. (b) TPL false color images of GSPNs (average 1.5 nm junction width) placed on a glass substrate. (c) Measured (symbols) and fitted (line) TPL spectra of a GSPN (marked by the yellow square in Fig. 5.5(b)).

TPL response of GSPNs was also calculated based on Eq. (5.2). All the geometries and material properties in the simulation models are selected according to the synthesized NPs in the experiments. Specifically, the radii of the outer shell and the inner core of GSPNs are kept as 30 and 10 nm,

respectively. Besides, GSPNs are placed on a glass substrate in simulations in order to be consistent with the experiments. Firstly, the GSPNs with dielectric junctions of three different widths (0.7, 0.9 and 1.5 nm) were considered. The refractive index for the 0.7 nm junction was set to 1.59, and that for 0.9 and 1.5 nm junctions was 1.65. For comparison, the TPL response of a solid Au NS (30 nm in radius) was also calculated in the simulation. Figure 5.6(a) shows the spectra of the relative TPL intensity with respect to the Au NS and the GSPNs excited by a linearly polarized plane wave with amplitude E_0 and wavelength 750 nm. Obviously, all the spectra demonstrate a TPL emission peak near 525 nm in the emission wavelength (λ_{em}) ranging from 400 to 650 nm. The results verify that the TPL emission of the GSPN is enlarged by the plasmonic antenna effect of the HEM, which red-shifts to 525 nm as a consequence of the presence of substrate. For the Au NS, the TPL emission peak is considered as the electric dipole mode of which the resonance wavelength is close to that of the HEM of the GSPN. For the GSPN, one can find that the TPL response depends on the junction width. For instance, the TPL intensity of the GSPN with 1.5 nm junction width is overall larger than that of others with smaller junction width. Additional calculations of the GSPN excited at other wavelengths (see Fig. 5.7) suggest that TPL intensity is also magnified by the LEM of which the resonance wavelength depends on the junction width. In Figure 5.6(b), I compare the TPL intensity of the GSPNs and the solid Au NS, integrated in the emission wavelength ranging from 400 to 650 nm, as a function of the excitation wavelength (λ_{ex}). Similarly, the integrated TPL intensity of GSPNs with different junction widths exhibits peaks at the resonance wavelengths of the LEMs, while that of a solid Au NS without the LEM monotonously decreases in the excitation wavelength ranging from 700 to 1200 nm. Hence, it is clear that both the spectral position and near-field EF of the LEM determine the dependence of the integrated TPL intensity as a function of λ_{ex}. Compared to the numerical results illustrated in Fig. 5.6(a), the measured TPL spectrum is broader and red-shifted due to the imperfections of the synthesized NPs.

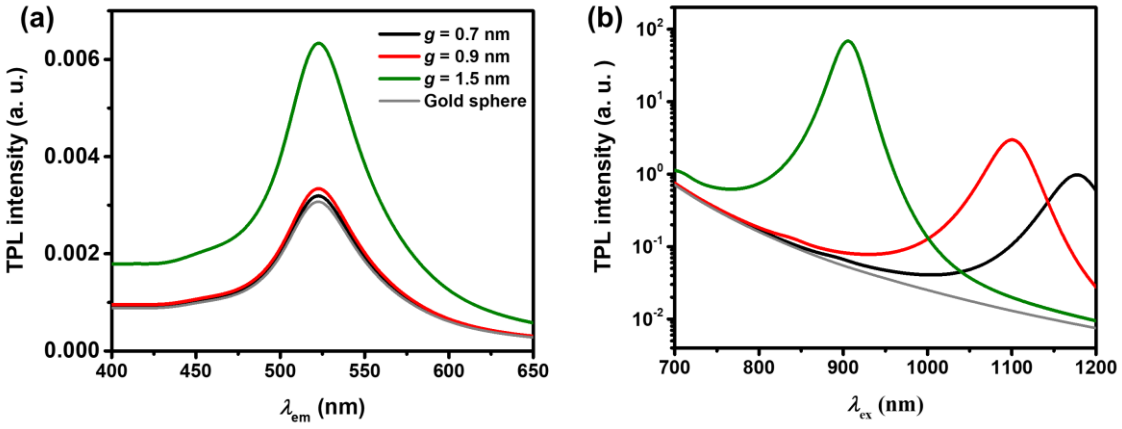

Figure 5.6 Calculated TPL responses of GSPNs with junction width (denoted as g) of 0.7, 0.9 and 1.5 nm based on different models of the junction conductance. (a) Relative TPL intensity of GSPNs as a function of the emission wavelength (λ_{em}) excited at 750 nm calculated based on a classical dielectric junction model. (b) Integral TPL intensity as a function of the excitation wavelength (λ_{ex}) calculated based on the same model as used in (a).

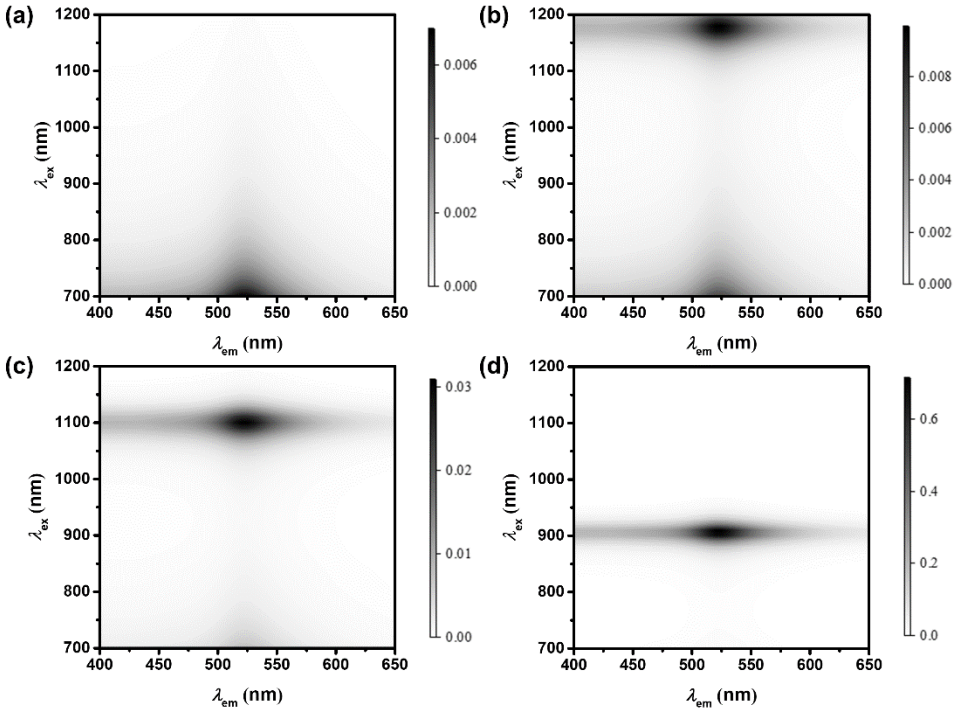

Figure 5.7 TPL intensity as a function of the emission wavelength λ_{em} (400 to 650 nm) and the excitation wavelength λ_{ex} (700 to 1200 nm). (a) A solid Au NS, (b) the GSPN with insulating junction of 0.7 nm, (c) the GSPN with insulating junction of 0.9 nm, (d) the GSPN with insulating junction of 1.5 nm.

5.3 Influence of Electron Transport on Two-Photon Luminescence Response of GSPNs

After analyzing both linear and TPL responses of GSPNs with dielectric nanojunctions, it is now possible to investigate how charge transport in the nanojunction influences the TPL response of the GSPN. In the simulation, the junction need to be treated as a conductive material with a complex dielectric function when charges can transport across it. This is the principle of the QCM that has been most commonly employed in the study of charge transfer effect in plasmonic nanostructures. Based on the QCM, the relative permittivity of the conductive gap $\varepsilon_{\mathrm{gap}}$ can be expressed as[77, 83, 85, 180]:

$$\varepsilon_{\mathrm{gap}} = n_{\mathrm{d}}^2 + \frac{\mathrm{i}\sigma_{\mathrm{gap}}}{\omega\varepsilon_0} \tag{5.3}$$

where n_{d} is the real part of the refractive index, i is the imaginary unit, and ε_0 is the permittivity of the vacuum. The most important parameter in Eq. (5.3) is the conductivity σ_{gap}, which is related to the junction conductance G_{gap}. For a spherical conductor with interior junctions, the relationship between σ_{gap} and G_{gap} follows[85]:

$$G_{\mathrm{gap}} = \frac{\sigma_{\mathrm{gap}} \cdot 4\pi r_1 (r_1 + g)}{g} \tag{5.4}$$

where g denotes the junction width. If the junction in the GSPN is treated as a classical circuit element, σ_{gap} should be a constant for different junction widths as it is the intrinsic material property. In this classical circuit model, G_{gap} is nearly proportional to $1/g$ according to Eq. (5.4). However, for charge transport across molecular junctions, many studies have revealed that G_{gap} exponentially attenuates as the junction width increases[181-187]:

$$G_{\mathrm{gap}}(g) = G_{\mathrm{gap}}^0 \exp[-\beta \cdot (g - g_0)] \tag{5.5}$$

where G_{gap}^{0} denotes the conductance of the shortest junction with initial width g_0, and β is the decay factor. In the following numerical calculations, G_{gap}^{0} is assumed to be 250 times larger than the quantum conductance G_0 (7.745×10^{-5} S). This presumption is based on the previous study, in which the conductance of a single 1,4-benzenedithiol (BDT) molecule was estimated as 0.044 G_0[85].

There have been many investigations indicating that β is primarily determined by two factors: barrier height and mechanism of the charge transport[183-185]. For the direct tunneling across conjugated molecules, β is typically in the range of 1-3 nm^{-1} and can become much smaller (for example 0.3 nm^{-1}) when the nature of charge transport process was changed from tunneling to hopping[187]. Fig. 5.8(a) shows spectra of the integrated TPL intensity as a function of the excitation wavelength ranging from 700 to 1200 nm, which was calculated based on Eq. (5.5) by considering different values of β. The results show that for a larger decay factor (β = 3 nm^{-1}), the spectra of the TPL intensity still exhibit distinct peaks at the resonance wavelengths of LEMs for GSPNs with relatively large junction widths (g = 0.9 and 1.5 nm), although the strengths are much smaller than those calculated based on the insulating model (Fig. 5.6(b)). This observation reveals that the charge transport in GSPNs with large junction widths is not sufficient to completely quench the LEM due to the fact that tunneling probability with β = 3 nm^{-1} quickly reduces as the junction width increases. Nevertheless, when more efficient charge transport occurs (for example hopping), the decay of junction conductance can be much slower, leading to strong quenching of the LEM even for a large junction width. This can be verified by the spectra of β = 0.3 nm^{-1} for g = 0.9 and 1.5 nm in Fig. 5.8(a), where the peaks of the TPL intensity at the resonance wavelengths of the LEM almost disappear. One can also consider a special case that the junction conductance is totally independent on the junction width, i.e. β = 0. Then the charge transport across molecular junctions is

always intense enough to completely quench all the LEMs for different junction widths as illustrated by the dash-dotted lines in Fig. 5.8(a). Under this circumstances, TPL response of the GSPNs becomes very similar to that of a solid Au NS (solid gray line), which shows a monotonously decreasing trend when λ_{ex} increases from 700 to 1200 nm. In Figure 5.8(b), I compare the calculated near-field enhancement (L_{ex}) of the LEM from the center of the core to 10 nm away from the outer surface of the shell based on the insulating junction model and molecular junction model with β = 0.3 nm^{-1}, which indicates that near-field enhancement is largely reduced in the GSPN with a molecular nanojunction due to the strong charge transfer effect. Furthermore, the field reduction mainly occurs inside the nanojunction and metal regions close to it, while the field distribution outside the shell is robust, as shown by the L_{ex} distribution across the cross section of the GSPN with an insulating (left inset) and molecular junction (right inset). One can also observe that the HEM (resonance at the short wavelength) is nearly insensitive to the charge transport, which results in the same field distributions in GSPNs with an insulating and a molecular junction (see Fig. A3).

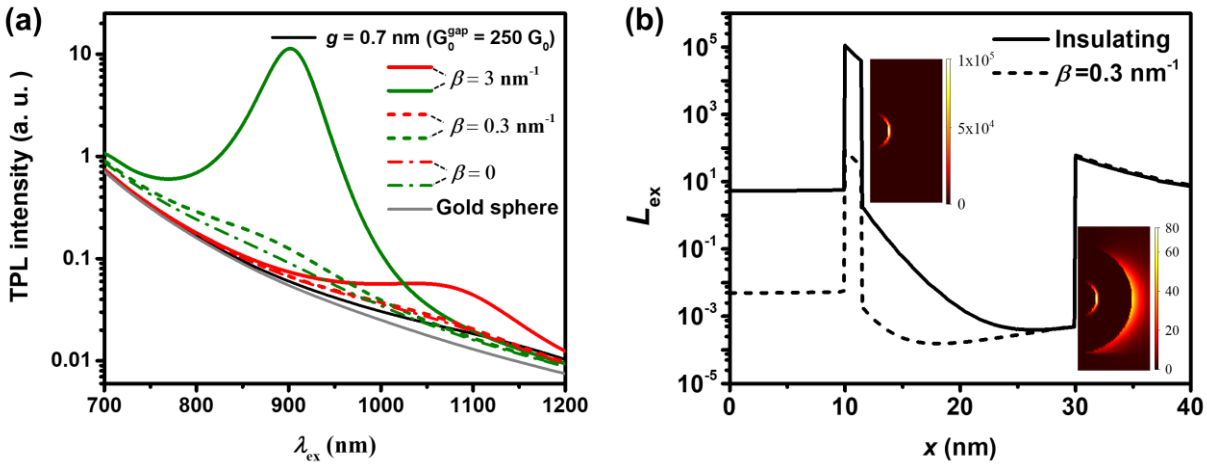

Figure 5.8 (a) Integral TPL intensity as a function of the excitation wavelength (λ_{ex}) calculated based on the tunneling-type model. TPL intensity of a solid gold sphere is appended in (a) by the gray line. Note that the results of g = 0.7 nm for different β are the same as shown by the black solid line. (b) Near-field EF (L_{ex}) from the center to 10 nm away from the

outer shell of the GSPN calculated at the excitation wavelength of the LEM based on the insulating model (solid line) and the tunneling-type model with β = 0.3 nm^{-1} (dashed line). The left and right insets show the distribution of L_{ex} on the intersecting surface of the GSPN.

Next, I try to experimentally investigate the charge transport across molecular junctions by measuring the integrated TPL intensity of GSPNs as a function of the excitation wavelength in the emission wavelength range of 400 to 650 nm, and comparing it with the corresponding calculations. Unfortunately, limited by the laser system, the wavelength of the reliable excitation in the experiment can only be tuned from 715 to 800 nm. Symbols in Fig. 5.9 show the measured TPL intensity versus the excitation wavelength for a solid Au NS, GSPNs with BDT, BPDT, and TPDT nanojunctions in (a)-(d), respectively. To make a reasonable comparison between the experimental and numerical results, the measured data were fitted by using the errors as weight, then the fitted and calculated spectra were normalized to the intensity at 715 nm. Firstly, for a solid Au NS the measured TPL intensity (solid line in Fig. 5.9(a)) reduces as the excitation wavelength increases, which agrees with the trend of the numerical spectrum (dashed line in Fig. 5.9(a)). Then, for GSPNs with shorter molecular junction widths (BDT and BPDT), the calculated TPL intensity obtained by considering an insulating junction and a molecular junction with different value of β has no observable distinctions in the excitation wavelength range of 715-800 nm, as illustrated by the dashed lines in Fig. 5.9(b) and 5.9(c). Both the measured and calculated TPL intensity decrease as the excitation wavelength increases, which is similar to the results of a solid Au NS shown in Fig. 5.9(a). This can be understood by the fact that the resonance wavelengths of LEMs of GSPNs with shorter junction width (0.7 and 0.9 nm) are far beyond 800 nm as disclosed by the numerical calculations shown in Fig. 5.6(b). In this context, whether the charge transport happens or not cannot be concluded from the results in Fig. 5.9(b) and 5.9(c). Yet, for GSPNs with a longer molecular junction

width (TPDT, 1.5 nm), the resonance wavelength of the LEM is about 900 nm (see Fig. 5.6(b)), which is close to the edge of window of the excitation wavelength range (715 to 800 nm) in Fig. 5.9. Therefore, the variation trend of the TPL intensity as a function of λ_{ex} is different for numerical calculations based on different models of junction conductance (as shown in Fig. 5.9(d)). In short, when the junction is completely insulating (black dashed-line) or the junction conductance is quite small (for example in the tunneling-type model with β = 3 nm^{-1} (blue dashed-line)), the TPL intensity first decreases then increases in the excitation wavelength range of 715-800 nm. Otherwise, when β = 0.3 nm^{-1} (olive dashed-line) and β = 0 (pink dashed-line), the TPL intensity decreases all the way in the same excitation wavelength range. Clearly, the measured results in Fig. 5.9(d) can match the numerical calculations only when highly conductive molecular junctions with slow decay factors (β = 0 and β = 0.3 nm^{-1}) are considered in the simulation. Hence, it is believed that the results shown in Fig. 5.9(d) provide another experimental evidence of the significant charge transport process in the molecular junctions. As the TPL response (Fig. 5.9) is closely related to the near-field properties of the GSPN, it is more convinced than the far-field results (Fig. 5.6 and 5.8) in terms of identifying the charge transport in molecular junction.

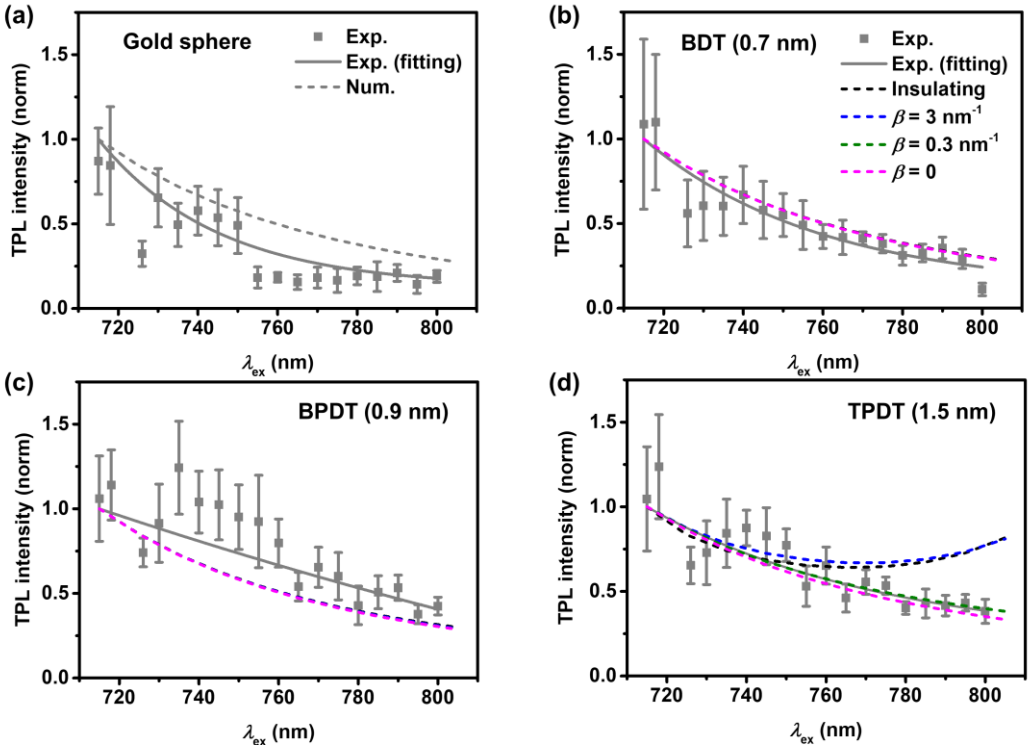

Figure 5.9 Comparison between the experimentally measured TPL responses of gold sphere as well as GSPNs and numerical results calculated based on different models. Measured (symbols) and calculated (dashed-lines) integral TPL intensity of (a) a solid gold sphere, GSPNs with (b) BDT, (c) BPDT, and (d) TPDT molecular junctions, as a function of the excitation wavelength (λ_{ex}) in the range of 715-800 nm. The solid lines are the fitted curves of the experimental data and (b)-(d) share the same legends. The error bars represent standard deviations of the TPL intensity of several NPs at each excitation wavelength.

5.4 Conclusion

In summary, I investigated the TPL response of GSPNs embedded with molecular nanojunctions and found that the charge transport across the junctions has strong impact on the nonlinear optical response. Together with the experimental spectra, theoretical and numerical results have demonstrated that the near-field enhancement of the LEM inside the metal regions is also significantly quenched due to the charge transfer effect. As a result, the TPL response of GSPNs with highly conductive molecular junctions is similar to that of a solid Au NS, which has been verified by both the numerical calculations

and experimental measurements. The results indicate that in addition to the SERS characterization, TPL spectroscopy can be employed as another efficient near-field probe to explore the charge transfer effect in plasmonic molecular nanocavities. The mechanism of charge transport is at the heart of the molecular electronics and has been extensively studied in molecular wires under DC bias[183-187]. Nevertheless, charge transport in molecular junctions under optical frequencies can be very different from that under DC bias because many plasmon-related effects can be involved in this process, for example plasmon-induced hot electrons[188]. In this respect, this work provides a useful insight regarding how to shed light on charge transport mechanisms across molecular junctions under optical frequencies by plasmon-enhanced spectroscopy.

Chapter 6 Conclusion and Outlook

My studies throughout this thesis include exploring all-optical modulation of both linear and nonlinear emissions in PNSs. First of all, comprehensive theoretical calculations as well as far- and near-field optical spectroscopic measurements were combined to probe the near-field enhancement limit in graphene-coupled MPoFNs. Together with classical local and quantum nonlocal calculations, the experimental SERS results clearly reveal that the in-plane near-field enhancement is strongly mitigated by the nonlocal screening effect when the gap thickness approaches to sub-nanometer scale. Different from the previous studies, for the first time, I carried out rigorously correlated morphological characterizations and optical spectroscopies exactly on the same MPoFNs in order to avoid ambiguities caused by possible geometric variation from structure to structure. Consistent with the nonlocal model predictions, both near-field SERS EF and far-field plasmon resonance shift exhibit a quantum mechanical limit to the gap width of the MPoFNs.

Then, I experimentally investigated quantum charge transport in the organic molecule-sandwiched MPoFNs. A blue-shift of the hybridized plasmon modes of the scattering spectra was clearly observed in conductive molecule (BPDT) sandwiched MPoFNs in contrast to that in MPoFNs with junctions formed by insulating molecule (B4T), which suggests that electron transport occurs in the molecular junction. To better understand the origins of major plasmon modes observed in scattering spectra, polarization-dependent dark-field spectroscopy was performed on each molecule-sandwiched MPoFN. Furthermore, as one of the near-field characterization approaches, SERS spectra were also measured on

individual molecular nanocavities to disclose charge transport across molecular nanojunctions. Specifically, in single-particle SERS measurement, several-fold reduction of SERS intensity was observed in conductive molecule-sandwiched MPoFNs compared to insulating counterparts, which is a signature of plasmonic quenching of the near-field enhancement. In addition to above works in passive MPoFNs, single-particle dark-field scattering spectroscopy was also carried out to realize active tuning of the plasmon resonance mode in individual photoswitchable molecule-sandwiched MPoFNs under UV-white light irradiation.

Finally, TPL responses of GSPNs embedded with molecular nanojunctions were studied to reveal the impact of electron transport on the nonlinear optical emissions. In combination with the measured linear and TPL responses of different GSPNs, theoretical and numerical results have indicated that the near-field enhancement of the LEM inside the metal regions is significantly quenched due to the charge transfer effect. As a result, the TPL response of GSPNs with highly conductive molecular junctions is similar to that of a solid Au NS. The results indicate that TPL spectroscopy can be used as an efficient near-field probe to study electron transport in plasmonic nanocavities.

In this thesis, PNSs have been regarded as the effective platform to study all-optical modulation of both linear and nonlinear emissions within classical or quantum regime. On the basis of the promising findings presented in this thesis, I intend to concentrate on several issues in the future research. One is the molecular length dependent charge transfer effect in molecule-sandwiched MPoFNs under optical frequency. The other problem needs to be addressed is to unravel the mechanism of charge transport from Fig. 5.9 by extending the excitation wavelength of the femtosecond laser to a broader range. In

addition, as active control of nonlinear signals in PNSs remains relatively unexplored, there is an urgent need to realize it for a large variety of photonics applications. With the advancement of nanofabrication and characterization, there will be more promising applications in this field.

Appendices

Dielectric Function of the Layered Graphene in Simulations

Layered graphene is modeled as a thin dielectric circular sheet with an anisotropic dielectric constant. The in-plane ($\varepsilon_{\parallel}$) and out-of-plane ($\varepsilon_{\perp}$) components of the graphene dielectric function are determined by:

$$\varepsilon_{\parallel}(\omega, E_{\mathrm{F}}, \Gamma, T) = \varepsilon_{\mathrm{r}} + \mathrm{i}\frac{\sigma(\omega, E_{\mathrm{F}}, \Gamma, T)}{\varepsilon_0 \omega d_{\mathrm{Gr}}} \text{ and } \varepsilon_{\perp} = \varepsilon_{\mathrm{r}} \quad \text{(A.1)}$$

where $\sigma(\omega, E_{\mathrm{F}}, \Gamma, T)$ is the surface conductivity of graphene, ω is angular frequency, E_{F} is the Fermi energy of graphene (which is dependent on the graphene charge carrier concentration), Γ is the scattering rate of electrons in graphene, and T is the temperature. The thickness of the graphene sheet d_{Gr} is 0.34×N nm where N is the layer number and 0.34 nm is the thickness of a graphene monolayer.

The surface conductivity of graphene can be computed within the local-RPA (random-phase approximation) limit[189-191], and is given by:

$$\sigma(\omega, E_{\mathrm{F}}, \Gamma, T) = \frac{-\mathrm{i}e^2}{\pi\hbar^2(\omega+\mathrm{i}2\Gamma)}\int_0^{\infty}\xi\left(\frac{\partial f_{\mathrm{d}}(\xi)}{\partial\xi} - \frac{\partial f_{\mathrm{d}}(-\xi)}{\partial\xi}\right)d\xi + \frac{\mathrm{i}e^2(\omega+\mathrm{i}2\Gamma)}{\pi\hbar^2}\int_0^{\infty}\frac{f_{\mathrm{d}}(-\xi)-f_{\mathrm{d}}(\xi)}{(\omega+\mathrm{i}2\Gamma)^2-4(\xi/\hbar)^2}d\xi \quad \text{(A.2)}$$

where $\Gamma = 1/(2\tau)$ with $\tau = \mu E_{\mathrm{F}}/(ev_{\mathrm{F}}^2)$ being the carrier relaxation lifetime in graphene, v_{F} is the Fermi velocity of graphene, and μ is the carrier mobility in graphene. Other parameters have the same physical meanings as described above.

The first term in Eq. (A.2) corresponds to the intraband electron-photon scattering processes in graphene and the second term originates from the direct interband electron transitions. In my simulations, the Fermi energy of graphene is taken as 0.5 eV and the carrier mobility is assumed to be 1000 $cm^2/(V \cdot S)$ for typical CVD-grown graphene. For few-layered graphene (less than five layers), the out-of-plane polarization is assumed to be extremely weak and the corresponding dielectric constant $\varepsilon_{\perp} = \varepsilon_r = 1$[192].

Power-Dependent Raman Characterization on SLG

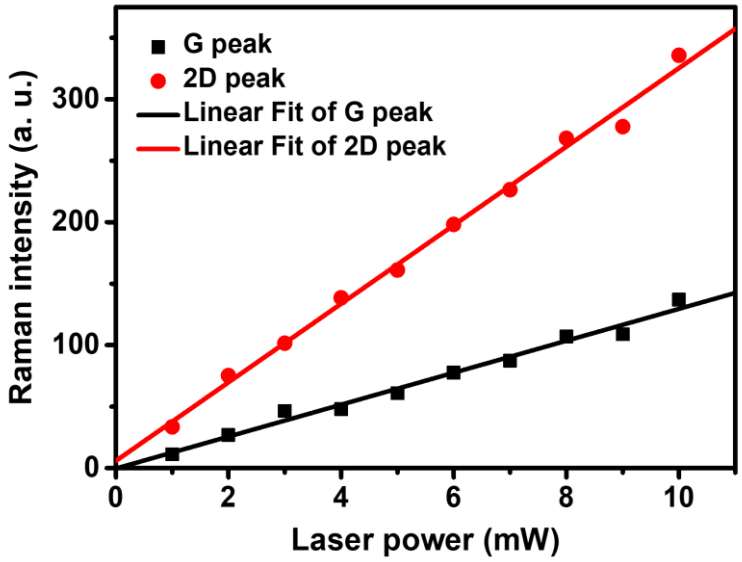

Figure A1 Measured Raman intensities for the G band and 2D band of a CVD-grown SLG on a 100 nm thick Au TF as a function of incident laser power.

Statistics of Measured SERS Enhancement Factors in Graphene-Coupled MPoFNs

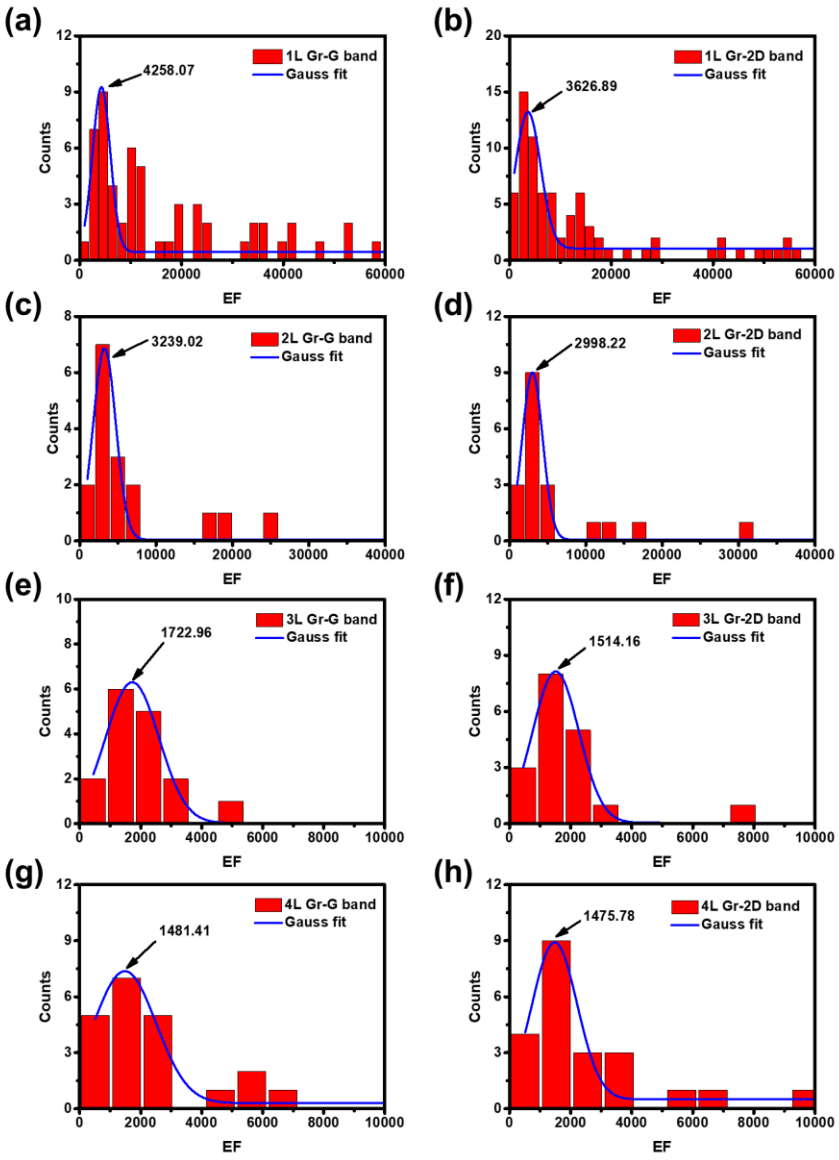

Figure A2 Histograms of SERS EFs measured in four graphene-coupled MPoFNs. The EF distribution in each figure is fitted by a Gaussian model (blue curves).

Near-field Enhancement of the HEM of the GSPN with an Insulating and a Molecular Junction

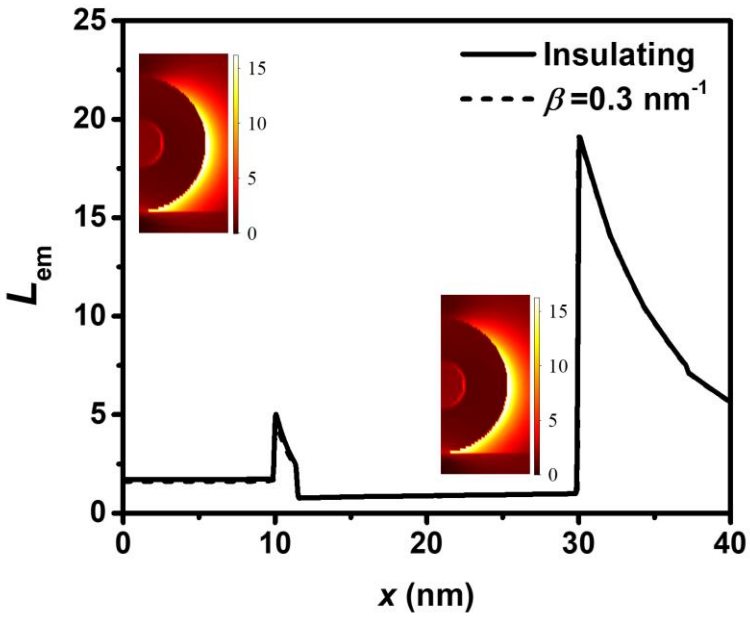

Figure A3 Near-field EF (L_{em}) from the center to 10 nm away from the outer shell of the GSPN calculated at the excitation wavelength of the HEM based on the insulating model (solid line) and the tunneling-type model with β = 0.3 nm^{-1} (dashed line). The left and right insets show the distribution of L_{em} on the intersecting surface of the GSPN.

The Linewidths of the Pump Laser at Different Excitation Wavelengths

Wavelength (nm)	715	718	726	730	735	740	745	750	755
Linewidth (nm)	2.81	6.36	5.46	5.68	5.22	8.59	8.25	8.12	8.32
Wavelength (nm)	760	765	770	775	780	785	790	795	800
Linewidth (nm)	6.52	6.29	8.08	8.11	8.79	8.64	8.32	8.30	8.36

Table A1 Measured linewidths of the Ti:sapphire femtosecond laser in the excitation wavelength ranging from 715 to 800 nm.

References

1. Yu, H.; Peng, Y.; Yang, Y.; Li, Z.-Y. Plasmon-enhanced light–matter interactions and applications. *npj Comput. Mater.* **2019**, *5* (1), 1-14.

2. De Leon, N. P.; Shields, B. J.; Yu, C. L.; Y.; Englund, D. E.; Akimov, A. V.; Lukin, M. D.; Park, H. Tailoring light-matter interaction with a nanoscale plasmon resonator. *Phys. Rev. Lett.* **2012**, *108* (22), 226803.

3. Giannini, V.; Fernández-Domínguez, A. I.; Sonnefraud, Y.; Roschuk, T.; Fernández-García, R.; Maier, S. A. Controlling light localization and light–matter interactions with nanoplasmonics. *Small* **2010**, *6* (22), 2498-2507.

4. Rahmani, M.; Jagadish, C. Light–Matter interactions on the nanoscale. *Beilstein J. Nanotechnol.* **2018**, *9*, 2125-2127.

5. Alvarez-Puebla, R.; Liz-Marzán, L. M.; García de Abajo, F. J. Light concentration at the nanometer scale. *J. Phys. Chem. Lett.* **2010**, *1* (16), 2428-2434.

6. Sorger, V. J.; Oulton, R. F.; Ma, R.-M.; Zhang, X. Toward integrated plasmonic circuits. *MRS Bulletin* **2012**, *37* (8), 728-738.

7. Leuchs, G.; Sondermann, M. Light–matter interaction in free space. *J. Mod. Opt.* **2013**, *60* (1), 36-42.

8. Lienau, C.; Noginov, M. A.; Lončar, M. Light–matter interactions at the nanoscale. *J. Opt.* **2014**, *16* (110201), 110201.

9. Danckwerts, M.; Novotny, L. Optical frequency mixing at coupled gold nanoparticles. *Phys. Rev. Lett.* **2007**, *98* (2), 026104.

10. Roelli, P.; Galland, C.; Piro, N.; Kippenberg, T. J. Molecular cavity optomechanics as a theory of plasmon-enhanced Raman scattering. *Nat. Nanotechol.* **2016**, *11* (2), 164-169.

11. Maier, S. A. *Plasmonics: fundamentals and applications*; Springer Science & Business Media, 2007.

12. Hillenbrand, R.; Taubner, T.; Keilmann, F. Phonon-enhanced light–matter interaction at the nanometre scale. *Nature* **2002**, *418* (6894), 159-162.

13. Vasa, P.; Lienau, C. Strong light–matter interaction in quantum emitter/metal hybrid nanostructures. *ACS Photonics* **2018**, *5* (1), 2-23.

14. Zhang, R.; Zhang, Y.; Dong, Z. C.; Jiang, S.; Zhang, C.; Chen, L. G.; Zhang, L.; Liao, Y.; Aizpurua, J.; Luo, Y.; Yang, J. L.; Hou, J. G. Chemical mapping of a single molecule by plasmon-enhanced Raman scattering. *Nature* **2013**, *498* (7452), 82-86.

15. Barnes, W. L.; Dereux, A.; Ebbesen, T. W. Surface plasmon subwavelength optics. *Nature* **2003**, *424* (6950), 824-830.

16. Wersäll, M. *Strong light-matter interactions and formation of hybrid states at the nanoscale*; Chalmers Tekniska Hogskola (Sweden), 2018.

17. Ebbesen, T. W.; Lezec, H. J.; Ghaemi, H. F.; Thio, T.; Wolff, P. A. Extraordinary optical transmission through sub-wavelength hole arrays. *Nature* **1998**, *391* (6668), 667-669.

18. Kelly, K. L.; Coronado, E.; Zhao, L. L.; Schatz, G. C. The optical properties of metal nanoparticles: the influence of size, shape, and dielectric environment. *J. Phys. Chem. B* **2003**, *107* (3), 668-677.

19. Willets, K. A.; Van Duyne, R. P. Localized surface plasmon resonance spectroscopy and sensing. *Annu. Rev. Phys. Chem.* **2007**, *58*, 267-297.

20. Wang, L.; Hasanzadeh Kafshgari, M.; Meunier, M. Optical properties and applications of plasmonic-metal nanoparticles. *Adv. Funct. Mater.* **2020**, *30* (51), 2005400.

21. Lumdee, C.; Yun, B.; Kik, P. G. Gap-plasmon enhanced gold nanoparticle photoluminescence. *ACS*

Photonics **2014**, *1* (11), 1224-1230.

22. Lombardi, A.; Schmidt, M. K.; Weller, L.; Deacon, W. M.; Benz, F.; De Nijs, B.; Aizpurua, J.; Baumberg, J. J. Pulsed molecular optomechanics in plasmonic nanocavities: from nonlinear vibrational instabilities to bond-breaking. *Phys. Rev. X* **2018**, *8* (1), 011016.

23. Hutter, E.; Fendler, J. H. Exploitation of localized surface plasmon resonance. *Adv. Mater.* **2004**, *16* (19), 1685-1706.

24. Haes, A. J.; Van Duyne, R. P. A unified view of propagating and localized surface plasmon resonance biosensors. *Anal. Bioanal. Chem.* **2004**, *379* (7), 920-930.

25. Thacker, V. V.; Herrmann, L. O.; Sigle, D. O.; Zhang, T.; Liedl, T.; Baumberg, J. J.; Keyser, U. F. DNA origami based assembly of gold nanoparticle dimers for surface-enhanced Raman scattering. *Nat. Commun.* **2014**, *5* (1), 1-7.

26. Lu, G.; Liu, J.; Zhang, T.; Shen, H.; Perriat, P.; Martini, M.; Tillement, O.; Gu, Y.; He, Y.; Wang, Y.; Gong, Q. Enhancing molecule fluorescence with asymmetrical plasmonic antennas. *Nanoscale* **2013**, *5* (14), 6545-6551.

27. Prodan, E.; Radloff, C.; Halas, N. J.; Nordlander, P. A hybridization model for the plasmon response of complex nanostructures. *Science* **2003**, *302* (5644), 419-422.

28. Nordlander, P.; Oubre, C.; Prodan, E.; Li, K.; Stockman, M. I. Plasmon hybridization in nanoparticle dimers. *Nano Lett.* **2004**, *4* (5), 899-903.

29. Nordlander, P.; Prodan, E. Plasmon hybridization in nanoparticles near metallic surfaces. *Nano Lett.* **2004**, *4* (11), 2209-2213.

30. Atay, T.; Song, J.-H.; Nurmikko, A. V. Strongly interacting plasmon nanoparticle pairs: from dipole−dipole interaction to conductively coupled regime. *Nano Lett.* **2004**, *4* (9), 1627-1631.

31. Funston, A. M.; Novo, C.; Davis, T. J.; Mulvaney, P. Plasmon coupling of gold nanorods at short

distances and in different geometries. *Nano Lett.* **2009**, *9* (4), 1651-1658.

32. Muskens, O. L.; Giannini, V.; Sánchez-Gil, J. A.; Rivas, J. G. Optical scattering resonances of single and coupled dimer plasmonic nanoantennas. *Opt. Express* **2007**, *15* (26), 17736-17746.

33. Reinhard, B. M.; Siu, M.; Agarwal, H.; Alivisatos, A. P.; Liphardt, J. Calibration of dynamic molecular rulers based on plasmon coupling between gold nanoparticles. *Nano Lett.* **2005**, *5* (11), 2246-2252.

34. Sheikholeslami, S.; Jun, Y.-W.; Jain, P. K.; Alivisatos, A. P. Coupling of optical resonances in a compositionally asymmetric plasmonic nanoparticle dimer. *Nano Lett.* **2010**, *10* (7), 2655-2660.

35. Fromm, D. P.; Sundaramurthy, A.; Schuck, P. J.; Kino, G.; Moerner, W. E. Gap-dependent optical coupling of single "bowtie" nanoantennas resonant in the visible. *Nano Lett.* **2004**, *4* (5), 957-961.

36. Le, F.; Lwin, N. Z.; Steele, J. M.; Käll, M.; Halas, N. J.; Nordlander, P. Plasmons in the metallic nanoparticle− film system as a tunable impurity problem. *Nano Lett.* **2005**, *5* (10), 2009-2013.

37. Mock, J. J.; Hill, R. T.; Degiron, A.; Zauscher, S.; Chilkoti, A.; Smith, D. R. Distance-dependent plasmon resonant coupling between a gold nanoparticle and gold film. *Nano Lett.* **2008**, *8* (8), 2245-2252.

38. Ciracì, C.; Chen, X.; Mock, J. J.; McGuire, F.; Liu, X.; Oh, S.-H.; Smith, D. R. Film-coupled nanoparticles by atomic layer deposition: Comparison with organic spacing layers. *Appl. Phys. Lett.* **2014**, *104* (2), 023109.

39. Kongsuwan, N.; Demetriadou, A.; Horton, M.; Chikkaraddy, R.; Baumberg, J. J.; Hess, O. Plasmonic nanocavity modes: From near-field to far-field radiation. *ACS Photonics* **2020**, *7* (2), 463-471.

40. Cherqui, C.; Wu, Y.; Li, G.; Quillin, S. C.; Busche, J. A.; Thakkar, N.; West, C. A.; Montoni, N. P.; Rack, P. D.; Camden, J. P.; Masiello, D. J. STEM/EELS imaging of magnetic hybridization in symmetric

and symmetry-broken plasmon oligomer dimers and all-magnetic Fano interference. *Nano Lett.* **2016**, *16* (10), 6668-6676.

41. Kongsuwan, N.; Demetriadou, A.; Chikkaraddy, R.; Benz, F.; Turek, V. A.; Keyser, U. F.; Baumberg, J. J.; Hess, O. Suppressed quenching and strong-coupling of purcell-enhanced single-molecule emission in plasmonic nanocavities. *ACS Photonics* **2018**, *5* (1), 186-191.

42. Okamoto, T.; Yamaguchi, I. Optical absorption study of the surface plasmon resonance in gold nanoparticles immobilized onto a gold substrate by self-assembly technique. *J. Phys. Chem. B* **2003**, *107* (38), 10321-10324.

43. Huang, C.-Z.; Wu, M.-J.; Chen, S.-Y. High order gap modes of film-coupled nanospheres. *J. Phys. Chem. C* **2015**, *119* (24), 13799-13806.

44. Benz, F.; De Nijs, B.; Tserkezis, C.; Chikkaraddy, R.; Sigle, D. O.; Pukenas, L.; Evans, S. D.; Aizpurua, J.; Baumberg, J. J. Generalized circuit model for coupled plasmonic systems. *Opt. Express* **2015**, *23* (26), 33255-33269.

45. Duan, H.; Fernández-Domínguez, A. I.; Bosman, M.; Maier, S. A.; Yang, J. K. W. Nanoplasmonics: Classical down to the nanometer scale. *Nano Lett.* **2012**, *12* (3), 1683-1689.

46. Wang, B.-L.; Ren, M.-L.; Li, J.-F.; Li, Z.-Y. Plasmonic coupling effect between two gold nanospheres for efficient second-harmonic generation. *J. Appl. Phys.* **2012**, *112* (8), 083102.

47. Tian, X.; Zhou, Y.; Thota, S.; Zou, S.; Zhao, J. Plasmonic coupling in single silver nanosphere assemblies by polarization-dependent dark-field scattering spectroscopy. *J. Phys. Chem. C* **2014**, *118* (25), 13801-13808.

48. Sigle, D. O.; Mertens, J.; Herrmann, L. O.; Bowman, R. W.; Ithurria, S.; Dubertret, B.; Shi, Y.; Yang, H. Y.; Tserkezis, C.; Aizpurua, J.; Baumberg, J. J. Monitoring morphological changes in 2D monolayer semiconductors using atom-thick plasmonic nanocavities. *ACS Nano* **2015**, *9* (1), 825-830.

49. Chikkaraddy, R.; Turek, V. A.; Kongsuwan, N.; Benz, F.; Carnegie, C.; van de Goor, T.; De Nijs, B.; Demetriadou, A.; Hess, O.; Keyser, U. F.; Baumberg, J. J. Mapping nanoscale hotspots with single-molecule emitters assembled into plasmonic nanocavities using DNA origami. *Nano Lett.* **2018**, *18* (1), 405-411.

50. Langer, J.; Jimenez de Aberasturi, D.; Aizpurua, J.; Alvarez-Puebla, R. A.; Auguié, B.; Baumberg, J. J.; Bazan, G. C.; Bell, S. E. J.; Boisen, A.; Brolo, A. G. Present and future of surface-enhanced Raman scattering. *ACS Nano* **2019**, *14* (1), 28-117.

51. Li, J.-F.; Li, C.-Y.; Aroca, R. F. Plasmon-enhanced fluorescence spectroscopy. *Chem. Soc. Rev.* **2017**, *46* (13), 3962-3979.

52. Liu, S.-D.; Leong, E. S. P.; Li, G.-C.; Hou, Y.; Deng, J.; Teng, J. H.; Ong, H. C.; Lei, D. Y. Polarization-independent multiple Fano resonances in plasmonic nonamers for multimode-matching enhanced multiband second-harmonic generation. *ACS Nano* **2016**, *10* (1), 1442-1453.

53. Zhang, S.; Li, G.-C.; Chen, Y.; Zhu, X.; Liu, S.-D.; Lei, D. Y.; Duan, H. Pronounced Fano resonance in single gold split nanodisks with 15 nm split gaps for intensive second harmonic generation. *ACS Nano* **2016**, *10* (12), 11105-11114.

54. Törmä, P.; Barnes, W. L. Strong coupling between surface plasmon polaritons and emitters: a review. *Rep. Prog. Phys.* **2014**, *78* (1), 013901.

55. Ding, S.-J.; Li, X.; Nan, F.; Zhong, Y.-T.; Zhou, L.; Xiao, X.; Wang, Q.-Q.; Zhang, Z. Strongly asymmetric spectroscopy in plasmon-exciton hybrid systems due to interference-induced energy repartitioning. *Phys. Rev. Lett.* **2017**, *119* (17), 177401.

56. Zhu, W.; Crozier, K. B. Quantum mechanical limit to plasmonic enhancement as observed by surface-enhanced Raman scattering. *Nat. Commun.* **2014**, *5* (1), 1-8.

57. Ciracì, C.; Hill, R. T.; Mock, J. J.; Urzhumov, Y.; Fernández-Domínguez, A. I.; Maier, S. A.; Pendry,

J. B.; Chilkoti, A.; Smith, D. R. Probing the ultimate limits of plasmonic enhancement. *Science* **2012**, *337* (6098), 1072-1074.

58. Xu, D.; Xiong, X.; Wu, L.; Ren, X.-F.; Png, C. E.; Guo, G.-C.; Gong, Q.; Xiao, Y.-F. Quantum plasmonics: new opportunity in fundamental and applied photonics. *Adv. Opt. Photon.* **2018**, *10* (4), 703-756.

59. Zhu, W.; Esteban, R.; Borisov, A. G.; Baumberg, J. J.; Nordlander, P.; Lezec, H. J.; Aizpurua, J.; Crozier, K. B. Quantum mechanical effects in plasmonic structures with subnanometre gaps. *Nat. Commun.* **2016**, *7* (1), 1-14.

60. Scholl, J. A.; García-Etxarri, A.; Koh, A. L.; Dionne, J. A. Observation of quantum tunneling between two plasmonic nanoparticles. *Nano Lett.* **2013**, *13* (2), 564-569.

61. Zhou, Z.-K.; Liu, J.; Bao, Y.; Wu, L.; Png, C. E.; Wang, X.-H.; Qiu, C.-W. Quantum plasmonics get applied. *Prog. Quant. Electron.* **2019**, *65*, 1-20.

62. Baumberg, J. J.; Aizpurua, J.; Mikkelsen, M. H.; Smith, D. R. Extreme nanophotonics from ultrathin metallic gaps. *Nat. Mater.* **2019**, *18* (7), 668-678.

63. García de Abajo, F. J. Nonlocal effects in the plasmons of strongly interacting nanoparticles, dimers, and waveguides. *J. Phys. Chem. C* **2008**, *112* (46), 17983-17987.

64. Raza, S.; Bozhevolnyi, S. I.; Wubs, M.; Mortensen, N. A. Nonlocal optical response in metallic nanostructures. *J. Phys.: Condens. Matter* **2015**, *27* (18), 183204.

65. McMahon, J. M.; Gray, S. K.; Schatz, G. C. Optical properties of nanowire dimers with a spatially nonlocal dielectric function. *Nano Lett.* **2010**, *10* (9), 3473-3481.

66. Toscano, G.; Raza, S.; Jauho, A.-P.; Mortensen, N. A.; Wubs, M. Modified field enhancement and extinction by plasmonic nanowire dimers due to nonlocal response. *Opt. Express* **2012**, *20* (4), 4176-4188.

67. Ciracì, C.; Pendry, J. B.; Smith, D. R. Hydrodynamic model for plasmonics: a macroscopic approach to a microscopic problem. *ChemPhysChem* **2013**, *14* (6), 1109-1116.

68. Ford, G. W.; Weber, W. H. Electromagnetic interactions of molecules with metal surfaces. *Phys. Rep.* **1984**, *113* (4), 195-287.

69. Apell, P. A simple derivation of the surface contribution to the reflectivity of a metal, and its use in the Van der Waals interaction. *Phys. Scr.* **1981**, *24* (4), 795.

70. Fernández-Domínguez, A. I.; Wiener, A.; García-Vidal, F. J.; Maier, S. A.; Pendry, J. B. Transformation-optics description of nonlocal effects in plasmonic nanostructures. *Phys. Rev. Lett.* **2012**, *108* (10), 106802.

71. Ginzburg, P.; Zayats, A. V. Localized surface plasmon resonances in spatially dispersive nano-objects: phenomenological treatise. *ACS Nano* **2013**, *7* (5), 4334-4342.

72. David, C.; García de Abajo, F. J. Spatial nonlocality in the optical response of metal nanoparticles. *J. Phys. Chem. C* **2011**, *115* (40), 19470-19475.

73. Barton, G. Some surface effects in the hydrodynamic model of metals. *Rep. Prog. Phys.* **1979**, *42* (6), 963.

74. Boardman, A. D. Hydrodynamic theory of plasmon-polaritons on plane surfaces. *Electromagnetic surface modes* **1982**, 1-76.

75. Toscano, G. *Semiclassical theory of nonlocal plasmonic excitation in metallic nanostructures*; Citeseer, 2013.

76. Ruppin, R. Extinction properties of thin metallic nanowires. *Opt. Commun.* **2001**, *190* (1-6), 205-209.

77. Esteban, R.; Borisov, A. G.; Nordlander, P.; Aizpurua, J. Bridging quantum and classical plasmonics with a quantum-corrected model. *Nat. Commun.* **2012**, *3* (1), 1-9.

78. Savage, K. J.; Hawkeye, M. M.; Esteban, R.; Borisov, A. G.; Aizpurua, J.; Baumberg, J. J. Revealing the quantum regime in tunnelling plasmonics. *Nature* **2012**, *491* (7425), 574-577.

79. Scholl, J. A.; Garcia-Etxarri, A.; Aguirregabiria, G.; Esteban, R.; Narayan, T. C.; Koh, A. L.; Aizpurua, J.; Dionne, J. A. Evolution of plasmonic metamolecule modes in the quantum tunneling regime. *ACS Nano* **2016**, *10* (1), 1346-1354.

80. Kushmerick, J. G.; Lazorcik, J.; Patterson, C. H.; Shashidhar, R.; Seferos, D. S.; Bazan, G. C. Vibronic contributions to charge transport across molecular junctions. *Nano Lett.* **2004**, *4* (4), 639-642.

81. Kim, B. S.; Choi, S. H.; Zhu, X.-Y.; Frisbie, C. D. Molecular tunnel junctions based on π-conjugated oligoacene thiols and dithiols between Ag, Au, and Pt contacts: effect of surface linking group and metal work function. *J. Am. Chem. Soc.* **2011**, *133* (49), 19864-19877.

82. Tan, S. F.; Wu, L.; Yang, J. K. W.; Bai, P.; Bosman, M.; Nijhuis, C. A. Quantum plasmon resonances controlled by molecular tunnel junctions. *Science* **2014**, *343* (6178), 1496-1499.

83. Pérez-González, O.; Zabala, N.; Borisov, A. G.; Halas, N. J.; Nordlander, P.; Aizpurua, J. Optical spectroscopy of conductive junctions in plasmonic cavities. *Nano Lett.* **2010**, *10* (8), 3090-3095.

84. Cui, X.; Qin, F.; Lai, Y.; Wang, H.; Shao, L.; Chen, H.; Wang, J.; Lin, H.-q. Molecular tunnel junction-controlled high-order charge transfer plasmon and Fano resonances. *ACS Nano* **2018**, *12* (12), 12541-12550.

85. Lin, L.; Zhang, Q.; Li, X.; Qiu, M.; Jiang, X.; Jin, W.; Gu, H.; Lei, D. Y.; Ye, J. Electron transport across plasmonic molecular nanogaps interrogated with surface-enhanced Raman scattering. *ACS Nano* **2018**, *12* (7), 6492-6503.

86. Jin, R.; Jureller, J. E.; Kim, H. Y.; Scherer, N. F. Correlating second harmonic optical responses of single Ag nanoparticles with morphology. *J. Am. Chem. Soc.* **2005**, *127* (36), 12482-12483.

87. Guan, Z.; Polavarapu, L.; Xu, Q.-H. Enhanced two-photon emission in coupled metal nanoparticles

induced by conjugated polymers. *Langmuir* **2010**, *26* (23), 18020-18023.

88. Siddiquee, A. M.; Taylor, A. B.; Syed, S.; Lim, G.-H.; Lim, B.; Chon, J. W. M. Measurement of plasmon-mediated two-photon luminescence action cross sections of single gold bipyramids, dumbbells, and hemispherically capped cylindrical nanorods. *J. Phys. Chem. C* **2015**, *119* (51), 28536-28543.

89. Venkatakrishnarao, D.; Narayana, Y. S. L. V.; Mohaiddon, M. A.; Mamonov, E. A.; Mitetelo, N.; Kolmychek, I. A.; Maydykovskiy, A. I.; Novikov, V. B.; Murzina, T. V.; Chandrasekar, R. Two-photon luminescence and second-harmonic generation in organic nonlinear surface comprised of self-assembled frustum shaped organic microlasers. *Adv. Mater.* **2017**, *29* (15), 1605260.

90. Molinaro, C.; El Harfouch, Y.; Palleau, E.; Eloi, F.; Marguet, S.; Douillard, L.; Charra, F.; Fiorini-Debuisschert, C. Two-photon luminescence of single colloidal gold nanorods: revealing the origin of plasmon relaxation in small nanocrystals. *J. Phys. Chem. C* **2016**, *120* (40), 23136-23143.

91. Dai, J.; Zeng, J.-H.; Lan, S.; Wan, X.; Tie, S.-L. Competition between second harmonic generation and two-photon-induced luminescence in single, double and multiple ZnO nanorods. *Opt. Express* **2013**, *21* (8), 10025-10038.

92. Mohamed, M. B.; Volkov, V.; Link, S.; El-Sayed, M. A. The 'lightning' gold nanorods: fluorescence enhancement of over a million compared to the gold metal. *Chem. Phys. Lett.* **2000**, *317* (6), 517-523.

93. Imura, K.; Nagahara, T.; Okamoto, H. Near-field two-photon-induced photoluminescence from single gold nanorods and imaging of plasmon modes. *J. Phys. Chem. B* **2005**, *109* (27), 13214-13220.

94. Han, F.; Guan, Z.; Tan, T. S.; Xu, Q.-H. Size-dependent two-photon excitation photoluminescence enhancement in coupled noble-metal nanoparticles. *ACS Appl. Mater. Interfaces* **2012**, *4* (9), 4746-4751.

95. Ueno, K.; Juodkazis, S.; Mizeikis, V.; Sasaki, K.; Misawa, H. Clusters of closely spaced gold nanoparticles as a source of two-photon photoluminescence at visible wavelengths. *Adv. Mater.* **2008**, *20* (1), 26-30.

96. Jiang, C.; Guan, Z.; Lim, S. Y. R.; Polavarapu, L.; Xu, Q.-H. Two-photon ratiometric sensing of Hg^{2+} by using cysteine functionalized Ag nanoparticles. *Nanoscale* **2011**, *3* (8), 3316-3320.

97. Guan, Z.; Li, S.; Cheng, P. B. S.; Zhou, N.; Gao, N.; Xu, Q.-H. Band-selective coupling-induced enhancement of two-photon photoluminescence in gold nanocubes and its application as turn-on fluorescent probes for cysteine and glutathione. *ACS Appl. Mater. Interfaces* **2012**, *4* (10), 5711-5716.

98. Guan, Z.; Gao, N.; Jiang, X.-F.; Yuan, P.; Han, F.; Xu, Q.-H. Huge enhancement in two-photon photoluminescence of Au nanoparticle clusters revealed by single-particle spectroscopy. *J. Am. Chem. Soc.* **2013**, *135* (19), 7272-7277.

99. Jiang, X.-F.; Pan, Y.; Jiang, C.; Zhao, T.; Yuan, P.; Venkatesan, T.; Xu, Q.-H. Excitation nature of two-photon photoluminescence of gold nanorods and coupled gold nanoparticles studied by two-pulse emission modulation spectroscopy. *J. Phys. Chem. Lett.* **2013**, *4* (10), 1634-1638.

100. Chen, Y.; Guan, R.; Zhang, C.; Huang, J.; Ji, L.; Chao, H. Two-photon luminescent metal complexes for bioimaging and cancer phototherapy. *Coord. Chem. Rev.* **2016**, *310*, 16-40.

101. Cahalan, M. D.; Parker, I.; Wei, S. H.; Miller, M. J. Two-photon tissue imaging: seeing the immune system in a fresh light. *Nat. Rev. Immunol.* **2002**, *2* (11), 872-880.

102. McPeak, K. M.; Jayanti, S. V.; Kress, S. J. P.; Meyer, S.; Iotti, S.; Rossinelli, A.; Norris, D. J. Plasmonic films can easily be better: rules and recipes. *ACS Photonics* **2015**, *2* (3), 326-333.

103. Lin, L.; Liu, Z.; Li, X.; Gu, H.; Ye, J. Quantifying the reflective index of nanometer-thick thiolated molecular layers on nanoparticles. *Nanoscale* **2017**, *9* (6), 2213-2218.

104. Lin, L.; Gu, H.; Ye, J. Plasmonic multi-shell nanomatryoshka particles as highly tunable SERS tags with built-in reporters. *Chem. Commun.* **2015**, *51* (100), 17740-17743.

105. Lee, Y.-J.; Schade, N. B.; Sun, L.; Fan, J. A.; Bae, D. R.; Mariscal, M. M.; Lee, G.; Capasso, F.; Sacanna, S.; Manoharan, V. N.; Yi, G.-R. Ultrasmooth, highly spherical monocrystalline gold particles

for precision plasmonics. *ACS Nano* **2013**, *7* (12), 11064-11070.

106. Hao, E.; Schatz, G. C. Electromagnetic fields around silver nanoparticles and dimers. *J. Chem. Phys.* **2004**, *120* (1), 357-366.

107. Lombardi, A.; Demetriadou, A.; Weller, L.; Andrae, P.; Benz, F.; Chikkaraddy, R.; Aizpurua, J.; Baumberg, J. J. Anomalous spectral shift of near-and far-field plasmonic resonances in nanogaps. *ACS Photonics* **2016**, *3* (3), 471-477.

108. Mertens, J.; Demetriadou, A.; Bowman, R. W.; Benz, F.; Kleemann, M.-E.; Tserkezis, C.; Shi, Y.; Yang, H. Y.; Hess, O.; Aizpurua, J.; Baumberg, J. J. Tracking optical welding through groove modes in plasmonic nanocavities. *Nano Lett.* **2016**, *16* (9), 5605-5611.

109. Sundaramurthy, A.; Crozier, K. B.; Kino, G. S.; Fromm, D. P.; Schuck, P. J.; Moerner, W. E. Field enhancement and gap-dependent resonance in a system of two opposing tip-to-tip Au nanotriangles. *Phys. Rev. B* **2005**, *72* (16), 165409.

110. Zuloaga, J.; Prodan, E.; Nordlander, P. Quantum plasmonics: optical properties and tunability of metallic nanorods. *ACS Nano* **2010**, *4* (9), 5269-5276.

111. Monreal, R. C.; Antosiewicz, T. J.; Apell, S. P. Competition between surface screening and size quantization for surface plasmons in nanoparticles. *New J. Phys.* **2013**, *15* (8), 083044.

112. Fuchs, R.; Kliewer, K. L. Surface plasmon in a semi-infinite free-electron gas. *Phys. Rev. B* **1971**, *3* (7), 2270.

113. Feibelman, P. J. Microscopic calculation of electromagnetic fields in refraction at a jellium-vacuum interface. *Phys. Rev. B* **1975**, *12* (4), 1319.

114. Fuchs, R.; Claro, F. Multipolar response of small metallic spheres: Nonlocal theory. *Phys. Rev. B* **1987**, *35* (8), 3722.

115. Esteban, R.; Zugarramurdi, A.; Zhang, P.; Nordlander, P.; García-Vidal, F. J.; Borisov, A. G.;

Aizpurua, J. A classical treatment of optical tunneling in plasmonic gaps: extending the quantum corrected model to practical situations. *Faraday Discuss.* **2015**, *178*, 151-183.

116.Scholl, J. A.; Koh, A. L.; Dionne, J. A. Quantum plasmon resonances of individual metallic nanoparticles. *Nature* **2012**, *483* (7390), 421-427.

117.Hajisalem, G.; Nezami, M. S.; Gordon, R. Probing the quantum tunneling limit of plasmonic enhancement by third harmonic generation. *Nano Lett.* **2014**, *14* (11), 6651-6654.

118.Zhao, Y.; Liu, X.; Lei, D. Y.; Chai, Y. Effects of surface roughness of Ag thin films on surface-enhanced Raman spectroscopy of graphene: spatial nonlocality and physisorption strain. *Nanoscale* **2014**, *6* (3), 1311-1317.

119.Chen, W.; Zhang, S.; Kang, M.; Liu, W.; Ou, Z.; Li, Y.; Zhang, Y.; Guan, Z.; Xu, H. Probing the limits of plasmonic enhancement using a two-dimensional atomic crystal probe. *Light Sci. Appl.* **2018**, *7* (1), 1-11.

120. Lo, T. W.; Zhang, Q.; Qiu, M.; Guo, X.; Meng, Y.; Zhu, Y.; Xiao, J. J.; Jin, W.; Leung, C. W.; Lei, D. Thermal redistribution of exciton population in monolayer transition metal dichalcogenides probed with plasmon–exciton coupling spectroscopy. *ACS Photonics* **2019**, *6* (2), 411-421.

121. Sun, J.; Hu, H.; Zheng, D.; Zhang, D.; Deng, Q.; Zhang, S.; Xu, H. Light-emitting plexciton: exploiting plasmon–exciton interaction in the intermediate coupling regime. *ACS Nano* **2018**, *12* (10), 10393-10402.

122. Ho, K. H. W.; Shang, A.; Shi, F.; Lo, T. W.; Yeung, P. H.; Yu, Y. S.; Zhang, X.; Wong, K. y.; Lei, D. Y. Plasmonic Au/TiO2-dumbbell-on-film nanocavities for high-efficiency hot-carrier generation and extraction. *Adv. Funct. Mater.* **2018**, *28* (34), 1800383.

123. Saito, R.; Hofmann, M.; Dresselhaus, G.; Jorio, A.; Dresselhaus, M. S. Raman spectroscopy of graphene and carbon nanotubes. *Adv. Phys.* **2011**, *60* (3), 413-550.

124. de Abajo, F. J. G. Graphene nanophotonics. *Science* **2013**, *339* (6122), 917-918.

125. Vanin, M.; Mortensen, J. J.; Kelkkanen, A. K.; Garcia-Lastra, J. M.; Thygesen, K. S.; Jacobsen, K. W. Graphene on metals: A van der Waals density functional study. *Phys. Rev. B* **2010**, *81* (8), 081408.

126. Amft, M.; Lebègue, S.; Eriksson, O.; Skorodumova, N. V. Adsorption of Cu, Ag, and Au atoms on graphene including van der Waals interactions. *J. Phys.: Condens. Matter* **2011**, *23* (39), 395001.

127. Chen, W.; Zhang, S.; Deng, Q.; Xu, H. Probing of sub-picometer vertical differential resolutions using cavity plasmons. *Nat. Commun.* **2018**, *9* (1), 1-8.

128. Esteban, R.; Aguirregabiria, G.; Borisov, A. G.; Wang, Y. M.; Nordlander, P.; Bryant, G. W.; Aizpurua, J. The morphology of narrow gaps modifies the plasmonic response. *ACS Photonics* **2015**, *2* (2), 295-305.

129. Mertens, J.; Eiden, A. L.; Sigle, D. O.; Huang, F.; Lombardo, A.; Sun, Z.; Sundaram, R. S.; Colli, A.; Tserkezis, C.; Aizpurua, J.; Milana, S.; Ferrari, A. C.; Baumberg, J. J. Controlling subnanometer gaps in plasmonic dimers using graphene. *Nano Lett.* **2013**, *13* (11), 5033-5038.

130. Shao, L.; Wang, X.; Xu, H.; Wang, J.; Xu, J.-B.; Peng, L.-M.; Lin, H.-Q. Nanoantenna-sandwiched graphene with giant spectral tuning in the visible-to-near-infrared region. *Adv. Optical Mater.* **2014**, *2* (2), 162-170.

131. Luo, Y.; Zhao, R.; Pendry, J. B. van der Waals interactions at the nanoscale: The effects of nonlocality. *Proc. Natl. Acad. Sci. U.S.A.* **2014**, *111* (52), 18422-18427.

132. Luo, Y.; Fernandez-Dominguez, A. I.; Wiener, A.; Maier, S. A.; Pendry, J. B. Surface plasmons and nonlocality: a simple model. *Phys. Rev. Lett.* **2013**, *111* (9), 093901.

133. Teperik, T. V.; Nordlander, P.; Aizpurua, J.; Borisov, A. G. Robust subnanometric plasmon ruler by rescaling of the nonlocal optical response. *Phys. Rev. Lett.* **2013**, *110* (26), 263901.

134. Zhang, Q.; Cai, X.; Yu, X.; Carregal-Romero, S.; Parak, W. J.; Sachan, R.; Cai, Y.; Wang, N.;

Zhu, Y.; Lei, D. Y. Electron energy-loss spectroscopy of spatial nonlocality and quantum tunneling effects in the bright and dark plasmon modes of gold nanosphere dimers. *Adv. Quantum Technol.* **2018**, *1* (1), 1800016.

135. Chikkaraddy, R.; Zheng, X.; Benz, F.; Brooks, L. J.; De Nijs, B.; Carnegie, C.; Kleemann, M.-E.; Mertens, J.; Bowman, R. W.; Vandenbosch, G. A. E.; Moshchalkov, V. V.; Baumberg, J. J. How ultranarrow gap symmetries control plasmonic nanocavity modes: from cubes to spheres in the nanoparticle-on-mirror. *ACS Photonics* **2017**, *4* (3), 469-475.

136. Holland, W. R.; Hall, D. G. Frequency shifts of an electric-dipole resonance near a conducting surface. *Phys. Rev. Lett.* **1984**, *52* (12), 1041.

137. Lévêque, G.; Martin, O. J. F. Optical interactions in a plasmonic particle coupled to a metallic film. *Opt. Express* **2006**, *14* (21), 9971-9981.

138. Di Martino, G.; Turek, V. A.; Tserkezis, C.; Lombardi, A.; Kuhn, A.; Baumberg, J. J. Plasmonic response and SERS modulation in electrochemical applied potentials. *Faraday Discuss.* **2017**, *205*, 537-545.

139. Powell, A. W.; Coles, D. M.; Taylor, R. A.; Watt, A. A. R.; Assender, H. E.; Smith, J. M. Plasmonic gas sensing using nanocube patch antennas. *Adv. Optical Mater.* **2016**, *4* (4), 634-642.

140. Li, J. F.; Huang, Y. F.; Ding, Y.; Yang, Z. L.; Li, S. B.; Zhou, X. S.; Fan, F. R.; Zhang, W.; Zhou, Z. Y.; Wu, D. Y.; Ren, B.; Wang, Z. L.; Tian, Z. Q. Shell-isolated nanoparticle-enhanced Raman spectroscopy. *Nature* **2010**, *464* (7287), 392-395.

141. Li, L.; Hutter, T.; Finnemore, A. S.; Huang, F. M.; Baumberg, J. J.; Elliott, S. R.; Steiner, U.; Mahajan, S. Metal oxide nanoparticle mediated enhanced Raman scattering and its use in direct monitoring of interfacial chemical reactions. *Nano Lett.* **2012**, *12* (8), 4242-4246.

142. Mubeen, S.; Zhang, S.; Kim, N.; Lee, S.; Krämer, S.; Xu, H.; Moskovits, M. Plasmonic

properties of gold nanoparticles separated from a gold mirror by an ultrathin oxide. *Nano Lett.* **2012**, *12* (4), 2088-2094.

143. Hajisalem, G.; Ahmed, A.; Pang, Y.; Gordon, R. Plasmon hybridization for enhanced nonlinear optical response. *Opt. Express* **2012**, *20* (28), 29923-29930.

144. Chen, J.-D.; Xiang, J.; Jiang, S.; Dai, Q.-F.; Tie, S.-L.; Lan, S. Radiation of the high-order plasmonic modes of large gold nanospheres excited by surface plasmon polaritons. *Nanoscale* **2018**, *10* (19), 9153-9163.

145. Li, G.-C.; Zhang, Q.; Maier, S. A.; Lei, D. Plasmonic particle-on-film nanocavities: a versatile platform for plasmon-enhanced spectroscopy and photochemistry. *Nanophotonics* **2018**, *7* (12), 1865-1889.

146. Liu, D.; Wu, T.; Zhang, Q.; Wang, X.; Guo, X.; Su, Y.; Zhu, Y.; Shao, M.; Chen, H.; Luo, Y.; Lei, D. Probing the in-plane near-field enhancement limit in a plasmonic particle-on-film nanocavity with surface-enhanced Raman spectroscopy of graphene. *ACS Nano* **2019**, *13* (7), 7644-7654.

147. Meng, Y.; Zhang, Q.; Lei, D.; Li, Y.; Li, S.; Liu, Z.; Xie, W.; Leung, C. W. Plasmon-induced optical magnetism in an ultrathin metal nanosphere-based dimer-on-film nanocavity. *Laser Photonics Rev.* **2020**, *14* (9), 2000068.

148. Benz, F.; Tserkezis, C.; Herrmann, L. O.; De Nijs, B.; Sanders, A.; Sigle, D. O.; Pukenas, L.; Evans, S. D.; Aizpurua, J.; Baumberg, J. J. Nanooptics of molecular-shunted plasmonic nanojunctions. *Nano Lett.* **2015**, *15* (1), 669-674.

149. Kawasaki, N.; Meuret, S.; Weil, R.; Lourenço-Martins, H.; Stéphan, O.; Kociak, M. Extinction and scattering properties of high-order surface plasmon modes in silver nanoparticles probed by combined spatially resolved electron energy loss spectroscopy and cathodoluminescence. *ACS Photonics* **2016**, *3* (9), 1654-1661.

150. Benz, F.; Schmidt, M. K.; Dreismann, A.; Chikkaraddy, R.; Zhang, Y.; Demetriadou, A.; Carnegie, C.; Ohadi, H.; De Nijs, B.; Esteban, R.; Aizpurua, J.; Baumberg, J. J. Single-molecule optomechanics in "picocavities". *Science* **2016**, *354* (6313), 726-729.

151. MacDonald, K. F.; Sámson, Z. L.; Stockman, M. I.; Zheludev, N. I. Ultrafast active plasmonics. *Nat. Photonics.* **2009**, *3* (1), 55-58.

152. Utikal, T.; Stockman, M. I.; Heberle, A. P.; Lippitz, M.; Giessen, H. All-optical control of the ultrafast dynamics of a hybrid plasmonic system. *Phys. Rev. Lett.* **2010**, *104* (11), 113903.

153. Wurtz, G. A.; Pollard, R.; Hendren, W.; Wiederrecht, G. P.; Gosztola, D. J.; Podolskiy, V. A.; Zayats, A. V. Designed ultrafast optical nonlinearity in a plasmonic nanorod metamaterial enhanced by nonlocality. *Nat. Nanotechnol.* **2011**, *6* (2), 107-111.

154. Wilson, W. M.; Stewart, J. W.; Mikkelsen, M. H. Surpassing single line width active tuning with photochromic molecules coupled to plasmonic nanoantennas. *Nano Lett.* **2018**, *18* (2), 853-858.

155. Chikkaraddy, R.; De Nijs, B.; Benz, F.; Barrow, S. J.; Scherman, O. A.; Rosta, E.; Demetriadou, A.; Fox, P.; Hess, O.; Baumberg, J. J. Single-molecule strong coupling at room temperature in plasmonic nanocavities. *Nature* **2016**, *535* (7610), 127-130.

156. Irie, M.; Uchida, K. Synthesis and properties of photochromic diarylethenes with heterocyclic aryl groups. *Bull. Chem. Soc. Jpn.* **1998**, *71* (5), 985-996.

157. Michota, A.; Bukowska, J. Surface-enhanced Raman scattering (SERS) of 4-mercaptobenzoic acid on silver and gold substrates. *J. Raman Spectrosc.* **2003**, *34* (1), 21-25.

158. Hanazawa, M.; Sumiya, R.; Horikawa, Y.; Irie, M. Thermally irreversible photochromic systems. Reversible photocyclization of 1,2-Bis(2-methylbenzo[*b*]thiophen-3-yl)perfluorocyclocoalkene derivatives. *J. Chem. Soc., Chem. Commun.* **1992**, (3), 206-207.

159. Matsuda, K.; Yamaguchi, H.; Sakano, T.; Ikeda, M.; Tanifuji, N.; Irie, M. Conductance

photoswitching of diarylethene−gold nanoparticle network induced by photochromic reaction. *J. Phys. Chem. C* **2008**, *112* (43), 17005-17010.

160. Takeshita, M.; Kato, N.; Kawauchi, S.; Imase, T.; Watanabe, J.; Irie, M. Photochromism of dithienylethenes included in cyclodextrins. *J. Org. Chem.* **1998**, *63* (25), 9306-9313.

161. Irie, M. *Photo-reactive materials for ultrahigh density optical memory: MITI research and development program on basic technologies for future industries*; Elsevier Science Inc., 1994.

162. Knebl, D.; Hörl, A.; Trügler, A.; Kern, J.; Krenn, J. R.; Puschnig, P.; Hohenester, U. Gap plasmonics of silver nanocube dimers. *Phys. Rev. B* **2016**, *93* (8), 081405.

163. Bardhan, R.; Mukherjee, S.; Mirin, N. A.; Levit, S. D.; Nordlander, P.; Halas, N. J. Nanosphere-in-a-nanoshell: a simple nanomatryushka. *J. Phys. Chem. C* **2010**, *114* (16), 7378-7383.

164. Song, J.; Duan, B.; Wang, C.; Zhou, J.; Pu, L.; Fang, Z.; Wang, P.; Lim, T. T.; Duan, H. SERS-encoded nanogapped plasmonic nanoparticles: growth of metallic nanoshell by templating redox-active polymer brushes. *J. Am. Chem. Soc.* **2014**, *136* (19), 6838-6841.

165. Shen, W.; Lin, X.; Jiang, C.; Li, C.; Lin, H.; Huang, J.; Wang, S.; Liu, G.; Yan, X.; Zhong, Q.; Ren, B. Reliable quantitative SERS analysis facilitated by core–shell nanoparticles with embedded internal standards. *Angew. Chem. Int. Ed.* **2015**, *54* (25), 7308-7312.

166. Khlebtsov, N. G.; Lin, L.; Khlebtsov, B. N.; Ye, J. Gap-enhanced Raman tags: fabrication, optical properties, and theranostic applications. *Theranostics* **2020**, *10* (5), 2067-2094.

167. Lin, L.; Zapata, M.; Xiong, M.; Liu, Z.; Wang, S.; Xu, H.; Borisov, A. G.; Gu, H.; Nordlander, P.; Aizpurua, J.; Ye, J. Nanooptics of plasmonic nanomatryoshkas: shrinking the size of a core–shell junction to subnanometer. *Nano Lett.* **2015**, *15* (10), 6419-6428.

168. Khalid, M.; Ciracì, C. Numerical analysis of nonlocal optical response of metallic nanoshells. *Photonics* **2019**, *6* (2), 39.

169. Zakomirnyi, V. I.; Rasskazov, I. L.; Sørensen, L. K.; Carney, P. S.; Rinkevicius, Z.; Ågren, H. Plasmonic nano-shells: atomistic discrete interaction *versus* classic electrodynamics models. *Phys. Chem. Chem. Phys.* **2020**, *22* (24), 13467-13473.

170. Zapata, M.; Beltrán, Á. S. C.; Borisov, A. G.; Aizpurua, J. Quantum effects in the optical response of extended plasmonic gaps: validation of the quantum corrected model in core-shell nanomatryushkas. *Opt. Express* **2015**, *23* (6), 8134-8149.

171. Khalid, M.; Della Sala, F.; Ciracì, C. Optical properties of plasmonic core-shell nanomatryoshkas: a quantum hydrodynamic analysis. *Opt. Express* **2018**, *26* (13), 17322-17334.

172. Kulkarni, V.; Prodan, E.; Nordlander, P. Quantum plasmonics: optical properties of a nanomatryushka. *Nano Lett.* **2013**, *13* (12), 5873-5879.

173. Bohren, C. F.; Huffman, D. R. *Absorption and scattering of light by small particles*; John Wiley & Sons, 2008.

174. Khlebtsov, B. N.; Khlebtsov, N. G. Surface morphology of a gold core controls the formation of hollow or bridged nanogaps in plasmonic nanomatryoshkas and their SERS responses. *J. Phys. Chem. C* **2016**, *120* (28), 15385-15394.

175. Li, G.-C.; Zhang, Y.-L.; Jiang, J.; Luo, Y.; Lei, D. Y. Metal-substrate-mediated plasmon hybridization in a nanoparticle dimer for photoluminescence line-width shrinking and intensity enhancement. *ACS Nano* **2017**, *11* (3), 3067-3080.

176. Wang, D.-S.; Hsu, F.-Y.; Lin, C.-W. Surface plasmon effects on two photon luminescence of gold nanorods. *Opt. Express* **2009**, *17* (14), 11350-11359.

177. Chen, L.; Li, G.-C.; Liu, G.-Y.; Dai, Q.-F.; Lan, S.; Tie, S.-L.; Deng, H.-D. Sensing the moving direction, position, size, and material type of nanoparticles with the two-photon-induced luminescence of a single gold nanorod. *J. Phys. Chem. C* **2013**, *117* (39), 20146-20153.

178. Huang, Z.; Dai, Q.; Lan, S.; Tie, S. Numerical study of nanoparticle sensors based on the detection of the two-photon-induced luminescence of gold nanorod antennas. *Plasmonics* **2014**, *9* (6), 1491-1500.

179. Boyd, G. T.; Yu, Z. H.; Shen, Y. R. Photoinduced luminescence from the noble metals and its enhancement on roughened surfaces. *Phys. Rev. B* **1986**, *33* (12), 7923.

180. Koya, A. N.; Lin, J. Charge transfer plasmons: Recent theoretical and experimental developments. *Appl. Phys. Rev.* **2017**, *4* (2), 021104.

181. Wang, T.; Nijhuis, C. A. Molecular electronic plasmonics. *Appl. Mater. Today* **2016**, *3*, 73-86.

182. Gerislioglu, B.; Ahmadivand, A. Functional charge transfer plasmon metadevices. *Research* **2020**, *2020*, 9468692.

183. Jia, C.; Guo, X. Molecule–electrode interfaces in molecular electronic devices. *Chem. Soc. Rev.* **2013**, *42* (13), 5642-5660.

184. Xiang, D.; Wang, X.; Jia, C.; Lee, T.; Guo, X. Molecular-scale electronics: from concept to function. *Chem. Rev.* **2016**, *116* (7), 4318-4440.

185. McCreery, R. L.; Bergren, A. J. Progress with molecular electronic junctions: meeting experimental challenges in design and fabrication. *Adv. Mater.* **2009**, *21* (43), 4303-4322.

186. Lu, Q.; Liu, K.; Zhang, H.; Du, Z.; Wang, X.; Wang, F. From tunneling to hopping: a comprehensive investigation of charge transport mechanism in molecular junctions based on oligo(*p*-phenylene ethynylene)s. *ACS Nano* **2009**, *3* (12), 3861-3868.

187. Choi, S. H.; Kim, B. S.; Frisbie, C. D. Electrical resistance of long conjugated molecular wires. *Science* **2008**, *320* (5882), 1482-1486.

188. Vadai, M.; Nachman, N.; Ben-Zion, M.; Bürkle, M.; Pauly, F.; Cuevas, J. C.; Selzer, Y. Plasmon-induced conductance enhancement in single-molecule junctions. *J. Phys. Chem. Lett.* **2013**, *4* (17), 2811-

2816.

189. García de Abajo, F. J. Graphene plasmonics: challenges and opportunities. *ACS Photonics* **2014**, *1* (3), 135-152.

190. Thongrattanasiri, S.; Koppens, F. H. L.; García de Abajo, F. J. Complete optical absorption in periodically patterned graphene. *Phys. Rev. Lett.* **2012**, *108* (4), 047401.

191. Hanson, G. W. Dyadic Green's functions and guided surface waves for a surface conductivity model of graphene. *J. Appl. Phys.* **2008**, *103* (6), 064302.

192. Mousavi, S. H.; Kholmanov, I.; Alici, K. B.; Purtseladze, D.; Arju, N.; Tatar, K.; Fozdar, D. Y.; Suk, J. W.; Hao, Y.; Khanikaev, A. B.; Ruoff, R. S.; Shvets, G. Inductive tuning of Fano-resonant metasurfaces using plasmonic response of graphene in the mid-infrared. *Nano Lett.* **2013**, *13* (3), 1111-1117.